Adaptive Optic Demonstrators for Extremely Large Telescopes

Michael Aloysius Campbell

Institute for Astronomy

School of Physics and Astronomy

University of Edinburgh

Doctor of Philosophy

2010

Abstract

The next generation of ground-based optical/infrared (IR) telescopes will have primary mirrors of up to 42 m. To take advantage of the large potential increase in angular resolution, adaptive optics will be essential to overcome the resolution limits set by atmospheric turbulence. Novel techniques such as Multi-Conjugate Adaptive Optics (MCAO) and Multi-Object Adaptive Optics (MOAO) are being developed to achieve near diffraction-limited images over large fields-of-view. This thesis concerns the development of MCAO and MOAO pathfinders. Specifically, the construction of CANARY, a MOAO demonstrator, and the on-sky performance and scientific exploitation of the Multi-conjugate Adaptive optics Demonstrator (MAD).

CANARY is under construction for the William Herschel Telescope (WHT) in La Palma and contains a telescope simulator to allow testing of the set-up in the laboratory. The simulator contains a natural guide star emulator, turbulence phase screens, and telescope relay optics. The work presented here concerns the integration of the various components in relation to numerical models and the CANARY specifications.

MAD was a near-IR imager on the Very Large Telescope (VLT) in Chile. Science demonstration observations were taken of R136, the young, massive cluster situated in the 30 Doradus star-forming region in the Large Magellanic Cloud. These data were used here to determine the MCAO performance across the $\sim$1'$\times$1' field-of-view, for different pointings with respect to the guide stars, finding high Strehl ratios and relatively uniform corrections across the fields.

The MAD data are then used to construct radial surface brightness profiles for R136, providing new insights into intriguing past results from the *Hubble Space Telescope*. The MAD data reveal that the profile is strongly asymmetric, removing the need for dramatic dynamical evolution of the cluster in the recent past, and highlighting the importance of considering asymmetries when analysing clusters further afield. The MAD data, combined with other near-IR imaging from the VLT, are then used to investigate the nature of candidate young stellar objects from recent observations with the *Spitzer Space Telescope*.

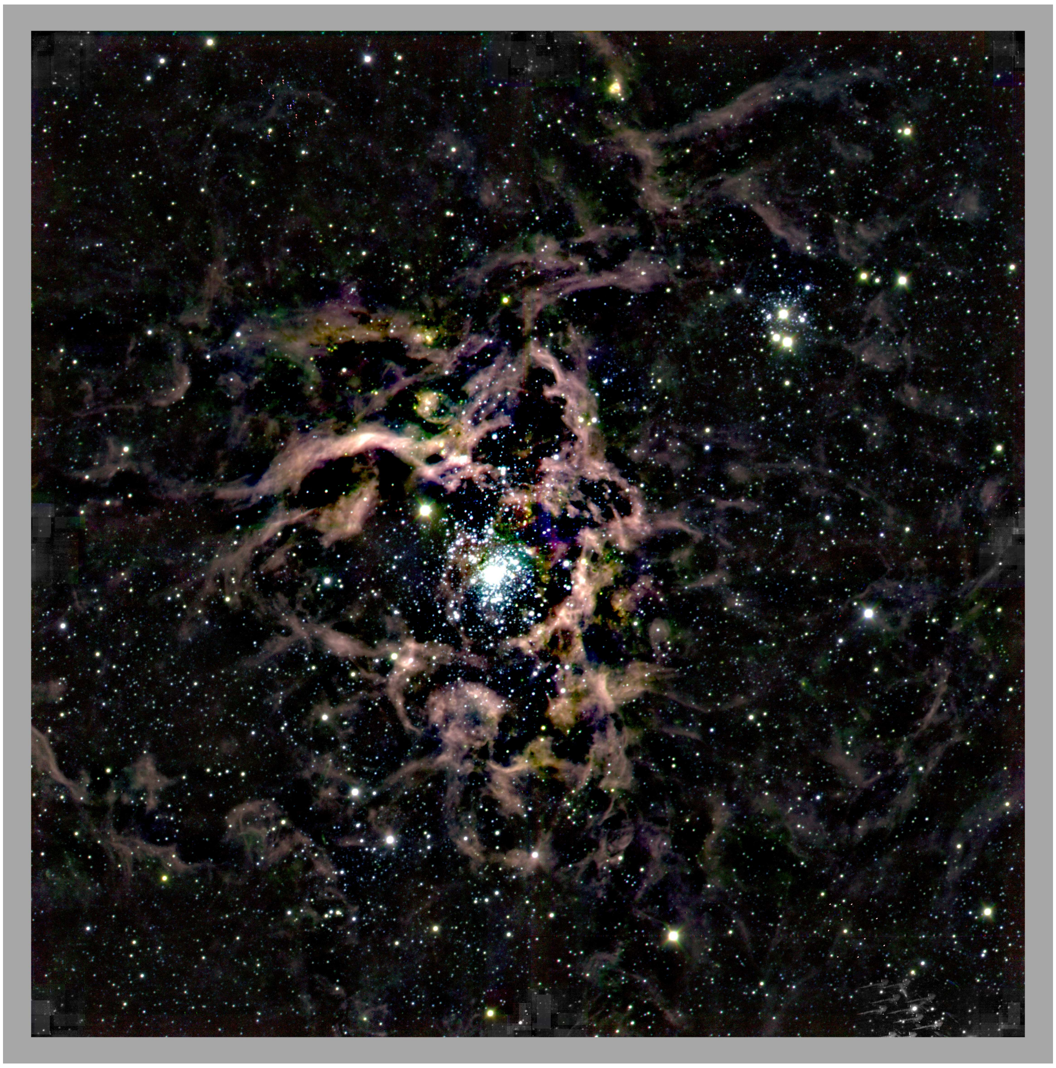

Declaration

I declare that this thesis is not substantially the same as any that I have submitted for a degree or diploma or other qualification at any other University. I further state that no part of my thesis has already been or is being concurrently submitted for any such degree, diploma or other qualification.

This thesis is the outcome of my own work except where specifically indicated in the text.

Michael Aloysius Campbell
Edinburgh
31st August 2010

Acknowledgements

I would like to thank my supervisor Chris Evans who has helped make my time in Edinburgh highly enjoyable. I have learnt a lot from Chris and he has provided endless support and encouragement throughout my four years, for which I am extremely grateful. This also extends to Andy Longmore, who has been acting as an unoffical supervisor for the past two years.

I would also like to thank members of the CANARY team, particularly Stephen Todd, David Henry, Tim Morris and Richard Wilson, who have always been willing to answer questions.

I spent an extremely enjoyable eight months in Tenerife and must thank Paco Garzon who provided supervison during that time. That was funded through a Marie Curie fellowship. Marie Curie is an amazing charity, carrying out fantastic work over a range of areas.

My fellow students also deserve a mention, particularly Neil Philips with whom I shared an office. His ability to put up with my inane chat, silly questions and choice of music has been quite outstanding.

I would like to thank Mike Briggs, who I have known from my undergraduate days at Leicester. It was Mike that convinced me to come to Edinburgh and complete a Ph.D. Now that it is complete, I am extremely grateful for that.

I have to mention STFC who have fallen on hard times in recent years. Suffering from financial hardship, they almost went bust until Mr Fitton came to the rescue. Swindon Town have proved many interesting days out since I have been in Edinburgh, although few have resulted in wins. This includes a trip to Wembley, at which the sub-standard pitch resulted in a unfortunate bobble, keeping us in league one. Hopefully better days are ahead.

I should also mention the other STFC, who provided funding during my time in Edinburgh. I have done some fantastic things over the last four years, a lot of which would not have been possible without STFC and Marie Curie

I would like to acknowledge my brother and sisters, who will now have too put up with me being (even more) big headed, and most likely unbearable at times. Finally, and most importantly, I would like to thank my parents, who have provided me every opportunity to reach this stage. I would like to thank them for their constant encouragement and support.

MAC
Edinburgh
31st August 2010

Table of Contents

List of Figures

List of Tables

Chapter 1

Introduction

The next generation of optical/infrared telescopes, collectively known as Extremely Large Telescopes (ELTs), will see primary apertures greater than 20m. This is a huge increase over the current 8-10m facilities and will revolutionise ground-based capabilities, increasing photon collecting power and theoretical angular resolution. Adaptive Optics (AO) is required to overcome the limits imposed by the atmosphere and achieve the potential gains available to large telescopes. AO has made impressive developments over the past 25 years as the systems become more complicated but provide better performance. This thesis concerns novel AO systems required to make corrections over large Fields of View (FoV). Over the course of my Ph.D I have worked with two novel wide-field instruments, in the laboratory during the construction phase, and on-sky for science verification. This has led to instrument characterisations and published science results from the verification observations and other complementary data.

As part of the instrumentation side of my work, I have been involved with CANARY, a Multi-Object Adaptive Optics (MOAO) demonstrator. I have mainly been involved in a telescope simulator, in which artificial stars are created and disturbed by a turbulence simulator. I have created numerical simulations of the expected performance of the turbulence simulator and made comparisons with empirical laboratory tests. An introduction to atmospheric turbulence and its influence on astronomical observations is provided later in this chapter . This is followed by the fundamental principles of wide-field AO systems, explaining the effect the atmosphere has in choosing which AO instrument is best suited for a given job.

My main area of astronomical research has revolved around the Young Massive Cluster (YMC) R136, found in the Large Magellanic Cloud (LMC). After analysing the performance of a novel Multi-Conjugate Adaptive Optics (MCAO) demonstrator, the observations were used to investigate the radial surface brightness profile of R136. These were used to study the cluster formation and its likely evolution, so the last part of this chapter contains an introduction to R136 and the broader 30 Doradus region which it resides in.

1.1 Extremely Large Telescopes

Three ELTs have currently been proposed, two by North American consortia with international partners, and one by the European Southern Observatory (ESO). ESO plans to build the European-ELT (E-ELT), with a 42m primary mirror, on Cerro Armazones in the Atacama desert in Chile (see Figure 1.1).

1.1.1 Science Drivers

The increased sensitivity and high angular resolution that comes with an ELT has been motivated by a host of science cases. These are usually split into three areas, including topics such as:

- Planets and Stars
    - Detection of exoplanets in habitable zones,
    - Understanding the physics and evolution of protoplanetary disks,
    - Studying the formation of the most massive stars,
    - Probing the formation and evolution of brown dwarfs.

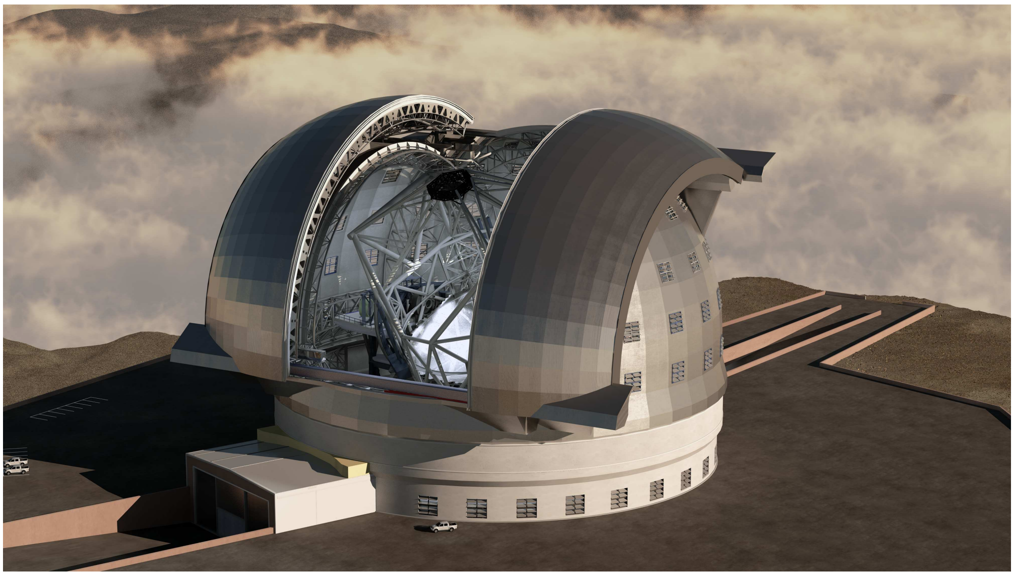

Figure 1.1: Artists impression of the European Extremely Large Telescope, courtesy of ESO.

- Stars and Galaxies
    - The formation and evolution of stellar clusters,
    - Determining whether the Initial Mass Function (IMF) varies with different environments or if it is universal as current observations suggest,
    - Mapping the current motions and metallicities of stellar populations to gain insight into galaxy assembly and evolution,
    - Understanding the influence of Active Galactic Nuclei on their surrounding environment.
- Galaxies and Cosmology
    - Study the evolution of galaxies in the Local Group out to unprecedented redshifts,
    - Characterisation of the first galaxies after “first light”,
    - Gain an understanding of cosmic expansion.

With ELT technology, virtually no area of astronomy will go untouched. Such an ambitious project comes with considerable challenges, from engineering, project management, and science management, to economic and political issues. One thing is clear, that in order to gain the most from an ELT, it must be able to perform to its potential and as efficiently as possible.

1.2 Adaptive Optics

Without the Earth's atmosphere life could not exist and conditions would be very different. However, from an astronomical point of view it hinders our ability to observe the Universe. In the optical and Near-InfraRed (N-IR) regime the atmosphere creates aberrations in the optical path, distorting images at the telescope detector. The purpose of AO is to correct for the aberrations.

1.2.1 Atmospheric Parameters

The atmosphere presents three main difficulties for astronomical observations. Firstly, the atmosphere is not transparent at all wavelengths and so observing the Universe in some wavelength regimes, such as the Far-Infrared (F-IR), is only possible from space. Optical wavelengths have a consistently high transmission but, between 1-10 µm, certain bands become opaque due to absorption from H_2O and CO_2 molecules through molecular vibrations.

Chemical reactions high in the Earth's atmosphere stop the night sky from ever becoming completely dark. The effect is referred to as airglow and occurs from the re-combination of ions created by cosmic rays, or chemiluminescence, mainly from oxygen and nitrogen atoms reacting with hydroxyl ions in the outer reaches of the atmosphere. The effect is particularly noticeable in the N-IR.

The most disruptive influence on observations is caused by atmospheric turbulence. Differential temperatures in the atmosphere ($< 1°C$) result in random changes in wind velocities (eddies), which we observe as turbulence. The temperature variations result

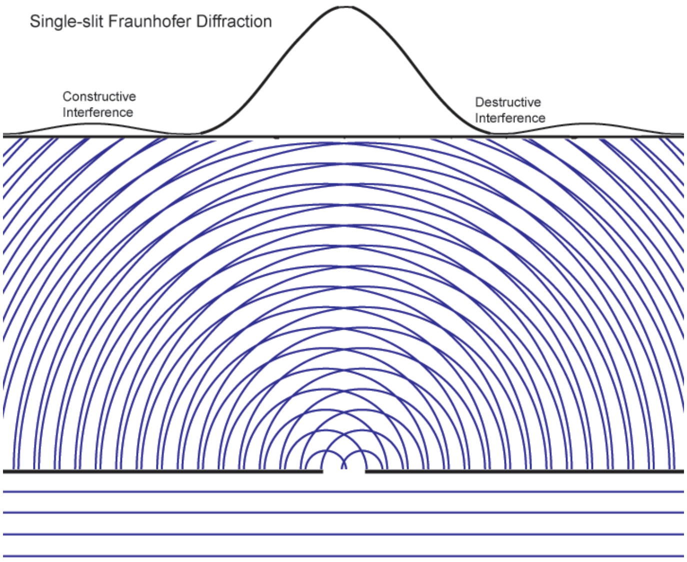

Figure 1.2: Single slit causing interference pattern through Fraunhofer diffraction. Courtesy of www.informationphilosopher.com.

in small changes in atmospheric density within different airmass[1]. The refractive index of the airmass is proportional to its density and so each airmass acts like a small lens, refracting the light as it propagates through.

1.2.2 Diffraction limit

The maximum resolution achievable by an optical system is set by the diffraction limit caused by Fraunhofer diffraction as light travels through an aperture. Applying Huygen's principle to a flat wave at an aperture, (i.e, all points along the aperture can be considered a point source radiating symmetrically outwards), rays travel at different angles towards the image plane, and hence also travel different distances. The difference in path length results in the coherent light interfering constructively or destructively (see Figure 1.2).

Where the path difference is equal to one wavelength, λ, the interference will be constructive. In Figure 1.3, constructive interference occurs when the top and bot-

---

[1] Airmass in this context refers to a mass of air, not the astronomical (1-zenith) distance.

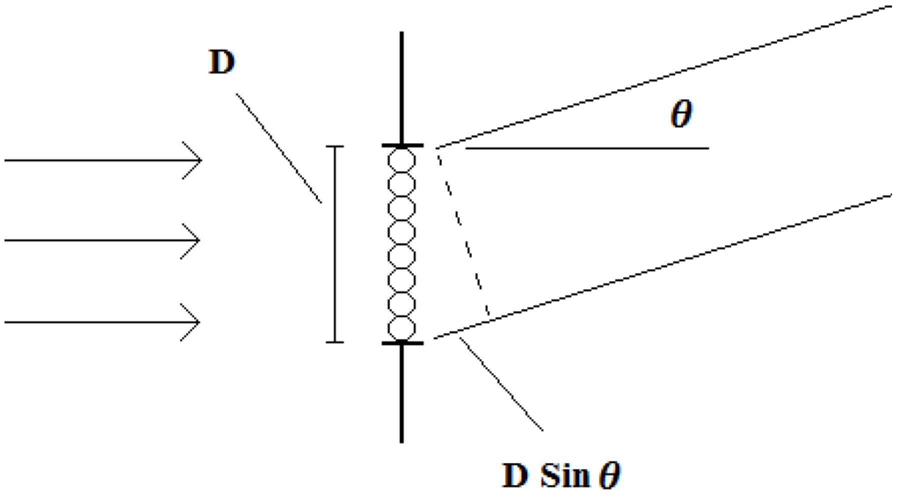

Figure 1.3: Single slit applying Huygen's principle across the field. θ is the angular tilt, λ is the wavelength and *D* is the telescope aperture.

tom rays have a path difference $D\sin\theta=\lambda$. At this same angle, θ, the top source and source in the middle of the aperture will undergo destructive interference, as well as other sources separated by $D/2$. Following this argument across the slit, at a radius of $D\sin\theta=\lambda$ from the central maximum, the first minima can be found.

Two objects are spatially resolved when the maximum of one diffraction pattern occurs in the minima of the other. Therefore, the diffraction limited angular resolution of a telescope is the angular distance to the first minima, which is dependent on the aperture size, *D*, and the wavelength, λ. The diffraction pattern from a circular aperture is an airy pattern, resulting in Equation 1.1, referred to as the Raleigh resolution:

$$R = 1.22\left(\frac{\lambda}{d}\right), \tag{1.1}$$

This relationship breaks down when optical aberrations are introduced. A plane wave entering the atmosphere will undergo differential refraction due to atmospheric turbulence and imperfections in the telescope optics. This results in a variation in phase across the wave by the time it reaches the detector. Peaks and troughs in intensity are created by interference, such that a scatter pattern forms at the image plane, where a diffraction pattern would have formed had no atmosphere been present. The density of the atmosphere decreases exponentially with altitude so turbulent effects decrease similarly with altitude. Turbulence caused by temperature variations are only significant to an altitude of ~10km (Hardy, 1998). Above this, the dominant cause of turbulence is shear winds (particularly at the tropopause (a typical height for the tropopause is 15km±1km (Garcia-Lorenzo et al., 2004)), the boundary between the troposphere and stratosphere, where air no longer cools with altitude.)

Kolmogorov (1941) developed a model of turbulence looking at the mechanical structure of the atmosphere. He assumed that energy is added to the system through large-scale disturbances, which dissipate to smaller and smaller scales. Energy is added to the system through solar heating during the day, creating convection cells near the surface. At night, the main source of energy comes from mixing of airmass at different temperatures and altitudes through winds. Kolmogorov introduced structure functions to describe the random fluctuations in refractive index within the atmosphere. The mean value of meteorological terms, such as temperature and pressure change slowly over time. A structure function calculates the average difference between two values of a random process, while adjusting for the slow changes in the mean values with time, allowing distinction between fluctuations from the mean value and those due to slowly varying mean values.

Tatarskii (1971) assumed that the variations in refractive index result directly in phase fluctuations described by $\phi(\mathbf{r})$, whereas any change in amplitude is due to second order effects acting on the already perturbed wavefront. This means that imaging performance is dominated by phase fluctuations and that amplitude fluctuations have a negligible effect on the structure of images seen in the focus of a large telescope. Tatarskii defined the structure function ($D_{\phi_a(r)}$) in terms of phase (ϕ_a):

$$D_{\phi_a(r)} = \langle [\phi_a(\mathbf{r}_1 + \mathbf{r}) - \phi_a(\mathbf{r}_1)]^2 \rangle, \tag{1.2}$$

where the phase is represented by

$$\phi_a(\mathbf{r}) = \frac{2\pi}{\lambda} l(\mathbf{x}), \tag{1.3}$$

in which $l(\mathbf{x})$ represents the optical path. Thus, the wavelength dependence of the structure function is:

$$D_{\phi_a(r)} \propto \lambda^{-2}. \tag{1.4}$$

By assuming the random phase variations were Gaussian, Tatarskii determined the structure function, integrated over the line of sight.

$$D_{\phi_a(r)} = 6.88 \left(\left| \frac{\mathbf{r}}{r_o} \right| \right)^{\frac{5}{3}}, \tag{1.5}$$

where r_0 is the Fried parameter. The Fried parameter is used to describe the strength of atmospheric turbulence, with its value determining the quality of the image observed. It effectively gives the length over which a wave will stay coherent. Apertures larger than r_0 will no longer be diffraction limited. Noll (1976) found that the mean square wavefront phase distortion over a circular area of diameter, d, is given by:

$$\sigma^2 = 1.03 \left(\frac{d}{r_0} \right)^{\frac{5}{3}}. \tag{1.6}$$

The root mean square of phase distortions for a circular aperture of radius r_0 is 1rad. For apertures larger than r_0, turbulent effects become significant and image quality deteriorates. Small values of r_0 indicate strong turbulence and bad seeing, whereas large values mean weak turbulence and so good seeing conditions. In the IR, r_0 can reach a few meres in good conditions, reducing down to centimetres in the optical during bad conditions (Tyson, 1998). From Equations (1.4) & (1.5) it can be seen that $r_0 \propto \lambda^{\frac{6}{5}}$. Therefore, the longer the wavelength, the better the seeing conditions.

If the aperture of a telescope is smaller than r_0, the telescope resolution is still determined by the diameter of the aperture, however, the atmosphere adds a tilt term which alters the image position. When $d > r_0$, phase variations within regions of the wavefront increase and multiple diffraction-limited images scatter over the detector. During long exposures, the scattered images smooth and the resolution becomes dependent on the Fried parameter (λ/r_0). At the best astronomical sites, the median seeing disk at 500nm is $\sim 0\overset{\prime\prime}{.}5$. The resolution limit for an 8m telescope at 500nm is $\sim 0\overset{\prime\prime}{.}015$ and so atmospheric turbulence reduces the resolution by two orders of magnitude. As we move towards ELTs, theoretical resolutions of $0\overset{\prime\prime}{.}003$ are possible, strongly highlighting the necessity of AO corrections.

Seeing Value

An image can be described by its spatial frequency components, from large-scale structure, to extremely fine detail. In essence, an imaging system transfers as much of this information as possible, with its ability to do so quantified by an Optical Transfer Function (OTF). The OTF describes the complex amplitude of the received wavefront in terms of spatial frequency in the optical aperture. From the OTF, the system's spatial frequency response is ascertained. If the system were perfect (OTF=1), all information and fine detail would be passed on. For all high spatial frequency data to be transfered, an infinitely large telescope would be required and so, in practice, the OTF is always less than one.

The Fourier transform of the OTF gives the time-averaged intensity distribution at the focal plane. If the OTF of the system is known, the corresponding structure in the focal plane can be found. For a time averaged system, a Point Spread Function (PSF) will result. The OTF of the system is the combination of the atmosphere OTF and the telescope OTF. For telescopes with $d > r_0$, the atmospheric OTF $(OTF_a(\mathbf{f}))$ dominates and can be calculated. As the complex amplitude of the received wavefront is assumed to be solely dependent on the phase variations across the wavefront (described by the structure function of the atmosphere), the OTF can be described by $D_{\phi_a(r)}$:

$$OTF_a(\mathbf{f}) = e^{\left[-0.5 D_{\phi}(\lambda \mathbf{f})\right]}. \tag{1.7}$$

As mentioned, the PSF, can be found through the Fourier transform of the OTF. Using Equation 1.7 the Full Width Half Maximum (FWHM), β, of the PSF can be found as a function of r_0:

$$\beta = 0.98\frac{\lambda}{r_0}. \tag{1.8}$$

With $r_0 \propto \lambda^{6/5}$ we find $\beta \propto \lambda^{-1/5}$. This indicates that the dispersion of the FWHM over a waveband will be small, but that seeing values improve with longer wavelengths.

The Kolmogorov structure function assumes that wavefront distortions contain contributions from all spatial scales out to infinity. In reality there is an outer scale, L_0, beyond which, negligible energy is added into the system. The value of L_0 varies with time and location, known to be as large as 1km and as small as 1m for different sites (Hardy, 1998). Reducing L_0 to a finite size reduces the effects of turbulence on the seeing. If L_0 is only ten times the telescope diameter, the effects of tilt decrease to 60%. If L_0 is only slightly larger than the size as the telescope, Equation 1.8 no longer holds and the FWHM value will be less.

Structure Refractive Index Constant

At each layer in the atmosphere, the structure function is defined by the structure refractive index constant, C_N, which is dependent on the energy of the system at a given altitude. The term “constant” is rather deceptive as it is highly variable on time scales of seconds to hours, through seasons, and in different locations. r_0 is found by integrating over the optical path, and is dependent on the path length, zenith angle, and C_N, as derived by Fried (1966):

$$r_0 = \left[0.423k^2\left(cos\zeta\right)^{-1}\int C_N^2\left(h\right)dh\right]^{-\frac{3}{5}}, \tag{1.9}$$

where k is the wave number and ζ is the angular distance of the source from the zenith. All variables are known for an observation except C_N^2. From measurements of the C_N^2 profile of the atmosphere, values of r_0 (thus the expected seeing conditions) can be determined.

Knowing C_N^2 as a function of altitude can inform which altitudes have the strongest influence on seeing. This is extremely important for ’wide-field’ AO instruments, which remove optical aberrations from the strongest turbulent layers in the atmosphere. There are a host of instruments, described below, which carry out these measurements.

The wind speed at a particular altitude, $V_{wind}(h)$ along with the altitude dependent C_N^2 profile determine the Greenwood frequency, f_G, which calculates the frequency at which turbulence is changing (Greenwood, 1977):

$$f_G = \left[0.102k^2 sec\left(\zeta\right)\int_0^{\infty} C_N^2\left(h\right) v^{\frac{5}{3}}\left(h\right) dh\right]^{\frac{3}{5}}. \tag{1.10}$$

Fried (1990) found that the mean-square change in the measured wavefront distortion for two measurements made at Δt apart is given by:

$$\sigma_\tau^2 = \left(\frac{\Delta t}{\tau_0}\right)^{\frac{5}{3}}, \tag{1.11}$$

where τ_0 is referred to as the Greenwood time constant. For an AO system to apply adequate corrections, the system response must be $< \tau_0$, which for astronomical sites is typically a few milliseconds. The lower the wind speed at a telescope, the better the performance of the adaptive optics.

1.2.3 Wavefront Sensing and Atmospheric Profilers

Determining the sources of image degradation is vital for instrument calibration and for developing future technologies. WaveFront Sensors (WFS) determine the aberrations in an optical system, while atmospheric profilers inform the influence of atmospheric turbulence. Current instruments performing these tasks are described in this section.

Shack-Hartmann wavefront sensor

A Shack-Hartmann WaveFront Sensor (SHWFS) is commonly used for measuring phase aberrations. An array of lenses, conjugated to the pupil-plane, divide the telescope pupil into sub-apertures, bringing the light from each of these to an independently focused image (as seen in Figure 1.4). A plane wave will create a grid of equidistant focal spots, while a distorted wave will contain phase fluctuations which alter the spot positions. The spot positions are used to determine the local wavefront gradients which are reconstructed to describe the whole wavefront. The resolution at which phase variations can be measured across the wavefront is determined by the number of lenslets across the aperture. The number of lenslets is often determined by the likely signal-to-noise ratio as enough photons must reach each sub-aperture per exposure to determine the spot position.

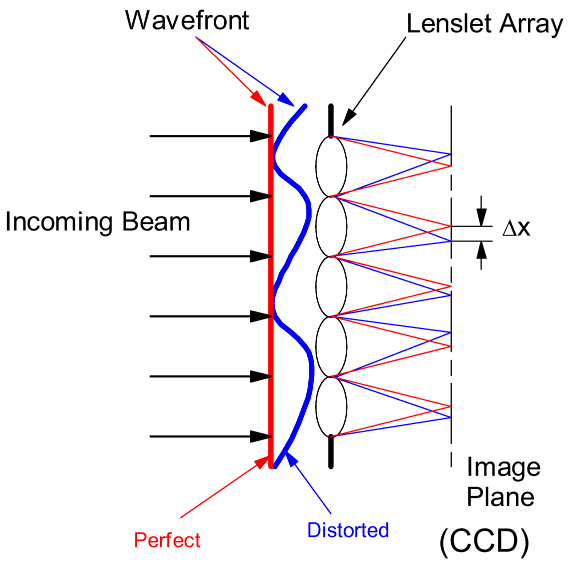

Figure 1.4: Principles of a Shack-Hartmann wavefront sensor.

1.2.4 Curvature WFS

Curvature WFS (CWFS) use two out-of-focus images before (intra-focal) and after (extra-focal) the focal point (see Figure 1.2.4). Any curvature in the wavefront will result in a intensity pattern seen at the intra- and extra-focal points which are used to reconstruct the wavefront. The intensity seen in the extra-focal image, I_2 in Figure 1.2.4, will be the opposite seen at the intra-focal point. The normalised difference between the two intensity fields is used to reconstruct the wavefront. Theoretically, only one out-of-focus image is required, however, using both provides the benefit of removing systematic errors such as readout and detector noise, while also cancelling out any small scintillation effects.

Unlike a SHWFS, A CWFS detects modal aberrations and while high order aberrations can be detected, it is better at detecting lower order terms. AO systems which use CWFS arrange the DM actuators in a circular fashion, rather than the grid used by SHWFS. Instead of requiring two imaging systems to obtain the intra- and extra-focal images, a membrane which alternates between the two is employed. The focal lengths are altered at a frequency of ~1kHz.

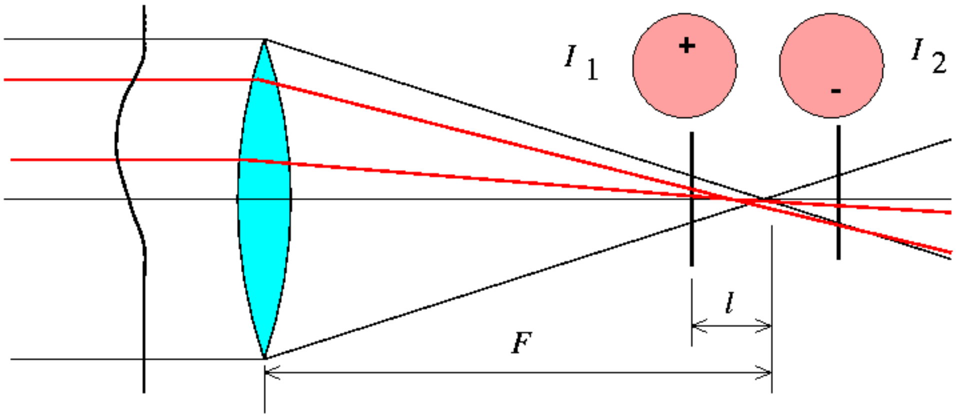

Figure 1.5: A curvature wavefront sensor. Courtesy of Dr. Andrei A. Tokovinin

1.2.5 Pyramid Wavefront Sensors

Pyramid WFSs (PWFS) works on the principle of the Foucault knife-edge test, with a pyramid lens placed at the focal point, splitting the beam into four separate images which are re-imaged at the pupil plane. Any distortion in the wavefront will cause the ray to fall onto one of the four sides, increasing the intensity in one sub-aperture and hence causing a reduction in the another three. The aberrations in the wavefront can be determined from the intensity patterns over the four sub-apertures. It is similar to a SHWFS by splitting the beam into sub-apertures, but similar to a CWFS in that it detects modal aberrations. PWFS show promising improvements over SHWFS in that only four sub-apertures are required, reducing the number of photons required for reconstructing the wavefront. This will allow fainter magnitude stars to be used as guide stars to remove atmospheric effects.

DIMM - Differential Image Motion Monitor

DIMM instruments are used to measure seeing values arising from atmospheric turbulence. Light from a bright star travels through two circular apertures at the entrance pupil plane. A dual star is created at the image plane, and using a quick frame rate, the variance of image motion is recorded. The variance of the differential motions between the dual stars removes any contribution from telescope tracking error, vibrations, or small focus errors. The variance of the differential motion is indirectly proportional to r_0 and hence the seeing (Sarazin & Roddier, 1990):

$$\sigma_{xy} = 0.36\lambda^2 D^{-\frac{1}{3}} r_0^{-\frac{5}{3}} \tag{1.12}$$

If the separation between the apertures becomes larger than r_0, then the motion of the two stars becomes uncorrelated and r_0 can no longer be determined. DIMM instruments can only measure the seeing conditions, they are not sensitive to turbulence strength at varying altitudes and so cannot record C_n^2 profiles. They have been used for many years at a wide number of telescope sites to give an idea of the conditions when an observation was taken.

SCIDAR - SCIntillations Detection And Ranging

SCIDAR instruments use two close stars, with an angular separation of ρ to determine atmospheric turbulence strength. Figure 1.6 provides a schematic of how SCIDAR works. A turbulent atmospheric layer at an altitude of h will create two scintillation patterns, separated by a distance $d = \rho h$, at the pupil plane. An autocorrelation function finds the separation of the repeating section of the scintillation pattern between stars over a number of images. The average separation in peaks is used to calculate the

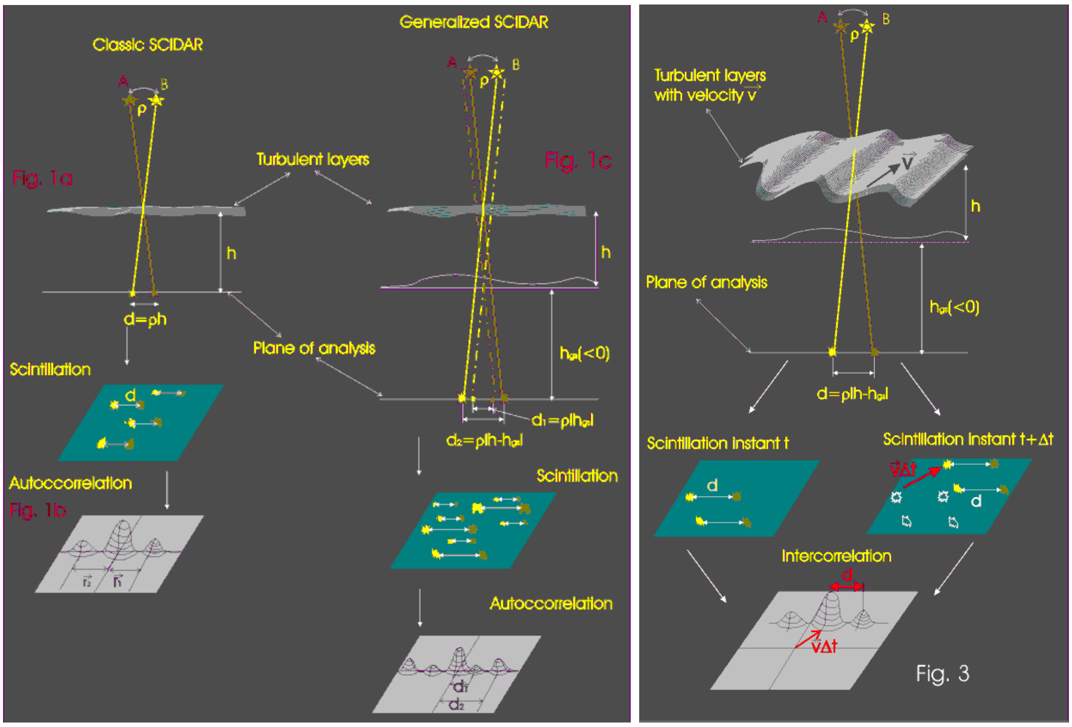

Figure 1.6: Diagrams explaining the principles of SCIDAR. Courtesy of the Instituto de Astronomia, Universidad Nacional Autonoma de Mexico (UNAM).

height of the turbulent layer, while the variations in separation are used to calculate the strength of the turbulence at that altitude.

The velocity of the turbulence can be measured using the variations in position of the scintillation patterns from image to image. If each image has an exposure time of Δt, the patterns will move a distance of $v_w \Delta t$ from the correlation centre from one image to the next as an airmass travels horizontally. Since Δt is a known parameter, the wind velocity v_w can be deduced.

SLODAR - SLOpe Detection And Ranging

SLODAR works in a similar manner to SCIDAR, using the separation between two stars (the angle θ in Figure 1.7) to determine the atmospheric turbulence strength at various layers. The local gradients across a wavefront at the pupil plane are measured using a SHWFS. Computing the cross-correlation of focal spot positions between the two stars within the different sub-apertures determines the influence of each atmospheric layer. The influence of L1 (in Figure 1.7) can be determined if patterns A1 and B1 are correlated. Any similar movements between A1 and B2 will be attributed to the overlap of L1 and also the overlap in L2.

The atmospheric resolution, δh, (or separation between the central position of each altitude layer) is dependent on the number of sub-apertures, n_{sub}, and the angular separation between the two stars, θ:

$$\delta h = \frac{(D/n_{sub})}{\theta}. \tag{1.13}$$

The maximum altitude resolution achievable is set by the FoV of the optical system, with larger angular separations resulting in higher resolution (see Figure 1.7). The maximum altitude probed is also dependent on θ as well as the telescope diameter, D:

$$H_{max} = D/\theta. \tag{1.14}$$

The wind velocities of individual turbulent layers can be found in the same manner as used for SCIDAR, using the time delays between images and tracking the turbulence from a particular airmass across the FoV. The SHWFS exposure times must be short enough to record ’frozen’ turbulence, i.e. faster than the crossing time for the fastest expected wind speed over a sub-aperture. High wind velocities generally exist at higher altitudes, limiting the altitude at which SLODAR measurements can be taken. As turbulence is usually strongest in the surface layers, high resolution altitude measurements ($\delta <$1km) are usually favoured, at the sacrifice of maximum altitude.

MASS - Multi-Aperture Scintillation Sensor

MASS instruments measure the turbulence profile from scintillation patterns from a single star (Kornilov & Tokovinin, 2001) in which the spatial fluctuations in intensity are dependent on the altitude of the turbulence causing them. Using this premise, Tokovinin & Kornilov (2002) devised a system of concentric ringed apertures (photon

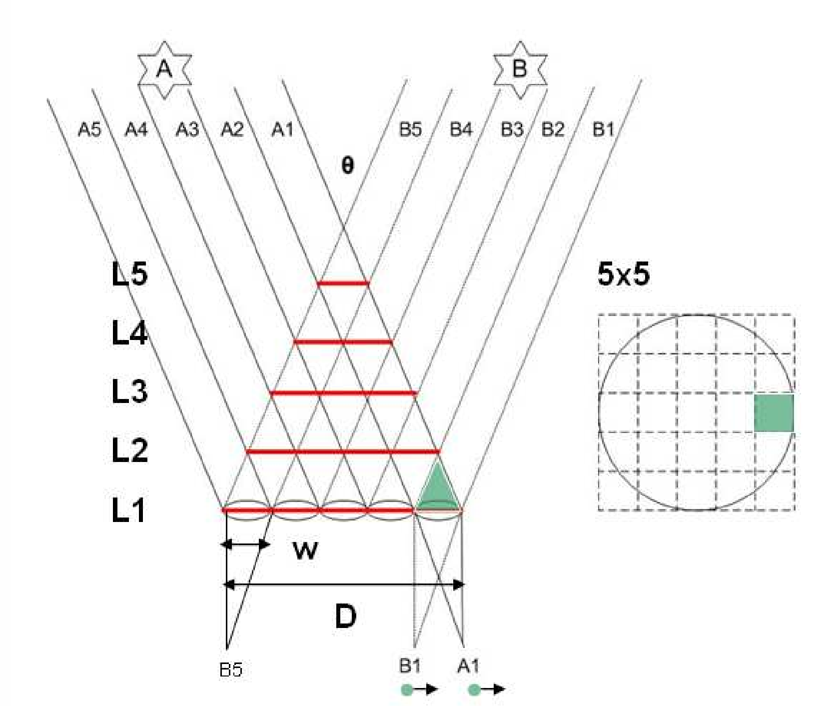

Figure 1.7: Diagram illustrating the principles of SLODAR. θ is the angular separation between stars, *w* is the sub-aperture size, *D* is the pupil diameter, and *L#* refers to atmospheric layer. Courtesy of Michael Goodwin, Research School of Astronomy & Astrophysics, The Australian National University.

counters in this case) to separate the contributions from different layers. A weighting function of an atmospheric layer contribution to each aperture is calculated and used to determine the strength of atmospheric turbulence at each layer.

1.2.6 Anisoplanatism

The value of r_0 not only informs of the resolution of a large telescope, but also gives an idea of the quality of corrections achievable when using an AO system. When using a Guide Star (GS) for mapping turbulence, it is likely that the optical path of the GS differs in some way from that of the science object. Atmospheric turbulence varies at different altitudes and zenith angles, so the turbulence in any line of sight will differ to the next. If the aberrations were uniform in each direction, then the atmosphere

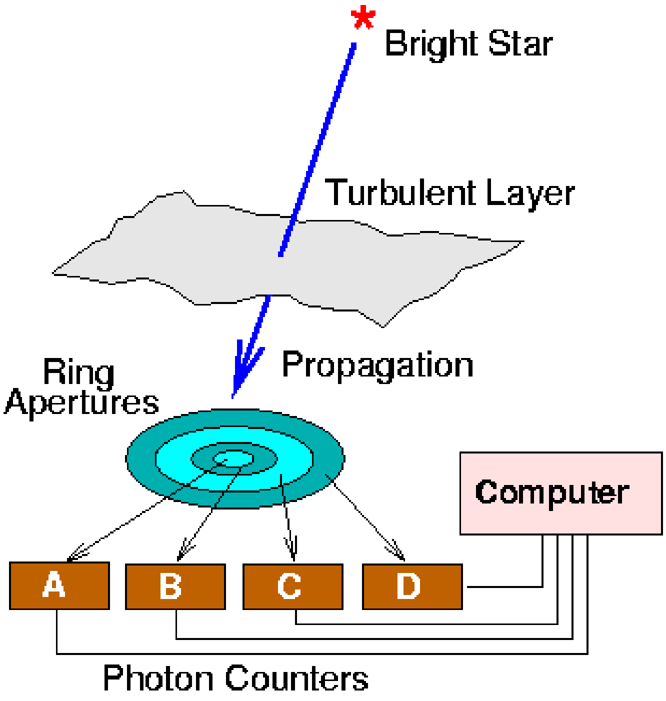

Figure 1.8: A basic description of MASS. Courtesy of A. Tokovinin.

could be considered isoplanatic. Unfortunately this is not the case, the atmosphere is anisoplanatic. The GS used to measure phase fluctuations can be naturally occurring (i.e. bright stars within the FoV), or artificially created. There are various different forms of anisoplanatism, all arising from the fact that GS are not measuring the same exact turbulence path as the science source (except point like science targets bright enough to be used as their own GS). Anisoplanatism largely influences the design of an AO system. For classical AO systems it limits the FoV over which corrections can adequately be applied.

Angular Anisoplanatism

An angular separation between the GS and the science object results in angular anisoplanatism, as illustrated in Figure 1.9. If most of the turbulence is generated in the surface layers near the pupil, a lot of the turbulent effects can be removed, even for a large separation. However, if turbulence in the upper atmosphere is dominant, good correc-

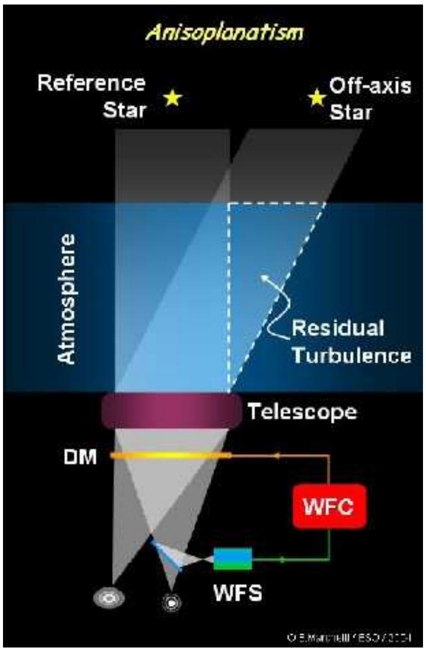

Figure 1.9: Illustration of angular anisoplanatism, courtesy of E. Marchetti, ESO.

tions can only be made when the offset between the objects is small. As the angular separation between the GS and science object increases, the wavefront errors become decorrelated. The isoplanatic angle, θ_0, is defined as the angular separation at which the mean-square wavefront error, averaged over a large aperture, is 1 rad^2 (Hardy, 1998). When C_n^2 is known for the whole path length, L, θ_0 can be defined in terms of r_0:

$$\theta_0 \approx 0.6 \left(\frac{r_o}{L}\right), \tag{1.15}$$

where the mean-square wave error is expressed by

$$\sigma_{iso}^2 = \left(\frac{\theta}{\theta_0}\right)^{\frac{5}{3}}. \tag{1.16}$$

Angular anisoplanatism is one of the largest difficulties facing AO (Hardy, 1998). Natural Guide Stars (NGS) are often used to measure wavefront distortions. They are required to be bright enough for wavefront sensing and within the angular distance θ_0 of the science object. In the optical, θ_0 ≈2" for average conditions. Assuming that a star of m_v <10 is required for WFS, coverage is limited to ∼0.001% of the hemisphere (Hardy, 1998). In the N-IR, values of r_0 and θ_0 increase and so ∼0.1% of the sky has a NGS in sufficiently close proximity. Clearly this is not ideal and not practical for most science cases. The problem can be overcome with the use of artificial guide stars.

Laser Guide Stars

There are two forms of Laser Guide Stars (LGS), sodium LGS and Rayleigh LGS. Sodium LGS take advantage of a thin layer of sodium atoms that exists high in the mesosphere (at ∼90km), deposited by meteors (Hardy, 1998). Atoms are stimulated by a laser specifically tuned to the 589.2nm sodium D_2 line. The excited sodium atoms decay back to the ground state, emitting light and producing an artificial beacon high in the atmosphere. A laser power of ∼10W is required to create the artificial stars.

Rayleigh LGS rely on backscattering off molecules in the atmosphere. The amount of light backscattered is dependent on the air density and so decreases with altitude. This generally limits Rayleigh LGS to operating up to an altitude of ∼20km. Backscattering occurs at all altitudes and so to measure the turbulence to a particular altitude the lasers are pulsed. Rayleigh scattering is less efficient than creating sodium beacons and so more powerful lasers are required (e.g, the system on the WHT used a 25W Rayleigh LGS (Rutten et al., 2003)). Sodium atoms are excited by only one wavelength, hence the lasers are difficult to produce. Although more powerful lasers are required for Rayleigh scattering, the relaxing of wavelength dependence means off-the-shelf lasers can be used, which reduces cost.

Focal Anisoplanatism

LGS are created within the atmosphere and the beams trace a cone pattern through the atmosphere, down to the telescope (see Figure 1.10). Star light originating outside the atmosphere travels through regions outside the LGS mapped region, resulting in focal anisoplanatism. This effect is often referred to as the cone effect. The focal isoplanatic

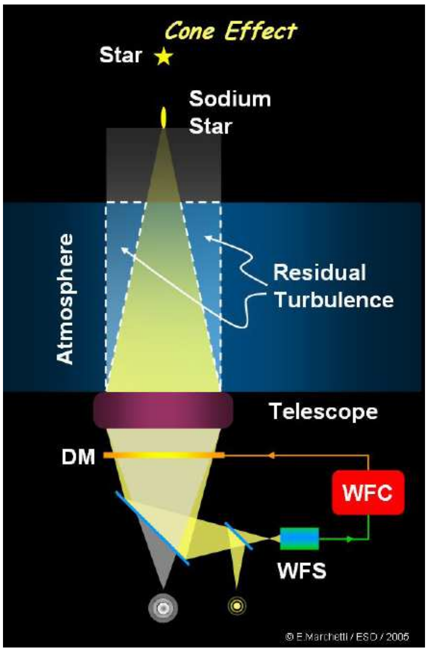

Figure 1.10: Illustration of focal anisoplanatism. Courtesy of E. Marchetti, ESO.

parameter, d_0, is defined such that the mean-square wave error, σ^2_{cone} is 1 rad^2:

$$\sigma^2_{cone} = \left(\frac{D}{d_0}\right)^{\frac{5}{3}}, \tag{1.17}$$

where D is the telescope aperture. The value of d_0 is a function of the LGS altitude, h_{LGS} (in km), and the C_N^2 profile (Tyler, 1994):

$$d_0 = \lambda^{\frac{6}{5}} cos^{\frac{3}{5}}(z) \left[19.77 \int \left(\frac{h}{h_{LGS}}\right)^{\frac{5}{3}} C_n^2(h)\, dh\right]^{-\frac{3}{5}}. \tag{1.18}$$

LGS created lower in the atmosphere lead to large variations between the turbulence experienced by the LGS and the science target, indicating the benefit of using sodium LGS over Rayleigh LGS. The problem can be overcome with Laser Topography Adaptive Optic (LTAO) systems, which use multiple lasers around the science target to sample a larger region of atmosphere. LTAO systems are planned for the ELTs, such as ATLAS for the E-ELT (Fusco et al., 2010), and greatly reduce the cone effect.

1.2.7 Adaptive Optic Techniques

MCAO - Multi-Conjugate Adaptive Optics

Multi-Conjugate Adaptive Optics (MCAO) applies wavefront corrections over a large FoV, overcoming angular anisoplanatism which affects classical AO systems. Multiple GS are detected by multiple WFS, mapping the turbulence across a large area. WFSs are conjugated (focused) to independent layers in the atmosphere, mapping the turbulence at that altitude. The location of an aberration on a WFS is dependent on both the altitude of the turbulence causing it and the angular field location of the WFS. Tomography employs cross-correlation to determine the relation of phase aberrations across the WFSs, using them to reconstruct a 3-D volume of turbulence above the telescope.

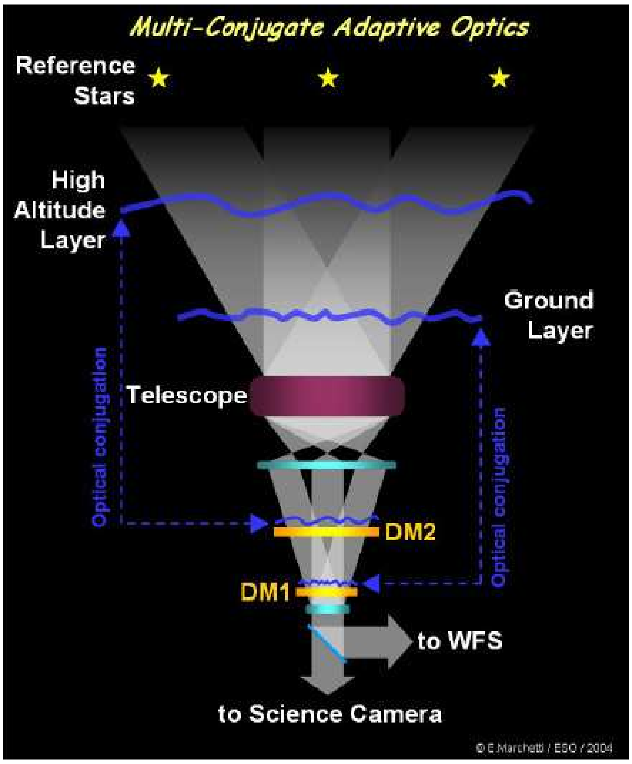

Figure 1.11: Illustration of MCAO principles, courtesy of E. Marchetti, ESO.

Multiple GS map turbulence that would otherwise be missed using a single GS (see Figure 1.11). MCAO usually employs a closed-loop WFS system. This means that the aberrated wavefront is measured and corrections are applied, after which the residual wavefront error is measured and corrected for. A benefit of using a closed-loop system is that the correction performance can be continuously monitored.

Tomography measures the aberrations from the most turbulent layers and Deformable Mirrors (DMs) conjugated to these layers apply corrections. Ideally there is a DM conjugated to each strong turbulence layer. Applying corrections for an atmospheric layer at its conjugate makes the correction accurate for all field positions. If a mirror is conjugated to an altitude of 5km, but the main turbulence contribution occurs from a ground layer, the applied corrections will not be accurate. This highlights the necessity to carry out extensive atmospheric measures with atmospheric profilers (see Section 1.2.3) at a potential telescope site before the telescope or instruments are designed.

MCAO technology has been shown to be capable of science grade results, e.g. on the Very Large Telescope (VLT) with the Multi-conjugate Adaptive optics Demonstrator (MAD). On-sky performance and scientific exploration of MAD observations are described in Chapters 2 & 3, respectively.

GLAO - Ground Layer Adaptive Optics

Long-term monitoring of the atmosphere above telescope sites has found that a significant fraction of turbulence resides in the lowest atmospheric regions, just above the telescope. A two year study by Els et al. (2009) at potential sites for the Thirty Meter Telescope (TMT) found that, at all of the sites, the lowest 200m of the atmosphere is the main source of the total seeing observed. Ground Layer Adaptive Optics (GLAO) corrects for turbulence generated in these low surface layers, improving seeing over a wide FoV (Rigaut, 2002). It works on the same principle as MCAO, using multiple GS to measure distortions, having only a single DM conjugated to the ground layer (see Figure 1.12). Not having to correct for a high altitude layer means a wider FoV can be compensated for. GLAO does not correct for all turbulence and so it only improves seeing, never reaching the diffraction limit. GLAO instruments are currently being constructed, such as the Ground layer Adaptive optics Assisted by Lasers (GRAAL)

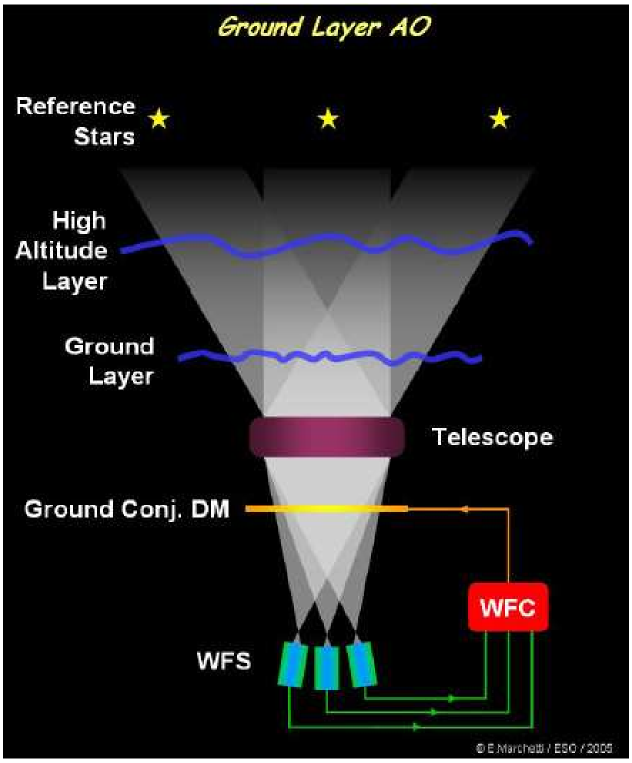

Figure 1.12: Illustration of GLAO principles, courtesy of E. Marchetti, ESO.

to be installed on the High Acuity Wide field K-band Imager (HAWK-I) on the VLT (Casali et al., 2009).

MOAO - Multi-Object Adaptive Optics

Multi-Object Adaptive Optics (MOAO) applies wavefront corrections to targets across a large FoV. However, instead of correcting for the whole field like MCAO, corrections are applied along the line-of-sight of the target object. Tomography calculates the turbulence above a particular science target from multiple surrounding GS (see Figure 1.13). Each target has an individual DM covering a small FoV, typically on the order of a few arcsec (Morris et al., 2010). MOAO systems are more practical over larger FoVs than MCAO as the corrections are optimised for a single atmospheric slice. Wave aberrations are mapped using a combination of NGS and LGS. The DMs are controlled in open-loop, i.e. the WFS do not observe the corrected wavefront then make the necessary adjustments, as a closed-loop system does. Open-loop systems directly apply the corrections measured from the incoming aberrated wavefront. In such a setup the system performance is unmeasured and accurate characterisation and calibration is required to ensure confidence in results. The benefit of using WFS in open-loop is that the system has a quicker temporal response. This allows longer exposure times and so more NGS become available at fainter magnitudes across the sky. There are several MOAO instruments currently in the design stage for ELTs, while on-sky demonstrators are currently under development (Morris et al., 2010). The work in Chapter 5 is toward the CANARY demonstrator being developed for the William Herschel Telescope in La Palma.

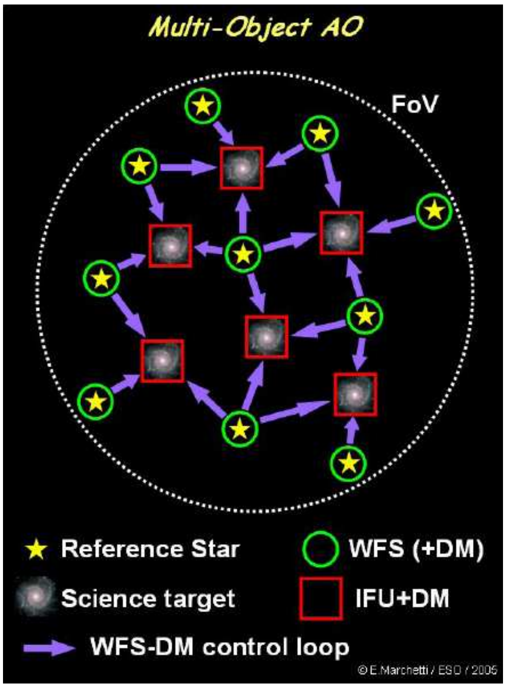

Figure 1.13: Illustration of MOAO FoV. The light-of-sight aberrations for each science target are mapped using the multiple surrounding GS. Courtesy of E. Marchetti, ESO.

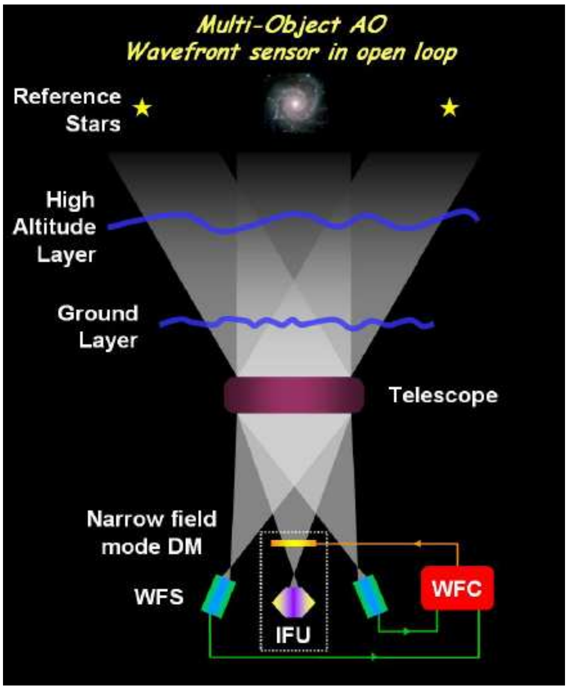

Figure 1.14: Illustration of MOAO principles, courtesy of E. Marchetti, ESO.

Table 1.1: Characteristic dimensions of the LMC and 30 Dor. From Walborn (1991)

Name	Class	Angular Extent	Linear Extent (pc)
LMC	Galaxy	5°	5000
30 Dor region	complex	1°	1000
30 Dor nebula	HII region	15’	200
NGC 2070	Stellar cluster	3’	40
R136	Stellar core	10"	2.5

1.3 30 Doradus

Chapter 2 presents science verification data from the VLT MCAO pathfinder, MAD, to investigate the on-sky performance of the system. After gaining confidence in the data reduction and calibration methods, the data is used in Chapter 3 to investigate the processes at work in R136, the dense stellar cluster at the core of 30 Doradus. The cluster is now briefly introduced.

30 Doradus (30 Dor), otherwise known as the Tarantula Nebula or NGC 2070 is situated in the LMC. It was initially thought to be a star, until Nicolas Louis de Lacaille reclassified it as a nebula in 1751. Since then, 30 Doradus has been determined to be the largest star-forming region in the Local group and, at a distance of ∼50kpc is close enough for us to resolve its components. Characteristic dimensions of the LMC and 30 Dor were summarised by Walborn (1991) and are displayed in Table 1.1

As a proto-typical, ’small-scale’ star burst, 30 Dor provides an excellent laboratory in which to study star formation and stellar evolution. Furthermore, the resolved data can be projected to larger distances, providing insight on how we should interpret the nature of distant super-star-clusters, for which we have only integrated light properties.

Extensive ground-based, optical imaging and spectroscopy have been carried out, studying the Initial Mass Function (IMF), reddening, star-formation history, stellar content and kinematics in 30 Dor. The *Hubble Space Telescope*, (*HST*), has also carried out extensive observations in the optical and in the N-IR (thus penetrating through the dust better), illuminating the different populations that exist within 30 Dor. A detailed analysis of the different populations has been carried out by Walborn & Blades (1997).

1.3.1 R136

At the centre of 30 Doradus lies the ionising cluster R136 (just below the centre of the image in Figure 1.15). Said to be in the “Carina phase”, the age of the cluster is thought to be $\sim$1-4Myr, with the most massive stars in the range of 1-2Myr (Massey & Hunter, 1998). The total stellar mass of the cluster is $\sim$0.35-1$\times 10^5$ $M_\odot$ (Mackey & Gilmore, 2003; Noyola & Gebhardt, 2007; Andersen et al., 2009) depending on the low-mass form of the mass function. This puts it on a par with some of the massive clusters in star-burst, interacting galaxies such as M51, M82 and the Antennae. Little primordial gas remains in the cluster, presumably having been removed by the massive O-type stars. The young age of the cluster means that few, if any, supernovae have occurred yet.

The core of R136 is too dense for traditional (seeing limited) ground-based techniques. Only with the arrival of *HST* was R136 resolved in optical and UV images (Campbell et al., 1992; de Marchi et al., 1993; Hunter et al., 1995, 1997; Sirianni et al., 2000), with follow-up spectroscopy revealing a hitherto unprecedented concentration of the earliest O-type stars (Massey & Hunter, 1998). $\sim$40 stars of spectral type O3 were discovered making it the most dense concentration of massive stars known. Massey & Hunter concluded that the high and intermediate-mass IMF of R136 is ’completely normal’ i.e., Salpeter-like.

With the advancement of AO, ground-based observations have been able to resolve the core of R136. AO-corrected, N-IR images were taken with the ESO 3.6-m telescope instrument, COME-ON+ (Rousset et al., 1994). COME-ON+ was the first AO system open to the astronomical community. One reference star within the isoplanatic patch was used to measure the atmospheric turbulence. The nature of the technology resulted in a FoV restricted to $12\overset{''}{.}8$x$12\overset{''}{.}8$, with the corrections deteriorating away from the reference star. When combined with *HST* data, the COME-ON+ images were

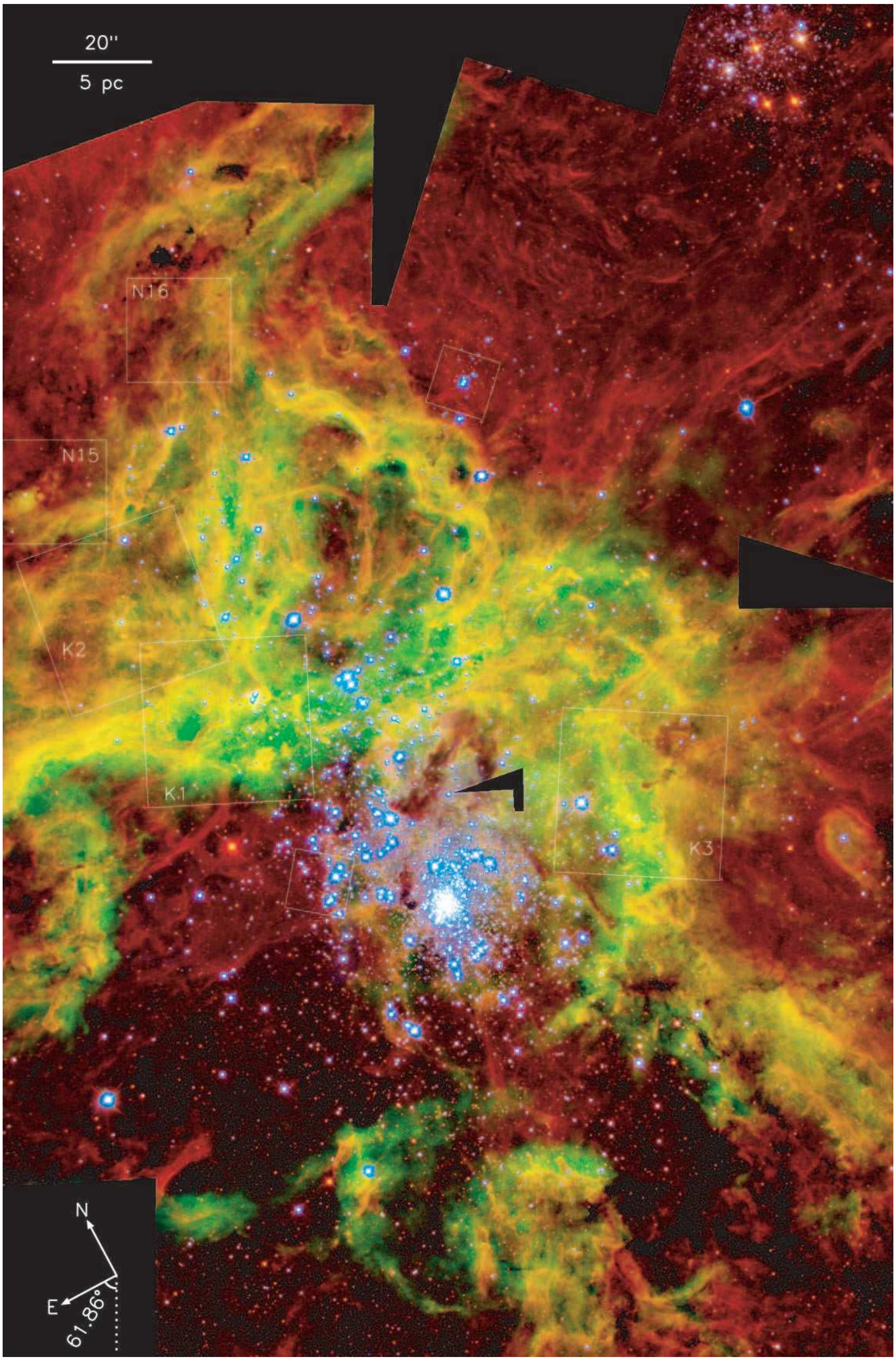

Figure 1.15: A mosaic of WFPC2 images of 30 Dor, from Walborn & Blades (1997). Blue: U-band; green: $\mathrm{H}\alpha + V$; red: [S II] $+I$. The yellow regions indicate where the central cavity interacts with the surrounding molecular cloud.

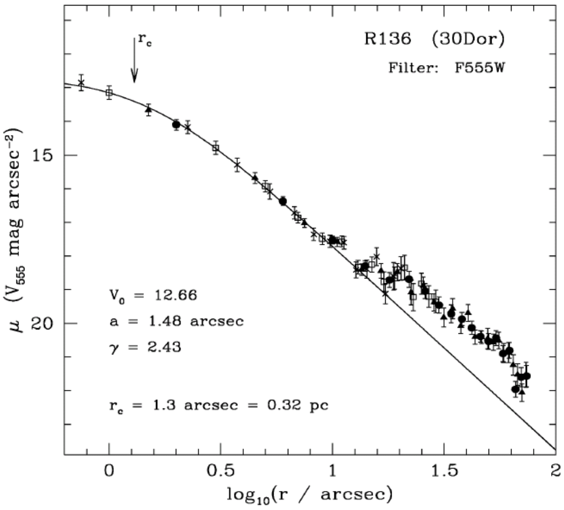

Figure 1.16: *HST* optical surface brightness profile of R136 from Mackey & Gilmore (2003).

used to determine the average slope of the mass function to be $\Gamma = -1.6$ (Brandl et al., 1996).

Star counts from the optical *HST* images revealed that the luminosity profile of R136 appears to be best described by two components, with a break at 10" (see Figure 1.3.1), (Mackey & Gilmore, 2003). New results from *F160W* imaging (equivalent to the H-band) with the *HST* Near Infrared Camera and Multi-Object Spectrometer (NICMOS) fit the profile with a single component (Andersen et al., 2009), but only in the inner 2 pc ($8\farcs25$).

It is possible that the break in the radial profile seen by Mackey & Gilmore (2003) in the optical data is a manifestation of the ‘excess light’ predicted to originate from Rapid Gas Expulsion (RGE) in the early stages of cluster evolution (see Section 3.1.1). However, this is difficult to assert due to the significant and variable extinction across the cluster. By penetrating through the gas in the N-IR, the high angular resolution of MAD will determine if the excess light is wavelength independent as expected by simulations of RGE.

1.3.2 30 Doradus Stellar Populations

Surrounding R136 are knots and filaments that appear heated and structured by the outflows from R136. The discovery of embedded Young Stellar Objects (YSOs) to the north, north-east, and west of the cluster (Hyland et al., 1992; Rubio et al., 1992, 1998; Brandner et al., 2001) suggests a new stellar generation in the so called 'Orion phase'. Due to the morphology of the surrounding filaments, Walborn & Blades (1997) concluded that the new star formation has been triggered by the ionising core, R136. They also detected IR sources to the south and east of R136 but concluded that they likely belong to the Carina phase. The Orion phase objects have characteristics which suggest ages of $<$1Myr.

The central region of 30 Dor also contains a population of OB supergiants described as in the 'Scorpius OB1 phase'. Having already evolved into supergiants, their ages appear to precede the formation of R136, corresponding to 4-6Myr (Walborn & Blades, 1997). To the northwest of 30 Dor resides an older cluster, Hodge 301 (located in the top right corner of Figure 1.15). Hodge 301 is the predominate "old" cluster in 30 Dor, at least 10 times older than R136 at an age of 20-25Myr (Grebel & Chu, 2000). At this age, many of the massive stars have reached the end of their lives, with Grebel & Chu (2000) suggesting that $\sim$40 stars may have already gone supernova. The ejecta from these supernovae cause turbulent motions in the gas surrounding the cluster. Walborn & Blades (1997) highlight another Scorpious OB1 phase called R143 in the south-east of 30 Dor containing late O- and early B-type stars of ages 4-7Myr.

Walborn & Blades (1997) conclude that there are many different populations within 30 Dor, which have not formed coevally. The five visibly distinct stellar populations within 30 Dor indicate a complex interconnection between the different regions, some being completely independent, while others are actively triggering new regions of formation. These populations are discussed further in Chapter 4.

Chapter 2

The Multi-conjugate Adaptive optics Demonstrator (MAD)

The development of MCAO technologies and techniques is seen to be crucial for the development of ELTs. As part of the technology development plan for the European Extremely Large Telescope (E-ELT), MAD was developed as a visiting instrument for the VLT (Marchetti et al., 2007). This chapter describes science verification observations of R136 in 30 Doradus with MAD.

2.1 MAD Introduction

MAD utilises three SHWFS to observe three natural guide stars (NGS) across a $2'$ circular field, thereby allowing mapping of the atmospheric turbulence. The turbulence is corrected using two deformable mirrors (operating at $\sim$400 Hz), one conjugated to the ground-layer (i.e. 0 km), the second conjugated to 8.5 km above the telescope. Figure 2.1 shows the optical layout of MAD.

The high-resolution, near-IR camera utilised by MAD is the CAmera for Multi Conjugate Adaptive Optics (CAMCAO) operating over the J, H, and K_s-bands, with critical (2 pixel) sampling of the diffraction-limited PSF at 2.2μm. The detector is a HAWAII2 2k$\times$2k HgCdTe array, with 0.028" pixels, giving a FoV of 57x57". A useful

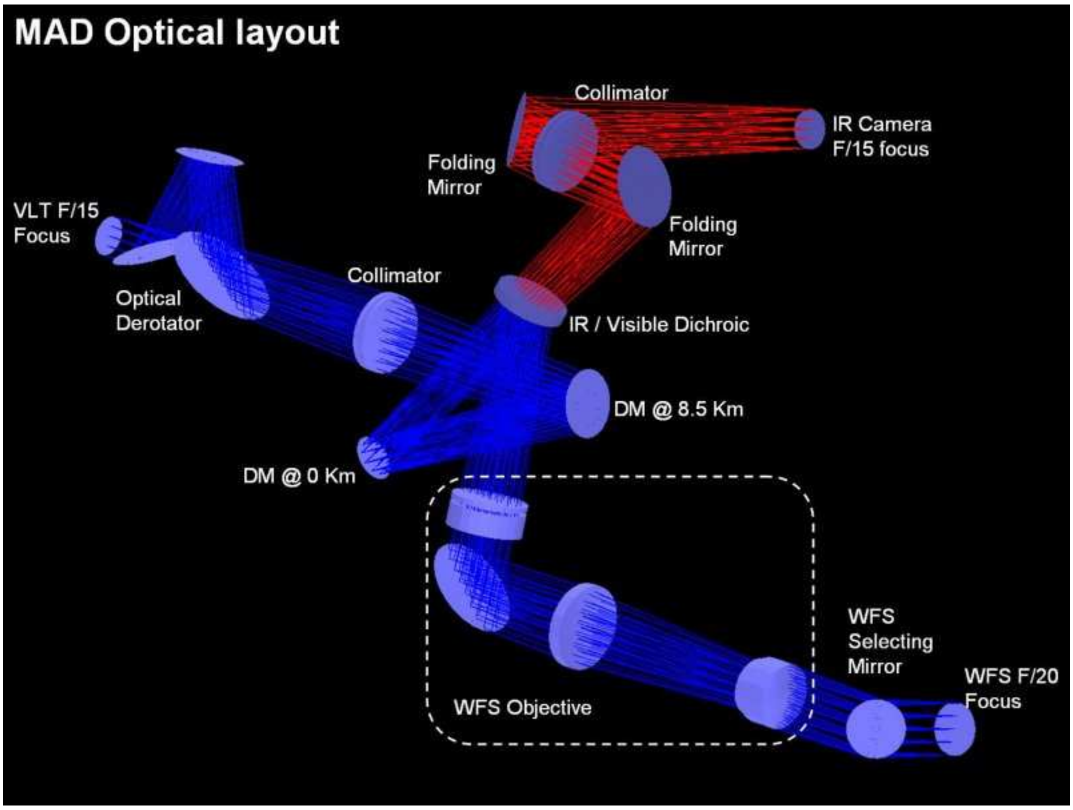

Figure 2.1: Optical layout of MAD, courtesy of ESO.

feature is that the camera can be moved within a $2'$ diameter field without requiring positional offsets of the telescope, meaning that the AO loop can remain closed.

2.2 MAD Data - Part I

2.2.1 Observations and Reduction Techniques

Three fields of R136 were observed in both the H & K_S-bands. Fields 1 & 3 overlapped such that the full cluster core was observed (see Figure 2.2). In order to measure the atmospheric turbulence efficiently, the NGS were required to be brighter than m_{ν} =12. Magnitudes fainter than this leads to a drop off in performance (Marchetti et al., 2007). The minimum allowable separation between the NGS is 15", with the best corrections occurring next to the NGS and within the triangle created by them.

An asterism with NGS of similar magnitude, separated uniformly around the periphery of the FoV was recommended. These conditions were met with stars Parker #952 (NGS1), #499 (NGS2) and #1788 (NGS3) making a triangle around Fields 1 & 2, with m_V=12.0, 11.9, 12.0 respectively (Parker, 1993). The magnitudes were on the recommended faint magnitude limit. Although brighter NGS are preferable, these were the only potential NGS in this region. Field 3 was slightly outside the asterism, containing only NGS2 in the top corner of the field. The variety of NGS orientations within the fields provides an excellent opportunity to analyse the MCAO performance in various conditions.

The LMC never rises above an altitude of approximately 45° as viewed from Paranal (i.e. the *minimum* zenith distance of the observations was ∼45°) resulting in a relatively high airmass over the course of the observations, ranging from 1.4-1.6.

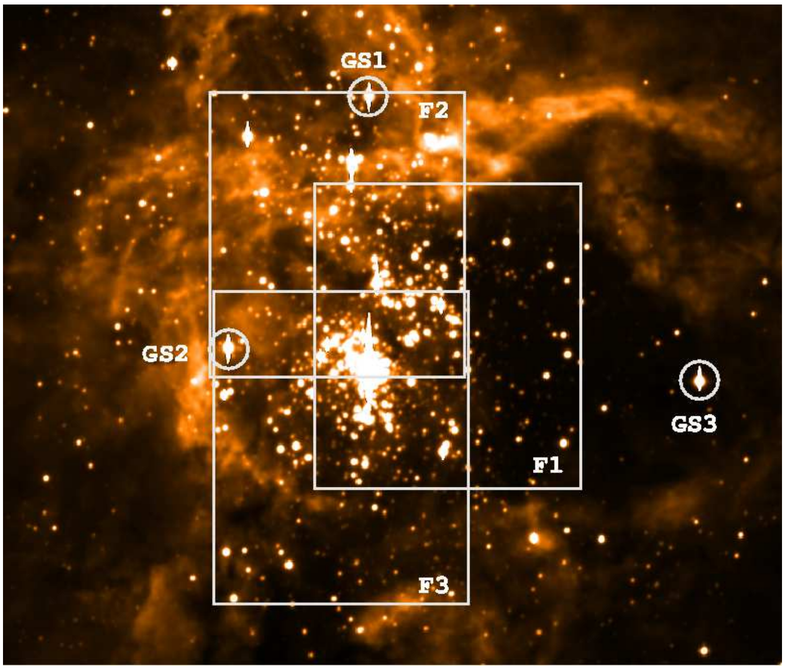

Figure 2.2: 2.2m Wide Field Imager (WFI) V-band image of the 30 Dor region. Rectangles indicate the MAD coverage. Circles indicate the NGS used. East is to the right, north is to the top.

The MAD FoV was centred on α = 5:38:47, δ = -69:05:54 (J2000.0). The detector

Table 2.1: Summary of MAD observations and image quality in 30 Doradus. The total exposure times quoted are for the final combined images.

Band	Field	Total Exp. [min]	DIMM [$''$]	FWHM [$''$]	<FWHM> [$''$]	Strehl ratio	<Strehl ratio>
K_s	1	22	0.4-1.8	0.10-0.13	0.11	10.0-15.0	12.5
K_s	2	24	0.5-1.1	0.08-0.10	0.09	15.0-30.0	22.5
K_s	3	23	0.6-1.0	0.10-0.20	0.14	5.0-25.0	12.5
H	1	12	0.3-0.6	0.10-0.12	0.11	-	-
H	2	12	0.9-1.1	0.08-0.11	0.09	-	-
H	3	11	0.6-1.6	0.08-0.15	0.12	-	-

integration time (DIT) for all of the observations was 2s, with 30 integrations (NDIT) for each exposure. Batches of three (H) and six (K_s) object and sky frames were interleaved in an ABABA pattern, yielding total exposures of 12 min for each field in the H band, and 24 min in K_s. The science exposures within each batch were each dithered by $5''$. Although this reduces the effective area of the combined images, it minimises the impact of bad pixels and cosmetic features from the array. Given the vast spatial expanse of 30 Dor, the sky offsets were relatively large (+12s of right ascension, $+13'$ in declination) to ensure they were not contaminated by nebulosity.

All of the H-band observations were carried out on the night of 09/01/08 (between UT=01:00-03:30). The seeing conditions, as measured by the Differential Image Motion Monitor (DIMM) at Paranal, ranged between $0\rlap{.}''4$ and $1\rlap{.}''75$ over the observations. The K_s-band images were captured over 3 different nights. K_s Field 3 was completed on the 27/11/07. The other two K_s Fields were planned to be carried out on the 07/01/08, however, due to deteriorating weather conditions, Field 1 was completed on 08/01/08. Although a few frames were affected by bad seeing, on the whole the conditions were good, as summarised in Table 2.1. K_s-band pointing 3 can be seen in Figure 2.3.

2.2.2 Instrument Light Leak

A light leak affected the MAD observations, adding noise to the left-hand side of the images (which was more significant for the K_s-band than those in the H-band). The most notable disruption was caused in Field 1 as it is through the cluster core. The background values in regions contaminated by the light leak are 2-3 times higher than in unaffected regions. The influence of the light leak on the results is incorporated in later sections.

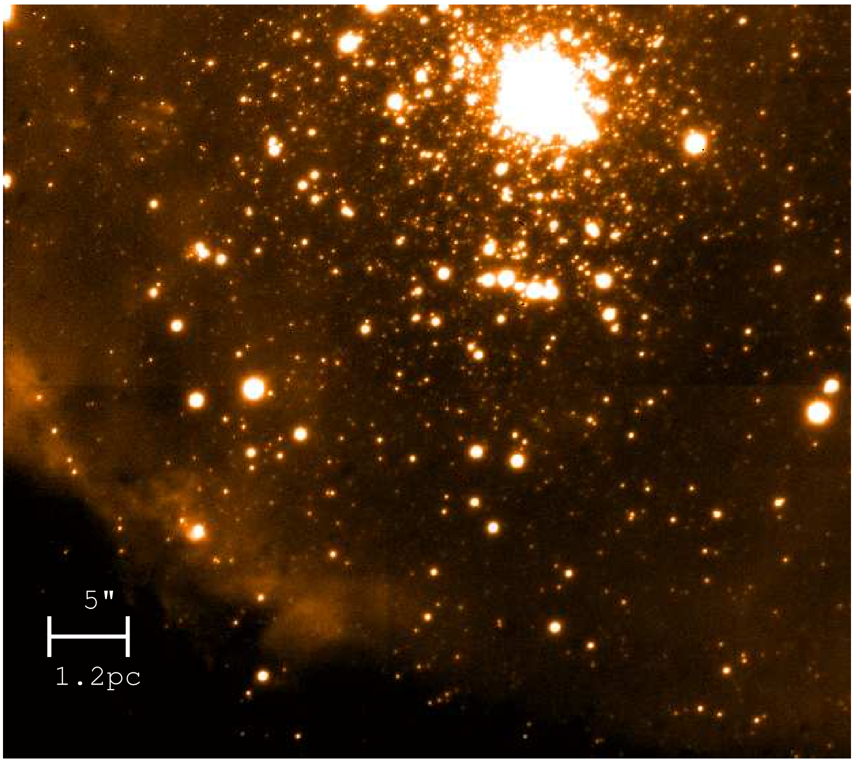

Figure 2.3: R136 K_s-band Field 3.

2.2.3 Data Reductions

The raw data was reduced using DAOPHOT packages within IRAF. Unfortunately flats and darks with the same DIT and NDIT were not available and so other frames available from the Science Demonstration (SD) runs were scaled accordingly when subtracted. Where there were no darks available from the night of observations, darks from the closest possible time were used. The science and sky frames were dark subtracted and flat fielded. The flat fields, taken at twilight in the relevant filters, were dithered, combined, and normalised. Median sky frames were created from the sky observations bracketing the science frames. This was to keep the sky observation conditions as similar to the science frames as possible.

A bad-pixel map was created from the master flat field image using a specifically written `idl` program. Pixels with counts of half the median value or less were mapped onto a FITS file. The IRAF FIXPIX routine then employed linear interpolation from the four surrounding pixels to mask bad pixels. Although dithering usually takes care of bad pixels, this was an extra precaution. Cosmic rays and hot pixels were removed from the individual images using the XZAP routine in DIMSUM.

The individual science frames for each field were aligned with each other and combined. There is a trade-off here between maximising angular resolution, while also probing as faint as possible. With this in mind, only frames recorded under particularly bad seeing conditions were removed, with the remaining frames combined. The seeing conditions for the H-band were typically slightly worse than those for the K_S-band, but they were more consistent. Only one frame was removed for all the H-band observations (in Field 3). The seeing conditions in the K_S-band were generally very good, except for one or two images which were significantly worse and were removed. The combined frames were then cropped so that all regions contained the same number of stacked frames.

The CCDCLIP function within IRAF was turned off when co-adding the science frames as, regardless of how high the cut-off threshold was set, it removed real signal from the centre of the cores of the brightest stars during the stacking process. As most artifacts had been removed through the bad pixel and cosmic ray removal process, few detector artifacts remained. Slight over-subtracted regions can be seen when increasing the contrast in the images, caused by bright objects visible in the sky frames. They are most prominent in the H-band frames as the sky frames were only dithered in the y-axis, causing objects to return to original positions after three shifts. Using the CCDCLIP routine on the sky frames minimised the effect, but did not remove it completely. Masking the sky frames for bright objects might have diminished this effect further, but the effect was small and did not affect the main section of the cluster, i.e, this is mainly an aesthetic issue. Sky values used in photometric measurements were calculated locally and so over-subtracted regions will have had minimal effect on the end photometric values.

2.2.4 Analysis

The FWHM and Strehl ratios see Section 2.2.4) of the objects were measured across the FoV for each combined field. Two different methods were employed to measure the FWHMs. Initially, the PSFs of 32 stars spread uniformly across each co-added image were measured within IRAF. The stars were hand picked as apparently single objects, not saturated, and isolated (within reason in such a crowded field). The sample was as spatially uniform as possible across the fields. For each object, the position, ellipticity, encircled energy, FWHM of the Moffat function, along with its beta value, and the direct FWHM were measured. The radial and contour profiles were also examined. Separately, the FWHM and Strehl ratios were examined using scripts specifically written for the commissioning of MAD by Dr. Johann Kolb. Due to undersampling at shorter wavelengths, Strehl maps could only be produced for the K_S-band. The spatially varying PSFs were found to be best fit by a PENNY2 function. This was measured by creating model PSFs using different fitting models, then finding the average residual difference. The PENNY2 model has a Gaussian core and Lorentzian wings mimicking a partially corrected AO PSF.

FWHM

In general, and as one would expect, the closer to the NGS, the better the corrections, with image quality within the triangle created by the NGSs more uniform. Table 2.1 provides a summary of the results. The FWHM maps are shown in Figures 2.4 &

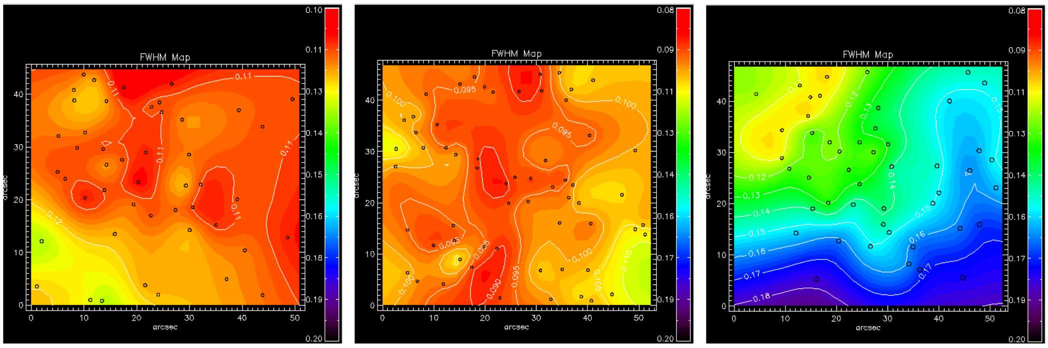

Figure 2.4: K_s-band FWHM (") maps for Fields 1, 2 and 3 (left to right). East is to the right, north is to the top.

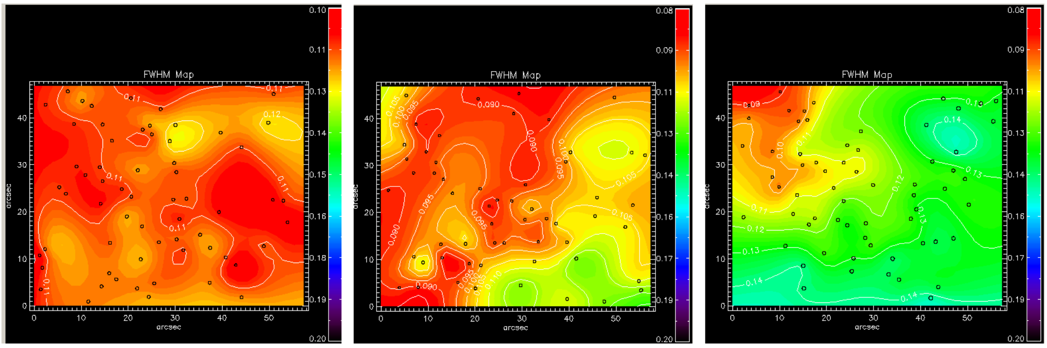

Figure 2.5: H-band FWHM (") maps for Fields 1, 2 and 3 (left to right). East is to the right, north is to the top.

2.5 with black circles indicating stars used in producing the maps. Results from the two FWHM measurement techniques were in agreement. The smallest FWHM values were witnessed in Field 2 in close proximity to the two NGS, and particularly in the regions aligned between the NGSs. The further away from this region, the larger the observed FWHM. The deviation, however, was small, there being a min-max range of 0.″04 across the whole FoV. The corrections were less uniform in Field 3, as expected. In the K_s-band a FWHM of 0.″10 was recorded next to the NGS, deteriorating to 0.″17 in the opposite corner . Field 1 was relatively uniform across the FoV, recording a mean FWHM of 0.″11.

The mean FWHM during MAD commissioning was 0.″10 with a DIMM value

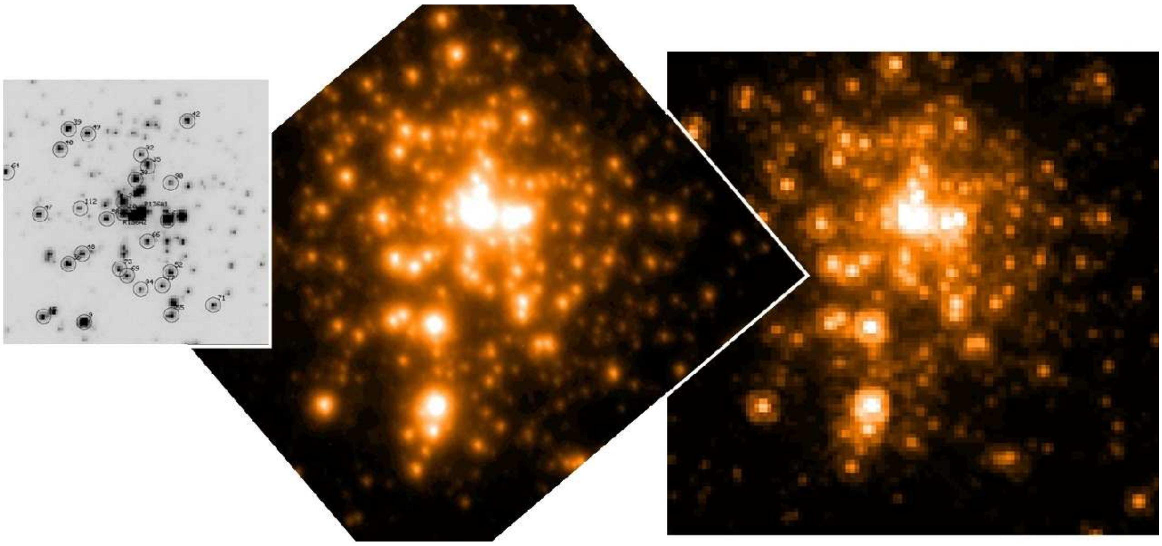

Figure 2.6: Comparison of different images of the core of R136; *left panel*: *HST*-WFPC2 F555W image (Massey & Hunter, 1998); *centre panel*: ∼10"x10" of *H*-band Field 3 MAD image; *right panel*: *HST*-NICMOS F160W image (Andersen et al., 2009)

of 1″.2 (Marchetti et al., 2007), yielding comparable corrections as in our R136 data. Observations taken of the Trapezium cluster obtained similar results, although all the NGSs appeared within, or close to a 1x1’ FoV, i.e, more closely packed than the R136 data (Bouy, 2008).

AO-corrected images have been obtained previously of R136 with the 3.6m ESO telescope using the COME ON+ AO system (Brandl et al., 1996). FWHMs of ∼0″.19 were recorded for the central source peak, but deteriorating as one moves away from the centre, over a 12.8x12″.8 FoV. To really appreciate the excellent image quality produced by MAD, Figure 2.6 shows a comparison with a *HST*-NICMOS image (Andersen et al., 2009). The MAD image provides a more defined central core to the PSF, with a cleaner profile. Note that, by virtue of the larger primary aperture, the resolution is better than *HST* in the near-IR and roughly comparable in the optical (left-hand panel of Figure 2.6.

Strehl Ratios

Aberrations push light into the wings of the profile, reducing the peak intensity. The Strehl ratio is the measure of the peak intensity of the aberrated PSF to that of the diffraction limited case. It is often used as a measure of aberrations present within the optical path, and so used to define the quality of corrections made by an AO system. There is debate over whether the Strehl ratio is the best method of determining the performance of an AO system as it does not define the form of the corrected PSF. Other terms are also beneficial in describing performance, such as the FWHM, which can describe the contrast and angular resolution of an image, and encircled energy, which defines the energy within a given radius and so helps define the PSF profile. Currently, however, the Strehl ratio is still the most common metric used in determining AO performance.

The Strehl ratios across the MAD fields can be seen in Figure 2.7. The maximum Strehl across the FoV for Field 2 in the K_S-band was 28%, the average being approximately 22%. Field 1 was less impressive with 12.5%, but it is relatively uniform across the entire field. Field 3 ranged from 22.5% next to the NGS, down to 5% at the furthest point from the NGSs. The relative positions of the NGSs differ from those used by Bouy (2008) in the Trapezium cluster, but the Strehl ratios of both programmes are comparable. The previous COME ON+ images from Brandl et al. (1996) had a Strehl ratio of 17% in the K_S-band, which they stated to be lower than expected (attributed to aberrations in the optical system). On the whole, similar values have been achieved by MAD, but over a much larger FoV.

2.2.5 Photometry

Photometric fluxes were calculated using standard DAOPHOT routines within IRAF. Parameters were set as follows. The PSF fitting annulus was set at $\sim$3 times the FWHM and the fitting radius to 1-2 pixels larger than the FWHM. Average FWHM and background values were used to find 5σ detections, with any false detections rejected at a later stage. The PHOT program was used to measure the instrumental flux of the de-

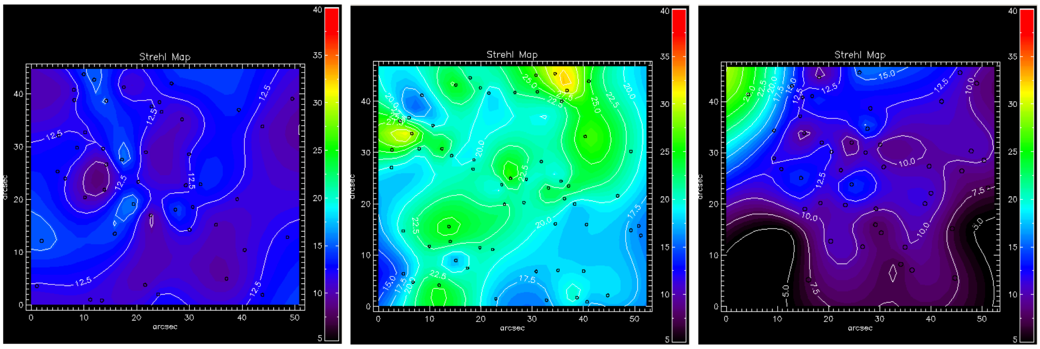

Figure 2.7: K_s-band Strehl (%) maps for Fields 1, 2 and 3 (left to right). East is to the right, north is to the top

tected objects and the PSF routine used to create a model PSF from 20-30 hand-selected stars across the FoV. The stars selected to create the model PSF were bright, but not saturated, isolated (as much as possible) and uniformly spread across the FoV. The model PSF followed a PENNY2 function, essentially a Gaussian core with Lorentzian wings. The nature of the ever changing turbulence and the quality of AO correction (dependent on NGS position, as well as other factors) results in a PSF whose shape is both temporally and spatially dependent. Figures 2.8 shows the PSF of a star change over six consecutive frames, while Figure 2.9 shows how the PSFs of six stars spread across the image vary with position. With this in mind, the model PSF was allowed to vary quadratically across the FoV.

Stars neighbouring on the selected stars were removed through the use of the initial model PSF. This allowed the model PSF to be re-computed from stars without contamination in their wings. Finally, a residual image was created using the ALLSTAR routine to subtract the spatially-varying model PSF from all the detected stars. This process was repeated, varying different parameters and altering the model PSF until the residual image resulted in a uniform subtraction, aiming for just the background and nebulosity remaining.

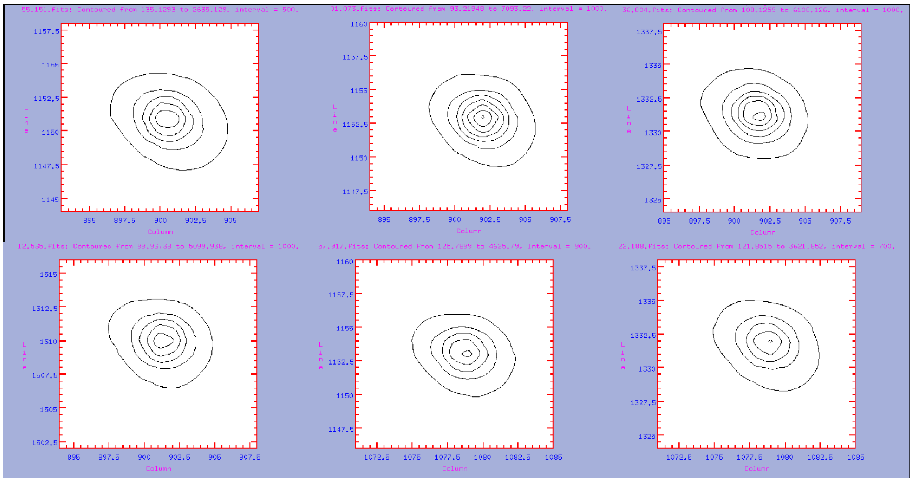

Figure 2.8: The PSF contours of a star in K_s-band Field 1 for six consecutive frames.

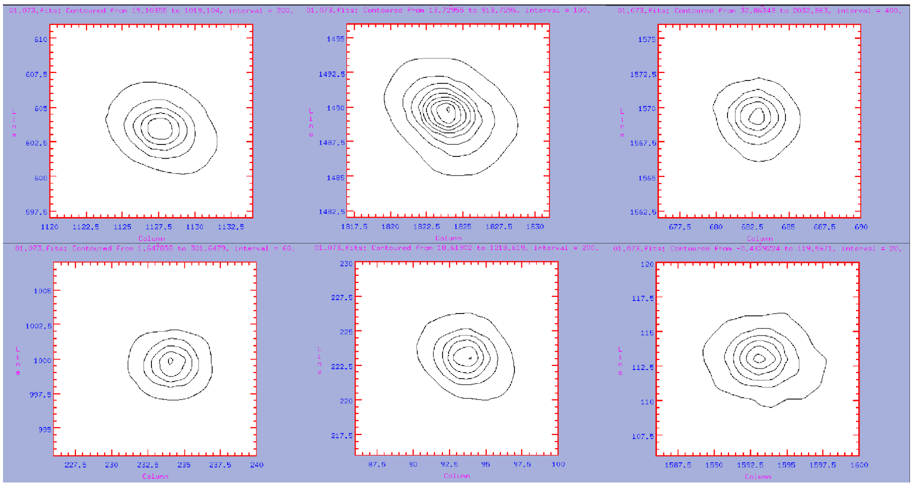

Figure 2.9: The PSF contours of six stars in K_s-band Field 1 spread uniformly across the frame.

Table 2.2: Photometric zero-points obtained from the combined image method. K_S-band results are from using 2MASS sources within the MAD frames , and using the HAWK-I commissioning data (see Section 2.4), in which the result for Field 2 was bootstrapped from stars overlapping with Field 1. The H-band results are obtained using 2MASS sources for Fields 1 and 3, with Field 2 again calibrated using stars overlapping with Field 1.

Band	Calibration	Field 1	Field 2	Field 3
K_S	2MASS	26.78 ± 0.13	26.61 ± 0.45	26.95 ± 0.25
K_S	HAWK-I	26.69 ± 0.08	27.04 ± 0.09	27.07 ± 0.11
H	2MASS	27.09 ± 0.14	27.27 ± 0.15	26.93 ± 0.08

2.2.6 Photometric Calibrations

The catalogues created from the combined frames for each field were initially calibrated from 2MASS sources. However this turned out to be problematic. 2MASS has a pixel size of 2" (Skrutskie et al., 2006), whereas MAD has $0\farcs028$ pixels, two orders of magnitude smaller. The high angular resolution of the MAD data resulted in many of the 2MASS stars within the FoV being resolved into asymmetric or multiple components. With this in mind, only apparently single sources with photometric ratings of ’A’, ’B’, or ’C’ in the relevant band were used for photometric calibration. This severely limited the number of 2MASS calibration sources available per field. Furthermore, to ensure the photometry of calibrating stars was reliable as possible, 2MASS objects fainter than 14.5^{m} were removed (2MASS has signal to noise of 10 down to 14.2^{m} in the K_S-band (Skrutskie et al., 2006)) . Four to eight 2MASS stars were available to compute the Zero Point (ZP) across each field; a summary of the results is in Table 2.2. The resulting ZPs had large uncertainties associated with them, with K_S-band Field 2 having the greatest uncertainty with a value of $\pm 0.45^{\mathrm{m}}$.

The magnitude offsets of stars overlapping between the MAD images were compared to check how well the ZPs for each field agreed. This was only possible between Fields 1 & 2, and 1 & 3, where $\sim$30 overlapping stars were compared. The stars chosen for comparison were hand picked and distributed as evenly as possible across

Table 2.3: Summary of the photometric zero-points obtained from the individual frame method. As in Table 2.2, the K_s-band results are derived from HAWK-I, with the H-band results from 2MASS. In both cases, Field 2 was calibrated using stars overlapping with Field 1.

Band	Field 1	Field 2	Field 3
K_s	23.40 ± 0.07	23.62 ± 0.08	23.59 ± 0.11
H	24.45 ± 0.14	24.37 ± 0.14	24.33 ± 0.08

Table 2.4: Comparison magnitudes of stars overlapping in different MAD fields.

Method	Fields	Δ Instrumental Magnitude	Δ ZP 2MASS Magnitude	Δ ZP Field Magnitude	σ
Combined	K_sF1-K_sF2	0.35	0.17	0.52	0.03
	K_sF1-K_sF3	0.37	−0.17	0.20	0.02
	HF1-HF2	0.17	−0.05	0.12	0.04
	HF1-HF3	−0.16	0.16	0.00	0.02
Individual	K_sF1-K_sF2	0.22	0.31	0.54	0.03
	K_sF1-K_sF3	0.21	0.02	0.24	0.02
	HF1-HF2	−0.08	0.2	0.11	0.03
	HF1-HF3	−0.10	0.12	0.02	0.02
	K_s-band Hawk-I F1-Hawk-I F2	−0.28	−0.18	−0.10	0.02
	K_s-band Hawk-I F1-Hawk-I F3	0.04	0.01	0.03	0.05

the overlap region. Although no hard limits were placed on the range of magnitudes used, extremely bright and extremely faint stars were rejected, along with stars used in the ZP calculations. No other constraints were placed on selection. Instrumental magnitude differences, and 2MASS ZP-corrected magnitude differences were found, as summarised in Table 2.4. If the 2MASS ZPs are accurate then the offset between the instrumental data should correspond to the difference in 2MASS ZPs. Similarly, the offset between the ZP-corrected data should be zero.

The only two fields in good agreement were H-band Fields 1 & 3. All others showed large variations between photometric values obtained, as can be seen in Table 2.4. The standard deviations of the differences between overlapping stars are small, suggesting that the offset from each overlapping star are consistent. The mean offsets between the ZP corrected magnitudes suggests that the 2MASS ZPs are not accurate between fields. The difference in calibrated ZPs could be caused by either inaccurate values from the 2MASS catalogue, or by differences in the star to star photometric values obtained from the MAD data. This is investigated in the next section.

2.2.7 Individual Data

If the PSF of a star varies between different frames (as is likely with AO-corrected imaging, as conditions change from exposure to exposure) the resulting combined PSF may broaden and be noisier. It is also possible that a double-peaked PSF could result. With this in mind, improvements might be made by measuring photometric values through PSF fitting on individual frames. This allows the sky, PSF, and seeing parameters to be tailored for each individual frame. The potential benefit of this method is more precise PSF fitting, leading to improved fidelity of the final photometric catalogue. Working on the individual frames can also reduce the impact of the varying Near-IR sky and take advantage of better seeing values. Furthermore, it allows the user to set the number of frames in which a source must be detected for its inclusion in the final catalogue. This has the big advantage that objects in the dithered regions (previously discarded when the combined image is subset) can now be included, increasing the spatial extent of the final source catalogue. It also leads to fewer object rejections from stars that are affected by cosmic rays or bad pixels in one or a few frames.

The potential downside to this method is a loss in sensitivity compared to the combined image method. To minimise the lower rate of detection due to a loss in sensitivity, the positions of stars in the individual images were found using the 5σ detection results from the pre-cropped, combined image. The relevant spatial shifts between the combined and individual frames were applied and photometric measurements were carried out on the individual frames. The same photometric methods were employed as previously. This involved creating individual model PSFs for each frame, resulting

Table 2.5: Table of MAD photometric zero-point uncertainties for both the individual frame and combined frame methods. Both 2MASS and HAWK-I calibrations are compared.

Calibration	ΔKf1	ΔKf2	ΔKf3	ΔHf1	ΔHf2	ΔHf3
Combined - 2MASS	±0.13	±0.45	±0.25	±0.14	±0.32	±0.08
Individual - 2MASS	±0.14	±0.45	±0.24	±0.14	±0.31	±0.08
Combined - Hawk-I	±0.08	±0.09	±0.11	-	-	-
Individual - Hawk-I	±0.07	±0.08	±0.11	-	-	-

in multiple catalogues for each frame. These were run through Peter Stetson's DAOMATCH and DAOMASTER packages to create a final mean catalogue. The number of frames in which an object must appear to be included in the final catalogue was set to the minimum repetition for each dither pattern (three) enabling the entire region covered by the observations to be included.

2MASS calibrations were undertaken using the same method employed on the combined frames, with the resultant ZP uncertainties found in Table 2.5. Using the individual frames made very little difference on the eventual photometric uncertainties. This points to a conclusion that the photometric uncertainties are dominated by the calibration sources, rather than the photometric measuring techniques.

As a further comparison, the photometric offsets between the combined and individual catalogues for each field were compared (see Figure 2.10). Over a thousand objects were compared in each field, for which no selection restrictions were applied. The mean offset between the two techniques was always less than 0.05^{m}, with the largest standard deviation corresponding to $\pm0.17^{\mathrm{m}}$. That this is much lower than the largest 2MASS derived ZP uncertainty, once again suggesting that the dominant source of ZP uncertainty arises from the sources used for calibration. With this in mind, another source of data to use as a calibrator was required.

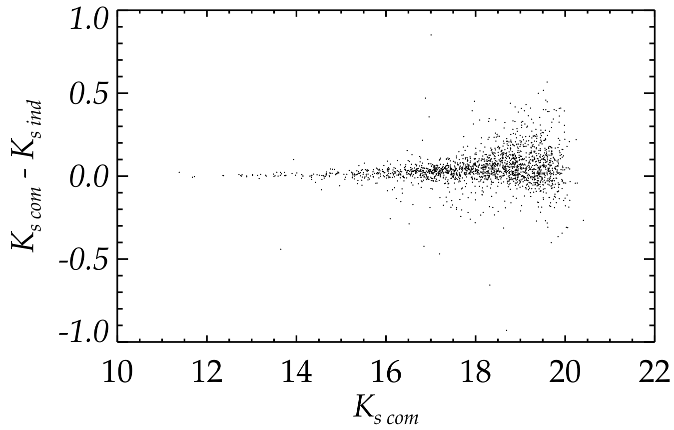

Figure 2.10: Comparison between the MAD photometric catalogues of individual and combined techniques for Kp1 which contained the largest scatter.

2.3 HAWK-I Data

30 Doradus was observed in the K_S, J, Y & $Br\gamma$-bands as part of the High-Acuity, Wide field K-band Imaging (HAWK-I) commissioning observations. HAWK-I is a cryogenic near-IR imager situated at the Nasmyth A focus of UT4 of the VLT in Paranal. The focal plane contains four HAWAII 2 RG arrays covering a $7\rlap{.}'5$ x $7\rlap{.}'5$ FoV with a pixel scale of $0\rlap{.}''106$ (Kissler-Patig, 2008). Currently HAWK-I does not have AO capabilities, although GLAO is planned for the future. The pixel scale is larger than that of MAD, but the FoV covers a much larger area, containing many more 2MASS sources than are available to MAD. It is therefore possible to calibrate the HAWK-I data using many 'AAA' rated 2MASS objects, providing a potentially more reliable ZP calibration. The MAD data can then be bootstrapped off the HAWK-I data, potentially improving the uncertainty associated with the MAD ZPs. Section 2.4 discusses the use of the HAWK-I data for photometric calibration of the MAD data.

The larger HAWK-I FoV also allows a wider analysis of the stellar populations surrounding R136. Further investigation into whether R136 is causing a second generation of star-formation (Walborn & Blades, 1997) on the periphery of R136 is carried out in Chapter 4.

2.3.1 Reduction Method

The HAWK-I data was reduced using the same principles as for the MAD data. A master dark mosaic was created from darks across all four detectors, then subtracted from all object and flat field frames. The frames were then split into their separate detectors. Where the exposure times of the flat fields and darks differed, they were scaled to the same exposure time as the science frames. Master flat fields were created and applied to the sky and science frames.

Bad pixels masks were created for each detector with an `idl` program, using master darks from each individual detector. The IRAF program FIXPIX interpolated across the bad pixels using the four surrounding pixels. This was undertaken on both science and sky frames, removing all bad pixels. The sky frames contained a lot of bright objects and so to remove as much light from the median sky frame as possible, sky masks were created for each individual sky frame. Applying these masks within FIXPIX removed most of the objects within the sky frames. A median sky frame was created using the IMCOMBINE package. Further clipping was employed at this stage to remove any star light not removed by the sky masks. The best results were found using a rejection threshold of 2σ, which is purposely low as the master sky frame should be uniform. Note that readout noise and gain values were set independently for each detector. The median sky frames were then subtracted from the science frames.

Cosmic rays were removed from the science frames using XZAP within XDIMSUM. Conservative sigma clipping values of 20 were used, however some of the frames contained saturated objects and the clipping process resulted in flux being removed from their cores. Accurate photometric values can not be obtained for saturated objects due to the non-linear response of the detector in these regions, therefore cutting flux from these objects was fine.

The optical distortions across each HAWK-I detector is quoted to be very small (Kissler-Patig, 2008), however as distortion maps were available they were applied using the HAWK-I reduction package HAWKI_UTIL_DISTORTION through the ESO Recipe Execution Tool (ESOREX). The science frames were aligned using the IRAF IMALIGN package and combined. The dither pattern of the observations resulted in the edge regions of the combined frames containing differing numbers of overlapping images. These regions were not removed because although photometric values cannot be obtained for sources within them, the objects can still be used for astrometric calibrations.

2.3.2 Photometric Calibration

Photometric values for the K_S HAWK-I data were obtained through PSF fitting subtractions for both the combined and individual data sets (employing 5 σ detections on the combined frames), with the detected objects aligned to the individual frames. The best-fitting PSF model was created using a PENNY2 function which was not allowed to vary across the field. Any distortions within the telescope optical path will cause the PSF to vary across the field. The HAWK-I FoV was found to be fairly uniform without distortion corrections. However, the small distortions that did exist were mapped and removed, and so the PSF should be constant across the image. When creating model PSFs it would have been possible to use a varying PSF across the FoV, however, there are benefits in keeping the model PSF spatially constant. Fixing the PSF model allows more stars to be used to create a final model PSF, whereas allowing the PSF model to vary results in fewer PSF stars being available to create the model in each region. Using fewer PSF stars leaves the model PSF more at the mercy of random anomalies. It could be argued that atmospheric effects would lead to spatially varying PSFs, however, the lower order turbulence, which influences the whole FoV, has the greatest effect on the resulting PSFs. Integration times of two seconds will average out turbulence across the FoV, creating a common PSF. A visual inspection of the HAWK-I residuals indicated that no poor subtractions occurred in any region.

Catalogues were created for the combined frames and for all the individual frames. Peter Stetson's DAOMATCH and DAOMASTER packages were used to create a final

Table 2.6: Summary of the HAWK-I K_S-band photometric ZPs derived from 2MASS sources. Numbers in brackets refers to the number of 2MASS objects used in each calibration.

Method	Field 1 ["]	Field 2 ["]	Field 3 ["]	Field 4 ["]
Combined	27.95 ± 0.07 [29]	27.87 ± 0.11 [18]	28.04 ± 0.11 [25]	27.76 ± 0.04 [13]
Individual	25.42 ± 0.09 [45]	25.25 ± 0.12 [28]	25.49 ± 0.11 [27]	25.18 ± 0.05 [21]

mean catalogue for the individual frames, setting the number of frames that an object must occur in to two, incorporating the repetition of the dither pattern. Selection criteria were set to chi<4 and $-2.5<$sharpness<2.5 to remove spurious detections. The sharpness criteria were relaxed relative to the MAD data due to the large regions of nebulosity in the HAWK-I data.

ZPs were calculated using 2MASS objects with 'AAA' ratings, as indicated in Table 2.6. Between 20 to 45 2MASS sources were used per field in calculating the individual catalogues ZPs, resulting in a uncertainty of $\sim 0.1^{\mathrm{m}}$ for each in K_S-band and $<0.1^{\mathrm{m}}$ in J-band. Similar uncertainties were recorded for the combined catalogues, even though fewer stars were available for the calibration, due to the reduced spatial coverage in the combined fields. The scatter for each ZP calculation can be seen in Figure 2.11. There were no trends with magnitude. To check that the ZPs obtained for the combined and individual catalogues were in agreement, the magnitudes of stars within the Fields were compared (see Figures 2.12 & 2.13). The graphs show the excellent agreement between calibrations, with standard deviations that are much less than the ZP uncertainties.

2.3.3 Photometric Calibration Colour Corrections

The filters used for the 2MASS observations differ from those of HAWK-I. The relative transmission of the filters differs with wavelength, so the ZP calibrations require a colour correction term. The colour term for the HAWK-I data was found by comparing to the 2MASS stars using (J-K_S) colours (see Figure 2.14). Weak colour terms were observed in both J- & K_S-bands. The photometric catalogues were corrected, remov-

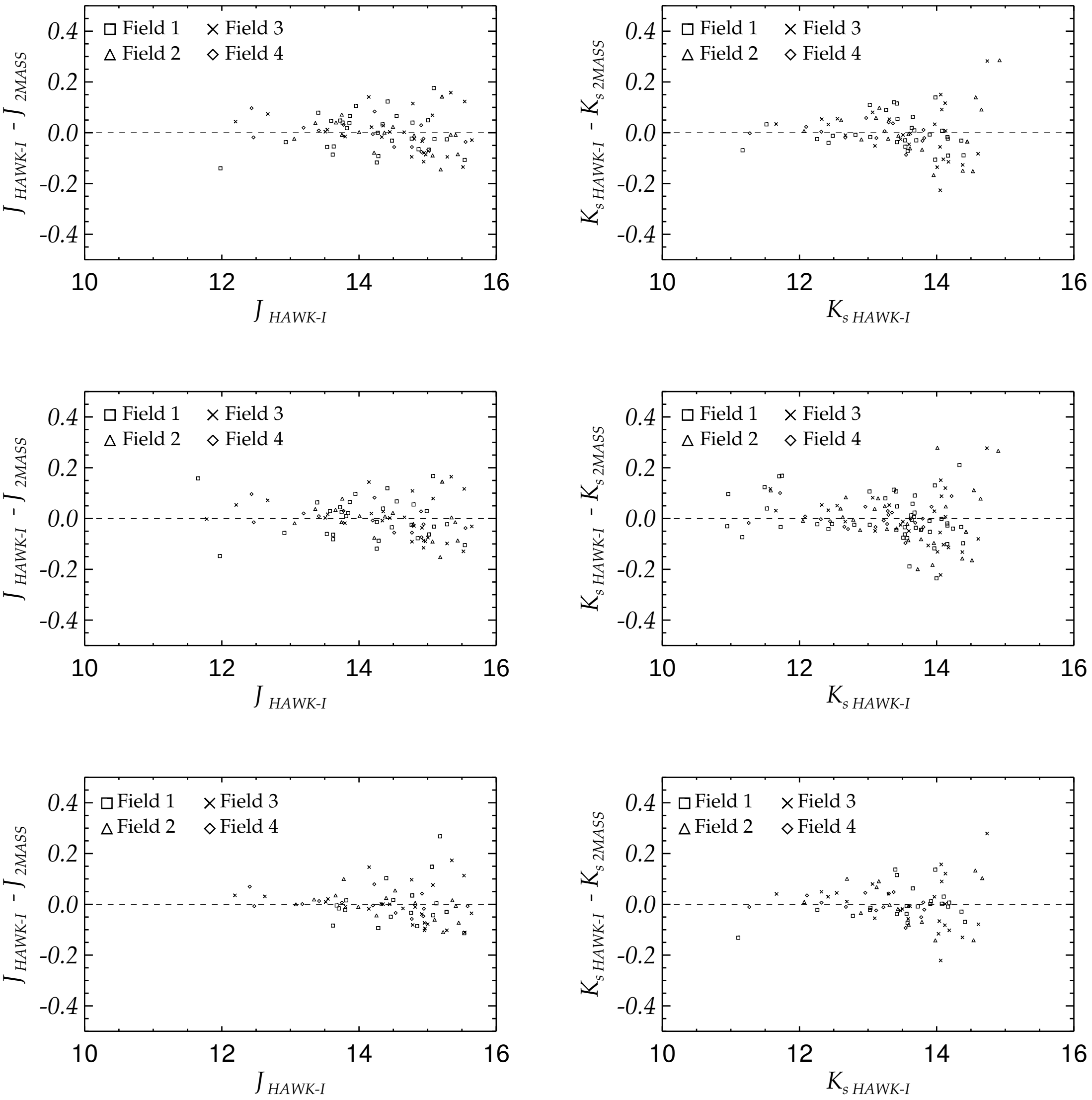

Figure 2.11: Comparison of the HAWK-I photometry compared with the 2MASS values. *Top-left panel*: Combined *J* fields, *top-right panel*: combined K_s fields, *middle-left panel*: Individual *J* fields, *middle-right panel*: individual K_s fields, *bottom-left panel*: Individual *J*-fields with colour corrections applied, *bottom-right panel*: Individual K_s-fields with colour corrections applied.

ing these terms, and the ZPs and standard deviations were re-calculated. In order to completely remove any colour term, this loop was repeated three times.

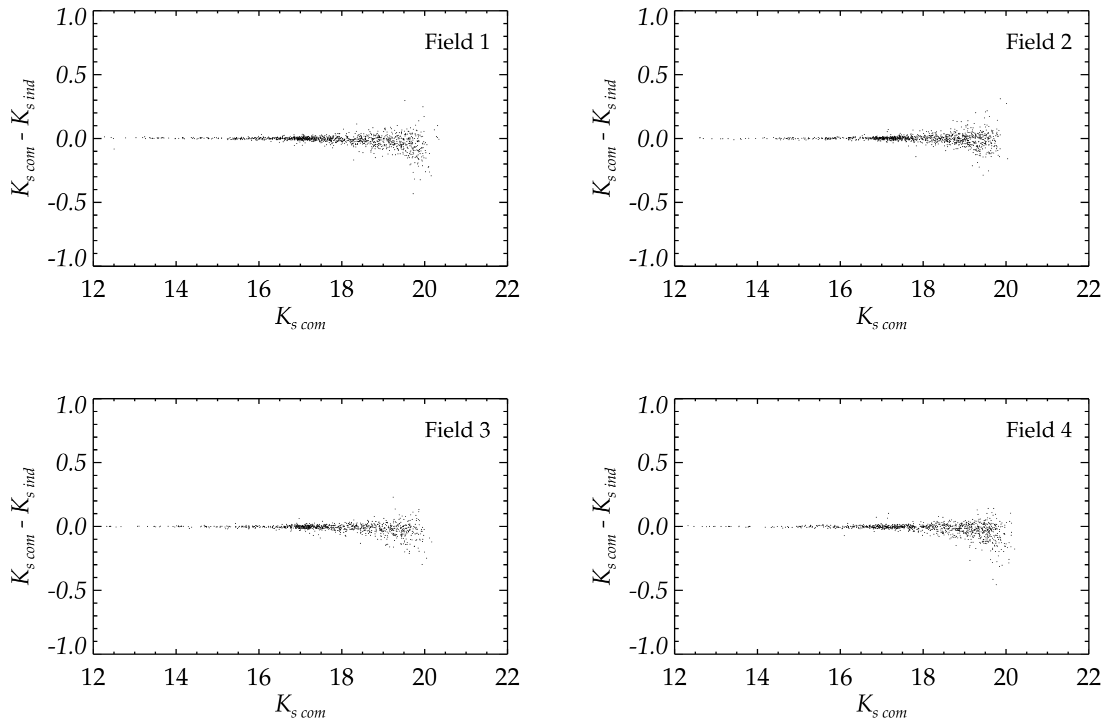

Figure 2.12: Comparison between the HAWK-I photometric catalogues for the individual and combined frame techniques for Kp1.

Recomputing the ZPs from the colour-corrected photometric catalogues, the ZPs were found to differ little from the original values (see Table 2.7). A reduction in the uncertainty was found in the K_S-band, although none was detected in the J-band. The lack of reduction in uncertainty suggests that the colour term is rather weak, and that uncertainty in the 2MASS and HAWK-I photometric values dominate. Figure 2.14 indicates that the colour term introduces an uncertainty of $J = \sim 0.1$ over J-$K_S \sim 3$mag.

The HAWK-I filters were designed to be similar to that of VISTA (Casali, M., private communication, 2010) and the colour terms associated with VISTA and 2MASS have been determined. The K_S-band colour term between VISTA and 2MASS is $+0.010 \times (J - K_S)$, half of that discovered for the HAWK-I - 2MASS system. Without HAWK-I observations in the H-band and no MAD data in the J-band, no colour term can be determined for the MAD observations in either the H or K_S-band. With a lack

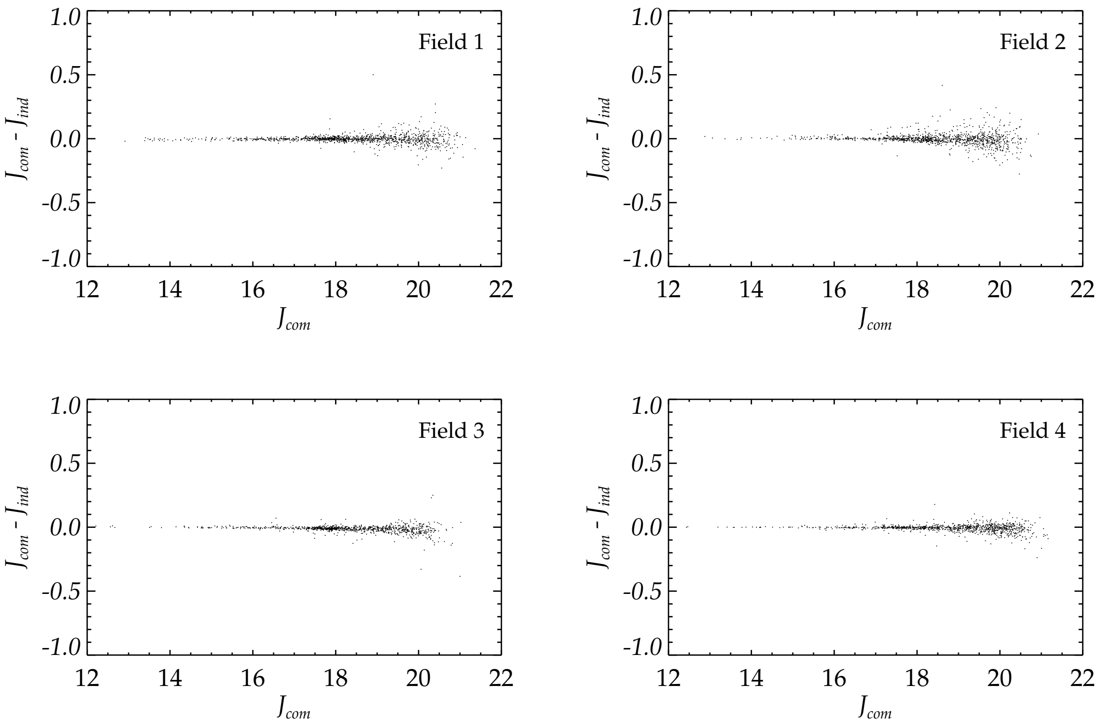

Figure 2.13: Comparison between the HAWK-I photometric catalogues for the individual and combined frame techniques for *J*-band.

Table 2.7: Summary of the HAWK-I colour-corrected photometric ZPs derived from 2MASS sources.

	Field 1 ["]	Field 2 ["]	Field 3 ["]	Field 4 ["]
K_S-band, no colour correction	25.42 ± 0.09	25.25 ± 0.12	25.49 ± 0.11	25.18 ± 0.05
K_S-band, colour correction	25.43 ± 0.06	25.27 ± 0.09	25.49 ± 0.10	25.19 ± 0.04
J-band, no colour correction	26.31 ± 0.08	26.20 ± 0.08	26.41 ± 0.08	26.16 ± 0.05
J-band, colour correction	26.29 ± 0.09	26.21 ± 0.06	26.41 ± 0.08	26.16 ± 0.05

of direct comparison between HAWK-I and 2MASS found in the literature, no colour correction can be applied to the MAD results.

The analysis of the MAD images (see Chapter 3) does not rely on accurate photometric values, so a weak colour term of $<0.2^{\mathrm{m}}$ does not affect the results. Photometric values for YSOs are quoted in Chapter 3, however these are not used for quantitative

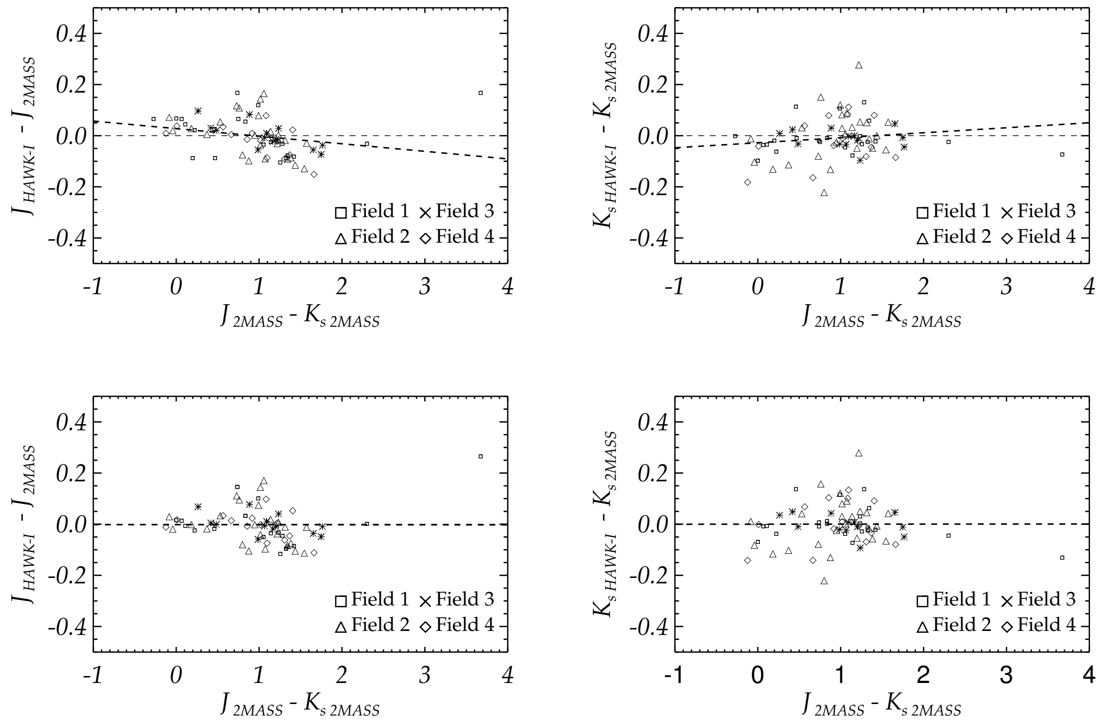

Figure 2.14: Colour trends between HAWK-I and 2MASS filters. *Top-left panel*: J-fields with no correction correction applied, *top-right panel*: K_S fields with no colour correction term applied, *bottom-left panel*: J fields with colour correction term applied , *bottom-right panel*: K_S fields with colour correction terms applied.

analysis, so an uncertainty of $<0.2^\mathrm{m}$ also has little affect. Therefore, the catalogues in the following sections have not had colour corrections applied because, as just stated, this was not possible for the MAD data. However, due to the nature of the analysis, this has little affect on the outcome of the results.

2.3.4 Photometric Completeness

To determine the magnitude level probed by the HAWK-I images, completeness tests were carried out on the combined K_S & J frames. 100 artificial stars between 13-23$^\mathrm{m}$ were distributed randomly across each field, created from the model PSFs generated for each field. Object detection, subtraction and PSF fits were performed for each field,

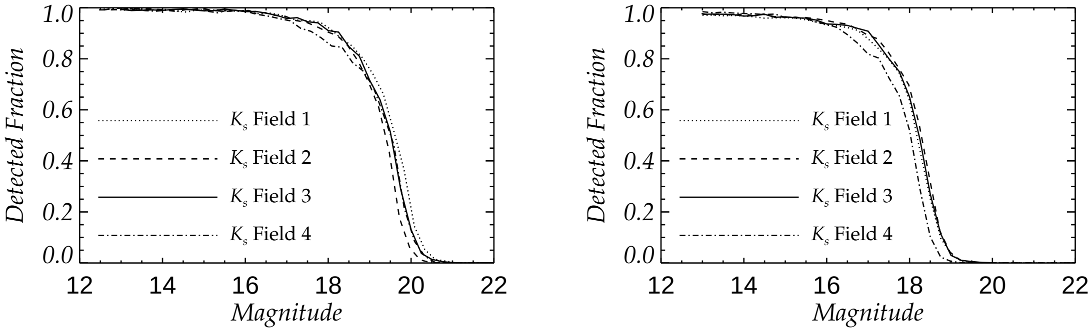

Figure 2.15: HAWK-I K_S-band completeness profiles. *left*: individual frames, *right*: combined frames.

then the ratio of artificial stars recovered to those added was measured as a function of magnitude. This process was repeated 1000 times until 100,000 stars were added to each field. The combined images for each field are 50% complete down to K_S=19.5^m and J=20.75^m as seen in Figures 2.15 and 2.16. Similar magnitudes were reached in the K_S-band as with the MAD data (see Section 2.4.6).

Single K_S frames were used to calibrate the MAD K_S-band data through the 2MASS calibrations as mentioned previously. In order to determine the validity of the calibration, the completeness limits of the single frames were measured. Figure 2.15 illustrates a 50% completeness level of $K_S$$\sim$18.5^m. The magnitude range of stars used to calibrate the MAD data was 14.5-18^m, i.e. above the 50% completeness level for both the MAD and HAWK-I frames, so this approach is justified.

2.3.5 Reddening

There is variable and significant extinction towards R136 with Andersen et al. (2009) finding a median value of $A_v = 1.85^m$ for objects with masses in the range 7-20M$_\odot$. Rieke & Lebofsky (1985) found the relation of interstellar extinction in the V-band to that of the K_S-band, where $A_K/A_v = 0.112$. Therefore, the K_S-band extinction at R136 corresponds to $A_K = 0.21^m$. Indebetouw et al. (2005) found scaling terms to

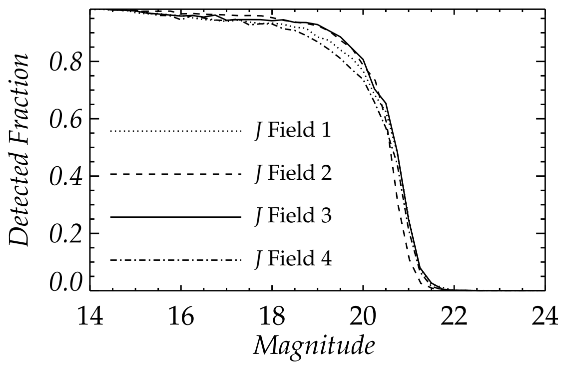

Figure 2.16: HAWK-I J-band completeness profile for the combined frames.

convert between bands, such that $A_J/A_K = 2.50 \pm 0.15$. This corresponds to a J -band extinction of $A_J = 0.52^{\mathrm{m}}$. This yields a near-IR extinction term of $E(J\text{-}K_{\mathrm{s}}) = 0.32^{\mathrm{m}}$, which is larger than the photometric errors.

2.3.6 Colour Magnitude Diagrams

Colour Magnitude Diagrams (CMDs) were created from the J and K_{s} bands (see Figure 2.17). The main sequence is visible , most predominantly in Field 1, which contains the cluster core. To illustrate the range of stellar masses probed by the data, a unreddened $log(t) = 3.0$ isochrone (effectively illustrative of the zero-age main sequence) from Lejeune & Schaerer (2001) is over-plotted in Field 1 of Figure 2.17, adopting a metallicity relevant to the LMC (i.e those from Schaerer et al. (1993) with $Z = 0.008$). The unreddened isochrone is in good agreement with the reddening estimate from Section 2.3.5.

In the redder part of the CMDs, the red clump is visible, centered at (J-K_{s})$\sim$0.75. The red clump is notably dispersed, which cannot be explained solely by photometric uncertainties, pointing to dispersion from differential reddening, with the range in keeping with the values from Section 2.3.5. The slope of the reddening vector (shown in Field 1 in Figure 2.17) is in excellent agreement with the data. The largest dispersion occurs in Field 2 which contains greater nebulosity than the other fields, while Field 3

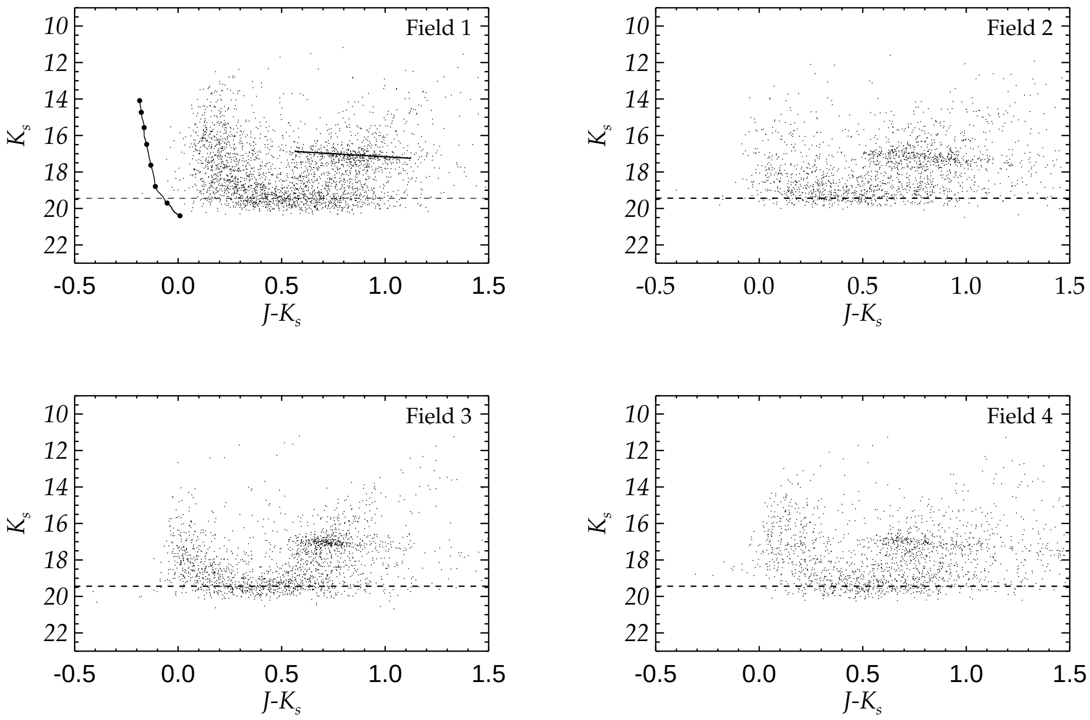

Figure 2.17: CMDs for the HAWK-I fields constructed from individual-frame photometry. Horizontal dashed lines represent the 50% completeness levels from the combined frames. Field 1 contains an estimate of the reddening vector (solid near-horizontal line) and also the youngest isochrone (log t=3.0) from Lejeune & Schaerer (2001), with the marked points indicating, from bright to faint magnitudes, 60, 40, 25, 15, 9, 5, 3, and $2M_\odot$.

contains the least nebulosity and also appears to have the smallest dispersion.

Another contributing factor to the red clump dispersion could be a spread in the age and metallicity of stellar objects. Indeed, a supernova remnant is just-off the bottom right corner of Field 2, suggesting the existence of a population older than R136. Further investigation into the star formation history of 30 Dor will be carried out in the future with aid from the VISTA Magellanic Cloud survey.

2.3.7 Astrometry

The HAWK-I fields were calibrated astrometrically with the same 2MASS objects used for the photometric calibrations, but now also including objects at the edge of the combined frames. Word Co-ordinate Solutions (WCS) were calculated and applied using the CCMAP and CCSETWCS programs in IRAF.

2.4 MAD Calibration - Part II

2.4.1 K_S-band Calibrations

The MAD data was calibrated using only a single HAWK-I frame and so slightly different ZPs were used to those described in Section 2.3.4. This was due to the chronological order that the work was completed. Since the HAWK-I pixel scale is still an order of magnitude better than 2MASS, a visual check was employed to ensure that the 2MASS sources were not multiples or blends in the HAWK-I image. The HAWK-I frames used for calibrating MAD Fields 1 & 3 contained ∼50 'AAA' rated 2MASS sources, while the HAWK-I frame used to calibrate Field 2 contained 28 sources.

To check that the ZPs for HAWK-I data were accurate, a comparison of stars overlapping in the different fields was carried out. The same method was applied as for the intercomparison of the MAD fields, with 30 overlapping stars used between Fields 1 & 3, while only 6 suitable stars could be used for Fields 1 & 2. Fields 1 & 3 were in agreement, while Fields 1 & 2 were offset by 0.10^{m} (see Table 2.4).

HAWK-I ZPs with low standard deviations were found and the MAD data were bootstrapped off them accordingly. Again ∼30 stars overlapping between the MAD - HAWK-I fields were used, being careful that the selected stars were neither saturated, nor below the 50% completeness level for each data set. The new MAD ZPs were within the uncertainty margins of the 2MASS calibrated MAD ZPs, but now with much reduced uncertainties. The greatest reduction was seen in Field 2, where the uncertainty reduced from $\pm0.45^{\mathrm{m}}$ to $\pm0.09^{\mathrm{m}}$. A comparison of using the HAWK-I

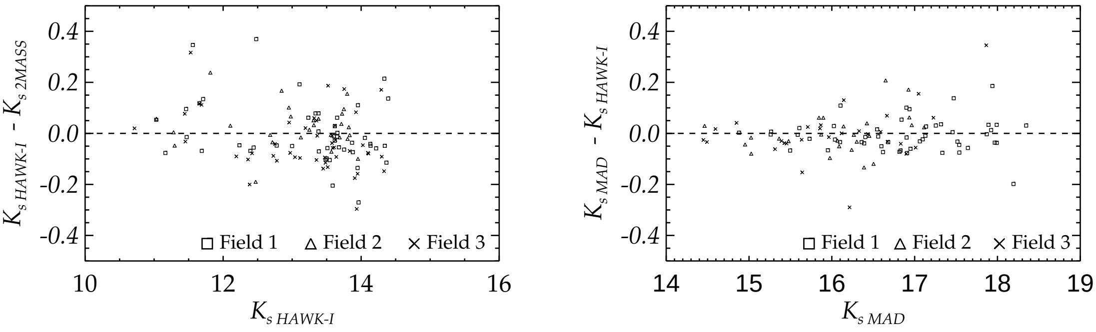

Figure 2.18: *left panel*: Comparison of the HAWK-I K_S-band photometry compared with the 2MASS values; *right panel*: comparison of the MAD K_S-band photometry from the individual frame method compared with the HAWK-I values (calibrated using 2MASS). Field 1: open squares; Field 2: open triangles; Field 3: crosses.

data relative to calibrating directly using the 2MASS data is given in Table 2.2.

Internal agreement between the calibrated MAD images was checked. The mean offset in instrumental magnitudes between Fields 1 & 3 corresponded to the offset between the respective ZPs, giving further confidence in each ZP. There was an offset of 0.1^{m} between Fields 1 & 2, in order to obtain photometric agreement between the 3 fields, Field 2 was corrected by the difference from Field 1.

A comparison between the HAWK-I and 2MASS magnitudes is shown in Figure 2.18, with dispersions of $\pm 0.12\ ^{\mathrm{m}}$, 0.16^{m} and 0.21^{m} for Fields 1, 2 and 3, respectively. The right-hand panel of Figure 2.18 shows a similar comparison between matched objects in the MAD and HAWK-I frames, with the dispersions around the mean quoted in Table 2.3.

2.4.2 H-band Calibrations

Unfortunately, HAWK-I data was not available in the H-band and so another approach was required for the MAD H-band data. The ZP uncertainties from the 2MASS calibration were lower in the H-band than in K_S. From overlapping stars in each field it became apparent that the offsets in ZPs for Field 1 & 3 were in good agreement, giving confidence that the ZPs were correct. Once again there was a difference between Field 1 & 2 and the offset (determined by overlapping stars) was used to correct the ZP of Field 2 relative to Field 1.

2.4.3 Reddening

Using the Indebetouw et al. (2005) relations as before (i.e. $A_H/A_K = 1.55 \pm 0.08$), and adopting the estimate of $A_H = 0.21^{\mathrm{m}}$ (see Section 2.3.5), this corresponds to a H-band extinction of $A_H = 0.32^{\mathrm{m}}$, yielding a relatively small extinction term of $E(H\text{-}K_{\mathrm{s}}) = 0.11^{\mathrm{m}}$. Thus, the H-K_{s} colours from MAD will, in general, not be differentially reddened by much more than the photometric errors.

2.4.4 Colour Magnitude Diagrams

CMDs were created for the three fields (see Figure 2.19). Objects within a $2''.8$ radius of the core, where crowding/blending effects dominate, were removed. The locations of the main sequence are in good agreement, suggesting that the adopted ZPs are consistent.

As for the HAWK-I CMDs, the unreddened, $log(t) = 3.0$ isochrone (illustrative of the zero-age main sequence) from Lejeune & Schaerer (2001) is over-plotted in the *top right-panel* of Figure 2.19 in agreement with the reddening estimate from Section 2.4.3.

To compare the advantages of both photometric techniques, Figure 2.19 shows CMDs created from both methods. As previously mentioned, one of the benefits of employing the individual technique is that the dithered regions can be included in the final catalogue. Table 2.8 lists the number of objects included in each CMD. To ensure a fair comparison between methods, the number of objects detected over the same spatial extent was also compared. This is referred to as 'Individual (Combined Area)' in Table 2.8.

The CMDs created from combined frames result in slightly fainter magnitude limits to those of the individual CMDs. From inspection, the individual method appears to produce a tighter main sequence, which becomes more obvious when CMDs over the same spatial extent are compared. This is due to a reduction in the random star-to-star uncertainties, improved by better fitting parameters when using the individual method.

There are more stars detected using the combined method when compared over the same area range in Fields 2 & 3, as indicated by Table 2.8. The extra detections come mainly from fainter magnitude objects. Although the objects in the individual catalogues were detected in the combined frames, the lower the signal-to-noise for the object, the worse the fitting process and so the more likely the object will be rejected. In Field 1, where the light leak was significant, more objects were detected in the individual (combined area) frame. The dither pattern causes the effect of the light leak to be variable on an object across the frames. By considering the individual frames, the resulting PSF of a particular object would be ’cleaner’ in some frames than in others. Since a star only has to occur in a few frames to be accepted into the final catalogue for the individual method, the probability of it being accepted into the final catalogue is high. The PSF resulting from the stacked frames however, is likely to become warped in the co-adding process and so is less likely to survive the rejection process and not make the final catalogue.

Many more objects are detected in the individual frames when comparing the two techniques over their entire spatial regions. There are overall gains of ∼600-1000 objects through using the individual frames from the spatially larger regions. This is clearly a compelling benefit of using the individual technique.

The number of stars gained using the individual frames, along with a tightening of the CMD over the same spatial extent as the combined frames would suggest that the individual frame measurements provide better catalogues for our purposes.

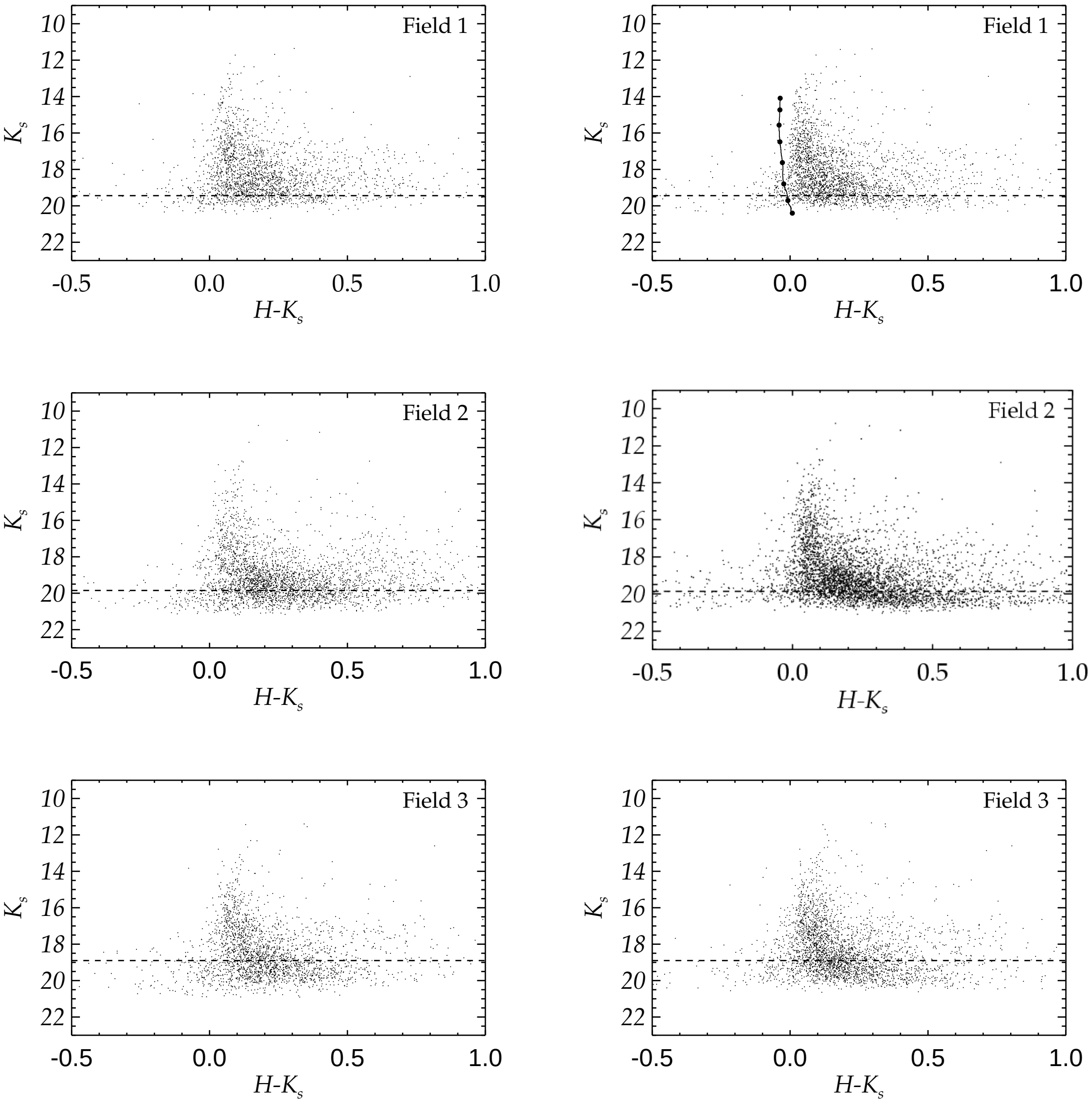

Figure 2.19: CMDs for the combined (*left panel*) and individual frame methods (*right panel*). Horizontal dashed lines represent the 50% completeness levels from the combined frames method. Field 1 for the combined frames also contains the youngest isochrone (log t=3.0) from Lejeune & Schaerer (2001), with the marked points indicating, from bright to faint magnitudes, 60, 40, 25, 15, 9, 5, 3, and 2M_*odot*.

Table 2.8: The number of objects included in the colour-magnitude diagrams in Figure 2.19. *Individual (Combined Area)* refers to the number of objects in the individual CMD covering the same area as the combined frame.

Method	Field 1	Field 2	Field 3
Combined	2164	3175	2346
Individual (Combined Area)	2330	3144	2274
Individual	2750	4134	3033

2.4.5 Astrometry

Astrometric calibration of each field was carried out using catalogues from Selman et al. (1998), recently re-calibrated by Brian Skiff[1]. These positions are dependent on the precision of the 2MASS/UCAC2 positions used to calibrate the data, combined with the plate-scale/seeing of the original New Technology Telescope (NTT) observations. The quoted precision on the new Skiff astrometry is $\sim0\overset{\prime\prime}{.}1$ (cf. the $0\overset{\prime\prime}{.}028$/pixel delivered by MAD). Visual matches of stars between the Skiff catalogue and the MAD fields were used to define ~40 well-distributed astrometric standards in Fields 1 and 2. The astrometric calibration of Field 3, in which there are greater PSF variations, was achieved using 60 visually-matched stars. WCS were calculated and applied using the CCMAP and CCSETWCS programs in IRAF.

2.4.6 Photometric Completeness

Combined Frames

Completeness tests were undertaken in both bands for all three fields. Using the STARLIST and ADDSTAR routines in IRAF, 100 artificial stars with magnitudes ranging from 14^{m} to 24^{m} were distributed uniformly across each combined (and subset) image. As before, PSF-fitting was performed, using the same settings and a PENNY2 model PSF which is allowed to vary across the field. Using the known positions of the added

---

[1] http://cdsarc.u-strasbg.fr/viz-bin/Cat?J/A+A/341/9

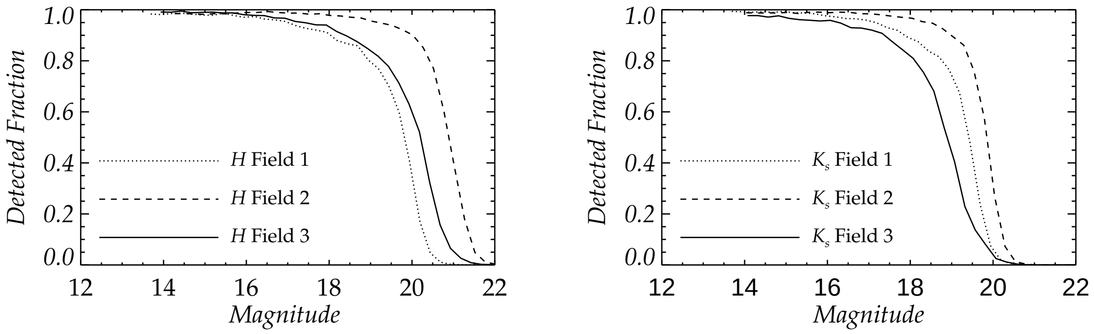

Figure 2.20: MAD H (*left panel*) and K_s (*right*) completeness profiles.

stars, the number recovered from the images within a two-pixel search radius was found. If more than one object was found within that small radius, the object with the smallest magnitude difference was considered the artificial star. Stars with magnitude differences of greater than $\pm 0.5^{\rm m}$ were cut from the detected list, with the intention of excluding mistaken matches, or artificial stars which have been superimposed on genuine stars within the image (thus increasing its magnitude).

Tests were repeated 1,000 times, until 100,000 artificial stars had been added to each image. This gives a ratio of $\sim$30 to 50 artificial stars for each observed object. The ratio of artificial stars detected to those introduced was measured for each image, as a function of magnitude. The stars were split into bins of $0.25^{\rm m}$, with the resulting completeness graphs shown in Figure 2.20. Field 2, which does not include R136 in the combined image, has a slightly more uniform completeness at brighter magnitudes while going slightly deeper. The H-band data is similar, going a magnitude deeper to a 50% completeness of at least $H\sim20$.

Individual Frames

Completeness tests on the individual frames were not undertaken because the objects obtained in the individual catalogues are found within the combined frames, and the completeness tests would not give a fair reflection of the magnitudes reached. Through the comparison of the CMDs the completeness terms should be comparable, although as previously mentioned the combined frames appear to delve slightly fainter.

Chapter 3

MAD Interpretation of R136

In this chapter the MAD observations and photometric catalogues are used for scientific analysis of R136. Surface brightness profiles and azimuthal density distributions are studied to investigate the likely evolution of the cluster and to understand the processes of formation. Before this, a brief introduction to the formation and evolution of stellar clusters is given.

3.1 Stellar Clusters

Star clusters are created from the gravitational collapse of Giant Molecular Clouds (GMCs). It is thought that star clusters are the site of the majority of star formation (Lada & Lada, 2003) with $\sim$95% of clusters dispersed after 100Myr, littering the host galaxy with field stars. A range of astronomical questions can be investigated through the study of stellar clusters, from the process of star formation and evolution, to the star formation histories and evolution of the host galaxies themselves.

3.1.1 Star Cluster Formation and Evolution

Lada & Lada (2003) found that $\sim$90% of the stars that form in embedded clusters are formed in rich clusters (with $\geq$ 100 members having masses in excess of $50\mathrm{M}_\odot$). With this in mind, the basic theory of massive star formation is a useful starting point in understanding how stellar clusters form and evolve (as described by Zinnecker & Yorke (2007)).

Dense molecular cores or filaments form through fragmentation of GMCs, producing locally compressed pockets of gas. Gravitation takes over as the cores begin to collapse, accreting material in the local vicinity of the protostellar object, thus gaining mass. For low mass stars it is believed that pre-main sequence objects run out of nearby material and contract - hydrogen burning commences and the star joins the main sequence. For massive stars, the objects are still believed to be accreting material when hydrogen burning is initiated. How material continues to accrete without being blown away from stellar winds and radiation pressure is still not fully understood. The first views of massive stars are currently being achieved with interferometer and AO-corrected observations (Davies et al., 2010; Kraus et al., 2010), but how even more massive ($>$20$M_\odot$) stars form, along with the large number of binaries, is still unknown.

A possible mechanism for the continual growth of massive stars is through competitive accretion. If stars form in a cluster and there is a large reservoir of gas near by, the gravitational force of the cluster of stars will funnel the gas towards the proto-stellar cores at the centre. This mechanism provides the continual inflow of gas required to create massive stars, however, it does not explain how the material continues to accrete after hydrogen burning has commenced. It could be that there is an upper mass limit possible through accretion and that the most massive stars are formed through collisions. In fact, Zinnecker & Yorke (2007) state that in massive protoglobular cluster clouds, as R136 is believed to be, the gas densities involved might be so large that the formation of massive stars through collisions is ineviable.

Stars disrupt and remove the cloud enshrouding them, while massive stars also help to remove gas within the rest of the cluster, through a combination of stellar winds, UV radiation and eventually (after $\sim$3Myr for the most massive stars), via supernovae. The most common result after gas removal will be an open OB cluster or association (Zinnecker & Yorke, 2007) (discussed in more detail in the next section). Various regions of the GMC can undergo different stages of star formation concurrently as one region triggers star formation within another. The timescales for "triggered" star formation are of order Myrs, so one would expect that as all the stars are formed from the same parent cluster, they will exhibit similar chemical compositions/metallicities.

Once the mass and chemical composition of a star is known, its evolutionary history and future can be constrained (unless in a complex astrophysical system, such as a binary or very dense cluster). Salpeter (1955) introduced the concept of the Initial Mass Function (IMF) of a cluster, relating the number of stars of a particular mass created within a cluster to the the size of the cluster. By tracing the evolutionary track of stars in clusters back to their formation, it should be possible to determine the relative ratios of initial star masses. There is an added difficulty that for clusters older than a few Myr, the highest mass stars will have disappeared due to their short lifetimes.

It is thought that disruption causes most clusters to become unbound, with only 4-7% of embedded clusters found to survive the emergence from molecular clouds to become bound clusters after $\sim$100Myr (Lada & Lada, 2003). Bastian & Gieles (2008) discuss three phases of stellar disruption and the timescales over which they occur.

- The removal of remaining gas by the massive stars, occurring on timescales of $\sim$10Myr.
- Mass loss through stellar evolution particularly from the fast living massive stars, occurring on timescales of $\sim$100Myr.
- Dynamical interactions or tidal relaxation which occurs on timescales of $\sim$ 1Gyr.

Throughout all these stages external tidal forces from the galaxy that the cluster resides in, also influence the cluster.

Primordial Gas Expulsion

Primordial gas expulsion dominates over the period described by massive star formation. Complex processes of gas dynamics, stellar dynamics, stellar evolution, and radiative transfer (which are not completely understood) occur during this phase (see

Elmegreen (2007), Price & Bate (2009)). The removal of the gas will disrupt the cluster. If the cluster is considered to be in virial equilibrium before the gas is removed, the cluster will end in a super-virial state afterwards; the rate of the gas removal will largely determine whether the cluster will remain bound. For many clusters gas expulsion will occur over short time-scales (Portegies Zwart et al., 2010), referred to as Rapid Gas Expulsion (RGE) by Bastian & Goodwin (2006). As mentioned in Section 1.3.1, RGE has been suggested as a likely cause of the excess light observed by Mackey & Gilmore (2003) in the profile of R136.

Hills (1980) investigated the process by considering the mass loss using the virial equation. For a cluster in virial equilibrium, $2T_0 + W_0 = 0$, where T_0 is the kinetic energy and W_0 is the potential energy. Rearranging these terms finds the velocity dispersion prior to mass loss:

$$\left\langle V_0^2 \right\rangle = \frac{GM_0}{2R_0}, \tag{3.1}$$

where M_0 is the total mass of the cluster, R_0 is the effective radius of the cluster and $\left\langle V_0^2 \right\rangle$ is the velocity dispersion. If all the stars in the cluster were of the same mass, then R_0 is the mean harmonic distance between each pair of stars (Hills, 1980). A cluster will establish dynamical equilibrium after the dynamical timescale, τ_{dyn}. In practice this is the time it takes for a typical star to cross the cluster. If the gas is removed in a time quicker than τ_{dyn}, then the gas will not have time to affect the velocities of the stars. In the extreme case, the velocity dispersion before the gas removal will be the same as after.

The energy in the cluster is the sum of the kinetic and potential energies and can be defined after mass loss as:

$$E = T + W = \frac{1}{2}\left[M\left\langle V_0^2 \right\rangle - \left(\frac{GM^2}{R_0}\right)\right], \tag{3.2}$$

where $\Delta M = (M_0 - M)$, and M is the mass remaining in the cluster. The cluster will expand on the dynamical time scale to the new radius in order to restore equilibrium. When virial equilibrium is reached, the energy of the system is related to the potential as:

$$E = \frac{W}{2} = \frac{-GM^2}{4R_{vir}}. \tag{3.3}$$

Re-arranging Equations 3.1, 3.2, and 3.3, the new virial radius can be found in terms of mass loss, where $f_e \equiv \frac{M}{M_0}$ (Hills, 1980):

$$\frac{R_{vir}}{R_o} = \frac{f_e}{2f_e - 1}. \tag{3.4}$$

If the cluster star formation efficiency is high so that less than half the mass of the cluster is lost, then the cluster might survive RGE. If, however, the formation efficiency is low, the new virial radius extends to infinity and the cluster becomes unbound. Furthermore, as the cluster is expanding it is likely that stars on the outskirts will evaporate out of the cluster, further reducing the cluster mass.

Although the example given is a rather simplistic scenario, it does highlight the potentially disruptive power of RGE. Zinnecker & Yorke (2007) point out that low star formation efficiencies could explain the small fraction of old, bound clusters observed.

Observational Considerations

A study by Bastian & Goodwin (2006) investigated what observational effects RGE would have on a cluster luminosity profile. They studied three cluster profiles that deviated significantly from standard parameterisations; M82-F, NGC1569-A, and NGC1705-1 were all found to exhibit excess light at large radii. Bastian & Goodwin suggest that the halos were caused by violent relaxation. As the cluster tries to regain equilibrium, many stars could become unbound - as the stars have finite velocities, the process of ejection could take up to 40Myr and so they will still form part of the luminosity profile, creating observable excess light at large radii. Bastian & Goodwin (2006) calculated N-body models of RGE to see the influence on luminosity profiles, finding an excess in luminosity at large radii, in the simulations.

The radial surface brightness profile for R136 from Mackey & Gilmore (2003) exhibits a “bump” at $\sim$10" (see Section 1.3). If the excess light is caused by RGE, the "bump" should be wavelength independent and so observable in the N-IR. To investigate these results, surface brightness profiles constructed from the MAD observations have been used to investigate whether RGE is the cause of the excess light observed in the optical. If the cluster were going through a state of RGE, it is likely that the strains of such mass loss will result in the cluster becoming unbound in the future.

Stellar Mass Loss

If the cluster remains bound after primordial gas expulsion ($\sim$10Myr), mass loss through stellar evolution becomes the dominant force of disruption. The quantity of mass lost is dependent on the IMF, as stars of different masses expel material over different evolutionary time periods. Massive stars ($\geq 50M_{\odot}$) lose 90% of their mass after going supernova in $\leq$ 4Myr, whereas a $5M_{\odot}$ star loses 80% of its mass before becoming a white dwarf, around 100Myr after joining the main sequence, (Zinnecker & Yorke, 2007). This results in 30% of the cluster mass being lost from a bound cluster within 1Gyr (Baumgardt & Makino, 2003; Baumgardt, 2006), causing the cluster to expand and reducing the cluster tidal radius. As this occurs over large timescales the effect is not as disruptive as primordial gas expulsion, although Baumgardt (2006) found that, combined with an external tidal field, it is enough to unbind low-concentration clusters. Varying the IMF would also alter the disruptive effects. For example, a top heavy IMF (with more massive stars in the cluster) would result in a greater loss over a shorter period, and so will suffer greater disruption. The situation becomes further complicated if the cluster is mass segregated. Under this scenario, most mass will be lost from the core where the massive stars reside, while less massive stars stay relatively unchanged around the periphery due to slower stellar evolution. This will cause an expansion of the inner core, with there being little effect further from the core.

Zinnecker & Yorke (2007) conclude that this phase of cluster evolution results in the expansion of the cluster core, with a slight increase in overall cluster size. After this phase, the cluster will either become completely unbound, or the core will contract under the influence of stellar dynamics.

Tidal Relaxation

The third phase of star cluster evolution is dominated by dynamical interactions between stars. The relaxation time, τ_{rl}, is the time required for the velocity distribution of the cluster members to become Maxwellian, in which case a fraction of the stars will have velocities greater than the escape velocity of the cluster. The mass from stars escaping the cluster in this manner is called evaporation. After another τ_{rl} the Maxwellian distribution will again be reached, and more stars will evaporate.

With time, mass segregation will occur in the cluster core through equipartition of energy. The massive stars will transfer kinetic energy to the less massive stars through weak, long-distance encounters. In the process, the massive stars lose kinetic energy, gaining potential energy and sinking to the cluster centre. As the core contracts, close dynamical interactions will become more frequent and stars will be ejected, further removing energy.

Evaporation and ejections will cause the core of the cluster to collapse and heat up. Left to is own devices, the core will contract to infinite density as it reaches zero radius, referred to as core collapse. The rate of this process is slowed down through the interactions, formations, and destruction of binary systems.

3.2 Star Cluster Profiles

The radial profile of YMCs can provide information about the progenitors to the cluster and some of the parameters affecting the formation process. If the age is less than the crossing time then it can be assumed that any cluster structure observed is largely determined by the formation process and not through dynamical interactions. The structure of the cluster can then be generalised to be similar to that of the original molecular cloud.

Bonnor (1956) & Ebert (1955) investigated the process of star formation through the collapse of molecular clouds. They treat the clouds as isothermal, following perfect gas laws. Truncated at an outer radius by pressure, the clouds are otherwise in hydrostatic equalibrium. A cloud with these initial conditions is referred to as a Bonnor-Ebert (BE) sphere. By applying Boyle's law, with a correction term as suggested by Terletsky (1952) to account for the cloud mass distribution, the cloud can become gravitationally unstable in a similar mannar to the Jeans instability. If the critical mass is reached, self-gravitational collapse occurs. As the inner core has no pressure support, the central core goes into free-fall, resulting in a increase in the central core density. This causes a reduction in the density in the outer regions. As pressure gradients are formed, free-fall is restricted.

The cloud has a radial profile following r^{-2} after collapse, while still truncated at large radii. If the stellar formation time is less than the collapse time, then the stars will form from a fragmenting, collapsing cloud before a singularity occurs at the cluster core. This will result in a constant density, ρ_0, in the cluster core. The radial extent of this constant density is dependent on the collapse timescale.

This description of cloud collapse follows the so called classical dynamical theory (Mac Low & Klessen, 2004) focusing on the dominance of self-gravity and pressure gradients, with turbulence having little affect of the cluster formation. Smoothed Particle Hydrodynamics (SPH) numerical simulations of molecular clouds (Ballesteros-Paredes et al., 2003) suggest that turbulence does have an important role to play. On global scales, turbulence can counterbalence gravity. However, locally, supersonic turbulence provokes collapse and hence star formation (Mac Low & Klessen, 2004). If the frequency between turbulent shocks is long enough, self-gravitational collapse can dominate and incite star formation. In fact, the efficiency with which star formation occurs is dependent on the strength and scale of turbulence. The more energy injected into a system through turbulence, the greater support there is, resisting collapse and so making star formation less efficient.

Whilst not all molecular clouds are thought to be isothermal, BE spheres have been discovered in nature, such as the Bok globule, Barnard 68 (Alves et al. (2001), Lada et al. (2007)). Recent SPH simulations treat molecular clouds as polytropic in nature, changing as a function of density. Recent simulations by Bate et al. (2003) & Bate

(2010) use the following conditions:

$$p = K\rho^{\eta} \tag{3.5}$$

where,

$$\eta = \begin{Bmatrix} 1, & \rho \leq 10^{-13} gcm^{-3} \\ 7/5 & \rho > 10^{-13} gcm^{-3} \end{Bmatrix} \tag{3.6}$$

where p is pressure and K is a measure of the entropy of the gas. As previously mentioned, for extremely young clusters, the structure of the stellar cluster is likely to be reminiscent of the molecule cloud it formed from. If the cluster has a profile of $\rho \propto r^{-2}$ (with γ=1, see Equations 3.7 & 3.8), then the original cloud could very well have been a BE sphere.

The structure of the cluster will be affected by the efficiency of the star-formation process and its time-scale. The formation efficiency is defined as the ratio of the original mass of the gas cloud that is converted into stellar mass. The formation phase is considered complete when all the gas has been converted into stellar objects or expelled from the cluster region. The formation time is considered fast if it is complete within a cluster crossing time and slow if longer. A fast formation time is difficult to envisage as it requires the formation process to be synchronized across the protocluster and so not instigated by other regions of formation. Previous observations of young stellar clusters in the LMC detect nebular emission from clusters with ages 10Myr, which exhibit crossing times of $\sim$ 1 - 10Myr. As the gas has not been removed within the crossing times, this indicates slow formation timescales are likely, but it does not however, rule out the possibility that fast formation times can also occur.

If the star-formation efficiency is low, but the formation timescale is fast, the cluster could not remain bound. The cluster would loose over 50% of its initial mass before the crossing time and so would dissipate (Elmegreen, 1983; Lada et al., 1984), although this could take a long time to occur (Takahashi & Portegies Zwart, 2000). As previously stated, the efficiency of star formation is reliant of the injection of energy to the system through turbulence, hence effecting the probability of the cluster remaining bound.

If the efficiency is high with a fast formation timescale, little energy is lost from the system and the cluster can be considered to have formed non-dissipatively. N-Body simulations of dissipationless collapse find profiles with $1.5 < \gamma < 2$ (McGlynn, 1984). The initial kinetic energy of the system was also found to influence the profile of the cluster. Cold initial conditions (i.e., zero kinetic energy) were found to produce small cluster cores, with larger cores and steeper slopes as the temperatures were increased. In contrast, the distribution or "clumpiness" of the original cloud had little effect on the end profile.

A study of extra-galactic clusters found evidence that younger clusters have shallower profiles (with γ increasing) with age (Larsen, 2004). It is thought that the increasing core and reduction in central density is caused by mass loss through stellar evolution and evaporation as the cluster age reaches the relaxation time (Takahashi & Portegies Zwart, 2000).

3.2.1 Fitting Cluster Profiles

Elson et al. (1987) studied the surface brightness profiles of young stellar clusters in the LMC and found they had cores of constant density out to a radius of a, then exhibit power-laws at large radii. The surface brightness profiles were described by mathematical fits, referred to as EFF profiles:

$$\mu(r) = \mu_0 \left(1 + \frac{r^2}{a^2}\right)^{-\frac{\gamma}{2}}, \tag{3.7}$$

where μ_0 is the surface brightness at r=0, a is the scale radius, and γ determines the power-law slope. The fits are for 2D observations. The 3-dimensional density profile has a logarithmic slope of (Portegies Zwart et al., 2010):

$$-\gamma_{3D} = -(\gamma + 1). \tag{3.8}$$

King (1962) investigated the surface brightness (μ) profiles of Globular Clusters (GC) and found the profiles drop-off at large radii. He found the GCs follow an empirically derived profile of:

$$\mu(r) = \mu_1 \left(\frac{1}{r} - \frac{1}{r_0} \right)^2, \tag{3.9}$$

where μ_1 is a constant and r_0 is the radius where μ reaches zero. Equation 3.9 is refereed to as the King model and fits the distribution of globular clusters well at large radii. Mackey & Gilmore (2003) found that the outer region of R136 in the optical was well fit by a King profile, suggesting that R136 might have more in common with GCs than other YMCs in the LMC.

3.3 MAD Radial Profiles

To gain an accurate radial profile that spans the core centre to the outer regions of the MAD data, a combination of star counts and integrated light measurements are required. The radial surface brightness methods and analysis for R136 are now discussed.

3.3.1 Integrated Light Measurements

Integrated-light radial profiles were calculated using a specifically written `idl` program and also using standard DAOPHOT routines in IRAF for a comparison. Under normal circumstances the standard DAOPHOT routines would have be fine to use, however, due to nature of the R136 data, there were several potential benefits in using an `idl` program tailored towards the observations. When using small apertures the IRAF routine was found to group pixel values. For example, when the aperture size was set to 2 pixels, instead of calculating the flux within a 2 pixel radius of the cluster core, the flux within the central 16 pixels was measured. The `idl` program re-samples the data as a function of azimuth, ϕ, and radius from the cluster centre, to enable a smoother, more robust calculation at smaller radii. Although interpolation creates a small error

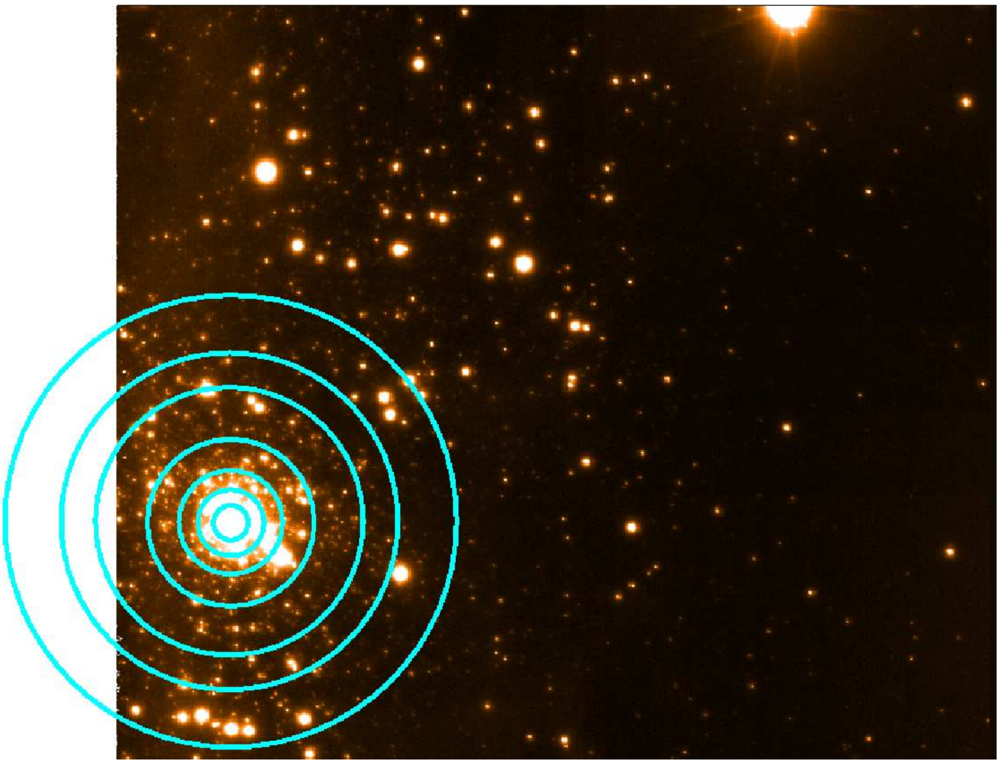

Figure 3.1: Kp1 with the integrated light apertures ($>1\farcs2$) overlaid.

term through the assumption that information between data points is linear, the error introduced is nominal compared to that introduced through incorrect measurement of the varying flux with radius.

As the radius increased, apertures were quickly interrupted by the edge of the field (see Figure 3.1). Information can still be gained from an aperture with a section partially missing. By applying an area correction term, the complete integrated light of each annulus surrounding the cluster core was found (assuming cluster symmetry). The area correction for each annulus was calculated by dividing the number of pixels within each annulus by the theoretical number of pixels per annulus. The final results were compared to aperture values obtained through both IRAF and the STARLINK `gaia` package. All were in good agreement, with small variations, as expected at small radii.

Uncertainties

An accurate calculation of the error associated with each aperture is difficult due to the many different error sources and the role each one plays as a function of radius. The main source of error introduced though the integrated-light method is from the instrument light leak (see Section 2.2.2). The cluster core is situated in the bottom left-hand corner of Field 1 (see Figure 3.1) which was the worst affected region in this regard, particularly in the K_S-band.

A constant sky term is perhaps a rather simplistic scenario as the MAD frames contain regions of varying nebulosity as well as the light leak. Quantifying these effects is, however, difficult.

An estimate on the total uncertainty associated with each annulus was found by dividing each section into 30° angular segments, originating from due north. Assuming that the cluster core is symmetrical, there should be no azimuthal angular variations and any discovered are due to errors/uncertainties associated with the measurements (Section 3.4 finds no evidence to suggest that the core is asymmetric out to r=$11\overset{\prime\prime}{.}2$). Thus, the standard deviation from the segments across each aperture was found and used as uncertainty estimates when fitting cluster profiles (see Section 3.3.4).

3.3.2 Star Counts Measurements

The luminosity profile was compiled at larger radii using star counts from the combined frame catalogues. Although the individual frame catalogues span a larger region than that of the combined frames, meaningful completeness terms were only possible for the latter (see Section 2.4.6). Objects were split into magnitude bins within different radial bins and completeness corrections were then applied, as a function of radii and magnitude (see Figure 3.2). As can be seen, completeness functions in the inner radii really suffer from crowding effects. However, past the first or second bin they become a lot more stable, only degrading again at the outermost radii, where small number effects come into play.

As the cluster core was not situated centrally within the fields, area corrections were

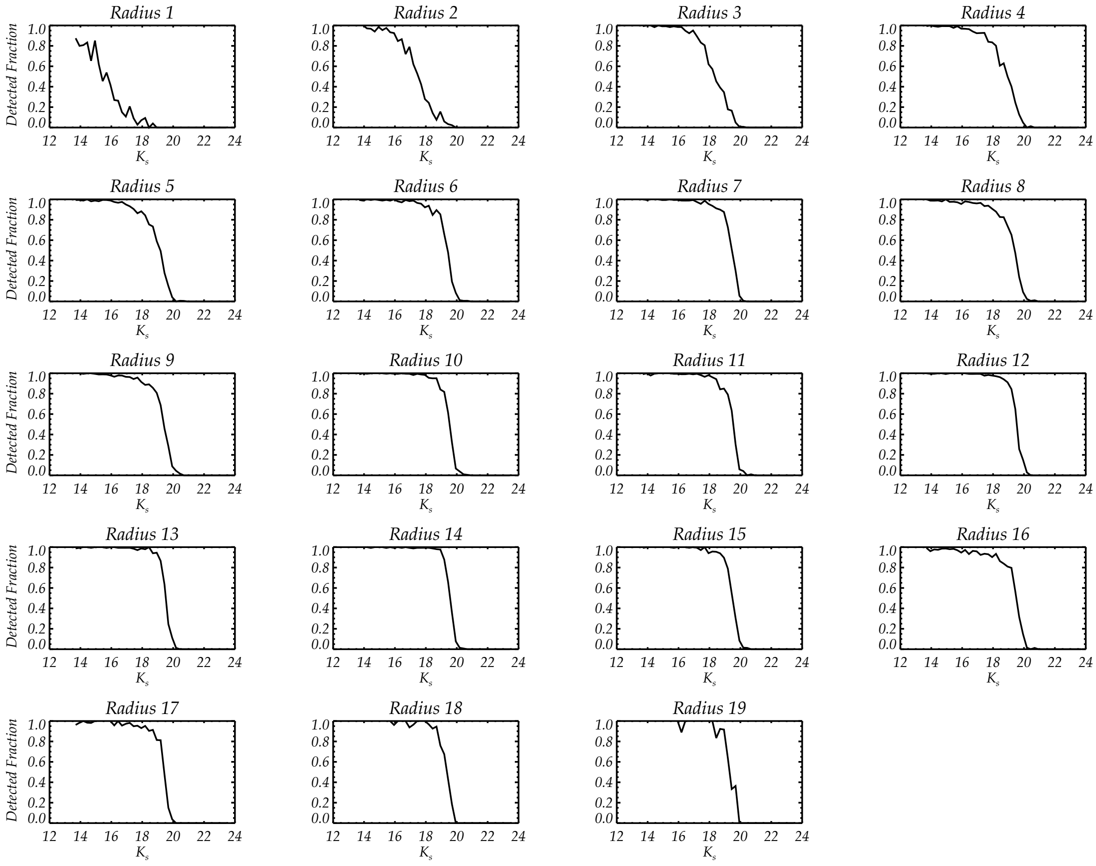

Figure 3.2: K_S-band radial completeness for Field 1. The width of each bin was set to contain equal numbers of objects. 'Radius 1' refers to the annulus closest to the cluster core.

applied to each annulus. The fractional area covered by each annulus within the FoV was calculated by plotting ten million objects uniformly across the field. The radial distance of each object from the cluster centre was calculated, along with the radial distance from the centre of the FoV. The two measurements were split into radial bins, and the ratio of the two gives the fraction of the annulus around R136 contained within the FoV. The radial width of each radial bin was set to contain roughly equal stars per bin.

In crowded regions re-detecting artificial stars for completeness corrections can be particularly difficult. If an artificial star is overlaid upon a real star it can be rejected through the selection criteria. This could be due to the creation of an unusual PSF or a variation in detected magnitude from that of the initially added artificial star. If the magnitude of the recovered star differed by more than 0.5^{m} then it was rejected. It is possible that the newly blended PSF, created from overlapping with a real object, causes it to not be recognised by the DAOFIND routine. If it is detected, it may also get rejected after the PSF sharpness and least squares selection criteria are applied (i.e, if the PSF fits were not good, the object was rejected). Thus, the completeness terms vary depending on the crowding in each annulus and so are radially and azimuthally dependent (due to the asymmetry of the cluster, see Section 3.4).

The completeness corrections were fixed to the magnitude reached by the 50% completeness level in the third annulus. By setting a minimum magnitude correction consistent across all annuli, this ensures that the radial profile probes to the same mass limit across the field. The first radial bin was also removed from the radial profile due to uncertainties from crowding. In fact, crowding within annuli closer than the third annulus leads to unreliable completeness terms, so the radial profile from star count measurements starts at a radius of $5\farcs6$. As the integrated light measurements span this inner region, the whole cluster profile can still be examined.

Uncertainty

The cluster is not perfectly symmetric, (discussed in more detail in Section 3.4), thus the area corrections introduce an additional uncertainty term. Without a complete knowledge of the cluster structure, this uncertainty is difficult to quantify. Combined with the unknown level of confidence in the completeness corrections, it is not possible to calculate overall values of uncertainty. Therefore, conservative ±10% error margins were adopted for the star counts radial profile, which were also included when analysing the combined profiles in the next section.

3.3.3 Combined Radial Profiles

The integrated-light surface brightness and associated error terms were converted into magnitudes arcsec^{-2} in log space. Likewise, the logarithm of the radial star counts data was found. Assuming that there is no mass segregation in a cluster, it is fair to assume that the number of stars (for a given mass function) needed to produce a given luminosity is constant across the cluster. Using this assumption it is possible to normalise the star count data to the integrated light data. If this were not the case, then the luminosity created by one group of stars would not relate to the luminosity at another region and so the star count data and integrated light would not be comparable. Evidence from Hunter et al. (1995) and Andersen et al. (2009) suggests there is no mass segregation within R136, whereas Brandl et al. (1996) suggested that R136 is mass segregated at high masses. However, since then, Ascenso et al. (2009) have found that mass segregation indicators are highly sensitive to incompleteness, and that completeness corrections are not adequate in resolving the problem. In fact, through simulations they found that incomplete observations can lead to the appearance of a mass segregated cluster where none exists. With a lack of strong evidence to the contrary, it has been assumed that R136 is not mass segregated. Therefore, an overlap region between the star counts and integrated light profiles was used to normalise the star count data into surface brightness profiles (magnitudes arcsec^{-2}).

The star count profiles were combined with the integrated light profiles in a consistent manner for all fields by interpolating between both data sets in the overlapping region. Since the radial bins varied in size as a function of radius, it was necessary to interpolate both data sets to an equidistant grid to avoid any weighted bias towards the smaller size bins. The average offset between the data sets was used to convert the star counts data to the correct surface brightness values. Such care is warranted as the method used to ‘stitch’ together the two data sets could alter the slope of the profile. As mentioned, the inner bins of the star counts profile were removed. However, the combined profile was also examined when the inner bins were used and found to make little difference to the resulting profile.

The radial profiles extend to 48" from the cluster core as a combination of both integrated-light and normalised star counts data. The surface brightness profiles approximately follow a power-law to large radii and so EFF profiles were fit following

Equation 3.7. The core radius, r_{core}, is usually defined as the radius where the surface brightness profile drops to half its central value (Portegies Zwart et al., 2010). For an EFF profile, r_{core} follows:

$$r_{core} = a\left(2^{\frac{2}{\gamma}} - 1\right). \tag{3.10}$$

Integrated-light profiles, fit with EFF profiles, can be seen in Figure 3.3. The combined profiles can be seen in Figures 3.4 and 3.5. The EFF profiles were fit using a program written by Dr Mark Gieles. The fits for Field 1 have reduced χ^2 =0.99 & 1.09 for the H- and K_S-band respectively. This indicates that the rather conservative error estimates of ±10% for the star counts data were actually quite appropriate. For Field 3, the χ^2 values are much reduced with values of 0.37 & 0.38 for H- & K_S-band respectively. This suggests that the conservative error margin of ±10% is over generous. There is an overdensity of stars seen at ∼20" in Field 1 which is not present in Field 3. The area corrections for Field 1 therefore introduce a larger error to the surface density in that region. Furthermore, Field 1 has added uncertainty, with the light leak occurring through the centre of the cluster, whereas the light leak is negliable in Field 3. It is therefore perfectly plausible that the error margins associated with Field 3 are smaller than that of Field 1.

3.3.4 Profile Analysis

The EFF parameters obtained from the radial profiles can be seen in Table 3.1. Values in italics refer to the combined profile, whereas normal font are the results from fits to the integrated-light profiles only. The contribution of the star counts data created a slightly shallower slope, by ∼0.1, but the two sets of results are in good agreement within the respective uncertainties. There is little signature of a core from the integrated light data, with the surface brightness profiles fit by a power-law over the full range of the data. The core has a scale radius of $a \sim 0\farcs1$ (0.025pc) which, in practice, is the resolution limit of the data. As it is possible that the core is smaller, but unresolved, $0\farcs15$ provides an upper limit to the core radius. For the γ values obtained, Equation

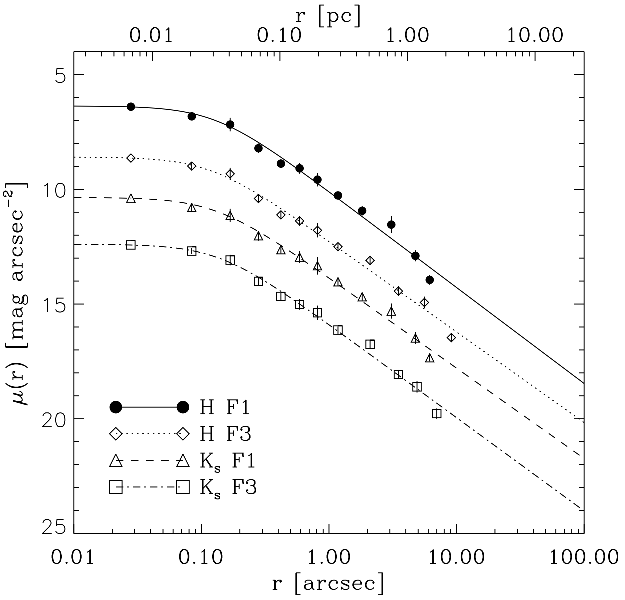

Figure 3.3: EFF fits to the MAD integrated-light profiles, with the K_S-bands and H-band (Field 3) profiles shifted to fainter magnitudes for clarity).

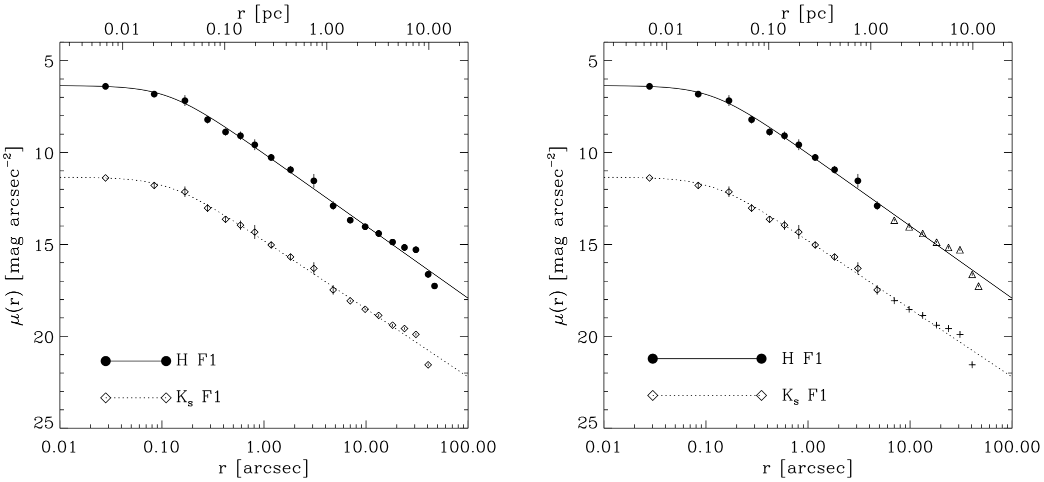

Figure 3.4: EFF fits to the combined MAD profiles for Field 1 (with the K_S-band profile shifted to fainter magnitudes for clarity). Right-hand figure highlights PSF fitting and integrated light measurement regions, with the outer regions indicating PSF fitting.

Table 3.1: Structural parameters for R136 from EFF fits to the MAD integrated-light profiles. The italicised results are from fits to the combined luminosity profiles. For convenience, results are quoted in direct observables and their physical size in pc.

Field	μ_0 [mag arcsec^{-2}]	a [$''$]	γ	r_c [$''$]
H F1	6.37 ± 0.12	0.13 ± 0.03	1.67 ± 0.15	0.15 ± 0.04
	6.36 ± 0.12	*0.12 ± 0.02*	*1.57 ± 0.05*	*0.14 ± 0.03*
H F3	6.59 ± 0.11	0.12 ± 0.03	1.58 ± 0.13	0.14 ± 0.03
	6.59 ± 0.11	*0.12 ± 0.02*	*1.57 ± 0.05*	*0.13 ± 0.02*
K F1	6.35 ± 0.14	0.13 ± 0.04	1.58 ± 0.15	0.15 ± 0.04
	6.35 ± 0.14	*0.12 ± 0.02*	*1.48 ± 0.06*	*0.15 ± 0.03*
K F3	6.39 ± 0.10	0.14 ± 0.03	1.63 ± 0.14	0.16 ± 0.04
	6.38 ± 0.11	*0.12 ± 0.02*	*1.56 ± 0.06*	*0.15 ± 0.03*

Field	μ_0 [mag pc^{-2}]	a [pc]	γ	r_c [pc]
H F1	3.293 ± 0.121	0.031 ± 0.008	1.67 ± 0.15	0.035 ± 0.009
	3.282 ± 0.121	*0.028 ± 0.005*	*1.58 ± 0.05*	*0.033 ± 0.006*
H F3	3.517 ± 0.112	0.028 ± 0.007	1.58 ± 0.13	0.034 ± 0.008
	3.509 ± 0.112	*0.027 ± 0.005*	*1.57 ± 0.06*	*0.032 ± 0.006*
K F1	3.278 ± 0.136	0.031 ± 0.009	1.58 ± 0.15	0.037 ± 0.010
	3.269 ± 0.136	*0.029 ± 0.006*	*1.48 ± 0.06*	*0.035 ± 0.007*
K F3	3.316 ± 0.105	0.033 ± 0.008	1.63 ± 0.14	0.039 ± 0.010
	3.305 ± 0.105	*0.030 ± 0.006*	*1.56 ± 0.06*	*0.036 ± 0.007*

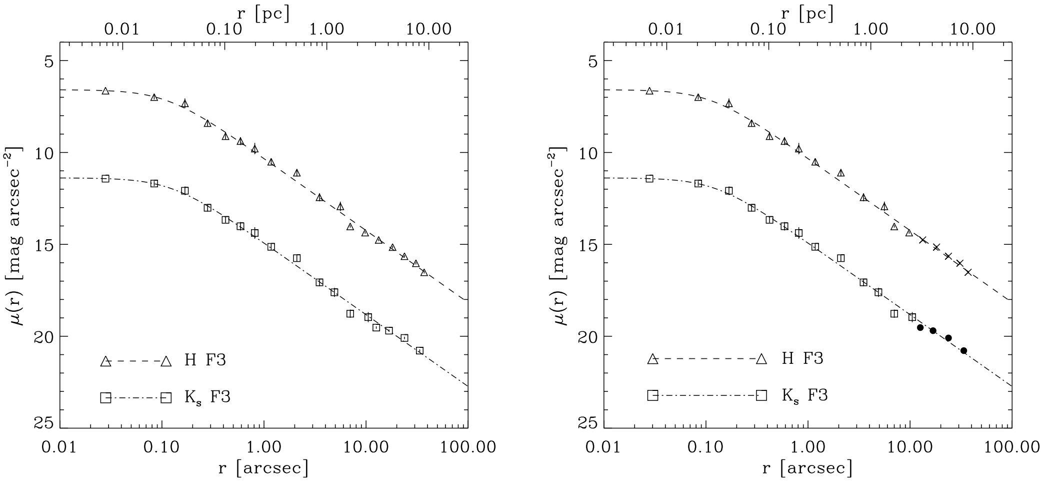

Figure 3.5: EFF fits to the combined MAD profiles for Field 3 (with the K_S-band profile shifted to fainter magnitudes for clarity). Right-hand figure highlights PSF fitting and integrated light measurement regions, where the outer regions indicate PSF fitting.

3.10 gives a core radius of, $r_{core} \approx 1.5a$. Although there is no clear evidence for mass segregation, if the cluster were mass segregated, it could be assumed that the massive stars would have migrated to the core, effectively reducing the core size. Therefore, the primordial core when the cluster was initially forming would be larger than we detect currently.

The slope of the power-law fits ($\gamma \sim 1.6$) were in good agreement for both fields 1 & 3. It would have been possible to combine the two fields to create a more complete profile, however, as stated in Section 3.3.5, in order to make a fair comparison with Mackey & Gilmore (2003) results it was necessary to treat the fields separately. Due to the agreement in slope values between fields 1 & 3 it was deemed unnecessary to calculate the radial profile with the field 1 & 3 data combined as this would have resulted in an average of the two already computed profiles.

The slope of the power-law fits are also in good agreement with past *HST* results in the optical, where Campbell et al. (1992) found a power-law slope of $\gamma = 1.72 \pm 0.06$. From visual inspection of the radial profiles in the optical by Hunter et al. (1995), their slopes were slightly shallower than r^{-2}, suggesting a value of $\gamma \sim 1.1$, somewhat steeper than the MAD value. The NICMOS values from Andersen et al. (2009) are also in close agreement with the MAD data, with $\gamma \simeq 1.55$.

Cluster Formation

The EFF fits in R136 have a slope of ≤ 2 which could be a signature of the formation process. R136 could have retained the profile of the original isothermal cloud and evolved with time to the γ value observed today through stellar evolution and heating from binaries as suggested by Larsen (2004). It would, however, be surprising if these processes have played a significant role in the cluster structure, given its young age. It is more likely that the slope of the profile is a remnant only of the formation process.

The value of γ could be evidence of dissipationless collapse - the cluster forming with a high star formation efficiency, using most/all of gas in the cloud to form stars. If the cluster formed from cloud collapse, with star formation occurring early on with a very high efficiency, the stars would form with velocities of the in-falling cloud and would collapse in a non-dissipative manner, satisfying the initial conditions simulated by McGlynn (1984). Furthermore, as there would be little gas left over from star formation, RGE would have little effect in disrupting the cluster, with a corresponding lack of excess light predicted.

3.3.5 Evidence for Rapid Gas Expulsion

Consistency with HST data

One of the main aims of investigating the radial profile of R136 with the MAD data is to compare the results with the *HST* observations of Mackey & Gilmore (2003). In order to make a fair comparison, the methods used to calculate the profiles for the *HST* data were replicated exactly for the MAD data. Indeed, the author of the *HST* results, Dr Dougal Mackey, was also an author on the MAD results and was consulted throughout on how to make the comparison as similar as possible. When comparing to the MAD profiles, the *HST* results were re-calculated, restricting the data to the same radius as the MAD profiles. The central region of the *HST* data extends over the region most closely matched by MAD Field 1. As Figure 3.6 illustrates, there is a small difference in the region covered by the MAD Field 1 and *HST* data, a small triangular section. Inspection of this region with both data sets shows few stars within the region giving confidence that the difference has little effect on the resultant profiles. By using the exact same methods of Mackey & Gilmore (2003) and calculating profiles over comparable regions, the profile techniques of MAD and *HST* are considered consistent.

Comparison with *HST* results

A comparison between the MAD profiles and that of Mackey & Gilmore (2003) seems to show startling differences (see Figure 1.3.1). The existence of a bump or dent at $\sim$10" in the optical data suggests a second component in the profile. Mackey & Gilmore (2003) suggested that the profile consists of two components, finding $\gamma = 2.43 \pm 0.09$ for the inner 10". In contrast, the MAD integrated light data at $r < 1$" rule out such a steep turnover in the N-IR.

Armed with the knowledge that the optical data 'turns' over earlier than the N-IR data, the core of the optical data was removed in order to directly compare the slope of the power-laws. Fitting an EFF profile over the new radius range revealed $\gamma = 1.80 \pm 0.10$ in both V and I-bands, in reasonable agreement with the MAD data, as illustrated in Figure 3.7. Note that McLaughlin & van der Marel (2005) re-analysed the profile from Mackey & Gilmore (2003) over the full extent of the *HST* data and found $\gamma = 2.05$.

Mackey & Gilmore (2003) fit the inner region with an EFF profile, and the outer region with a King profile. A similar bump or dent in the profile was also observed by Meylan (1993) for B and V-band data from the ESO 2.2m telescope. There is tentative evidence for a 'bump' at a comparable radius in the Field 1 of the N-IR MAD data, but Field 3 follows a much tighter single component fit in both H and K_S-bands. To investigate possible causes of discrepancy between the results, the asymmetry of the

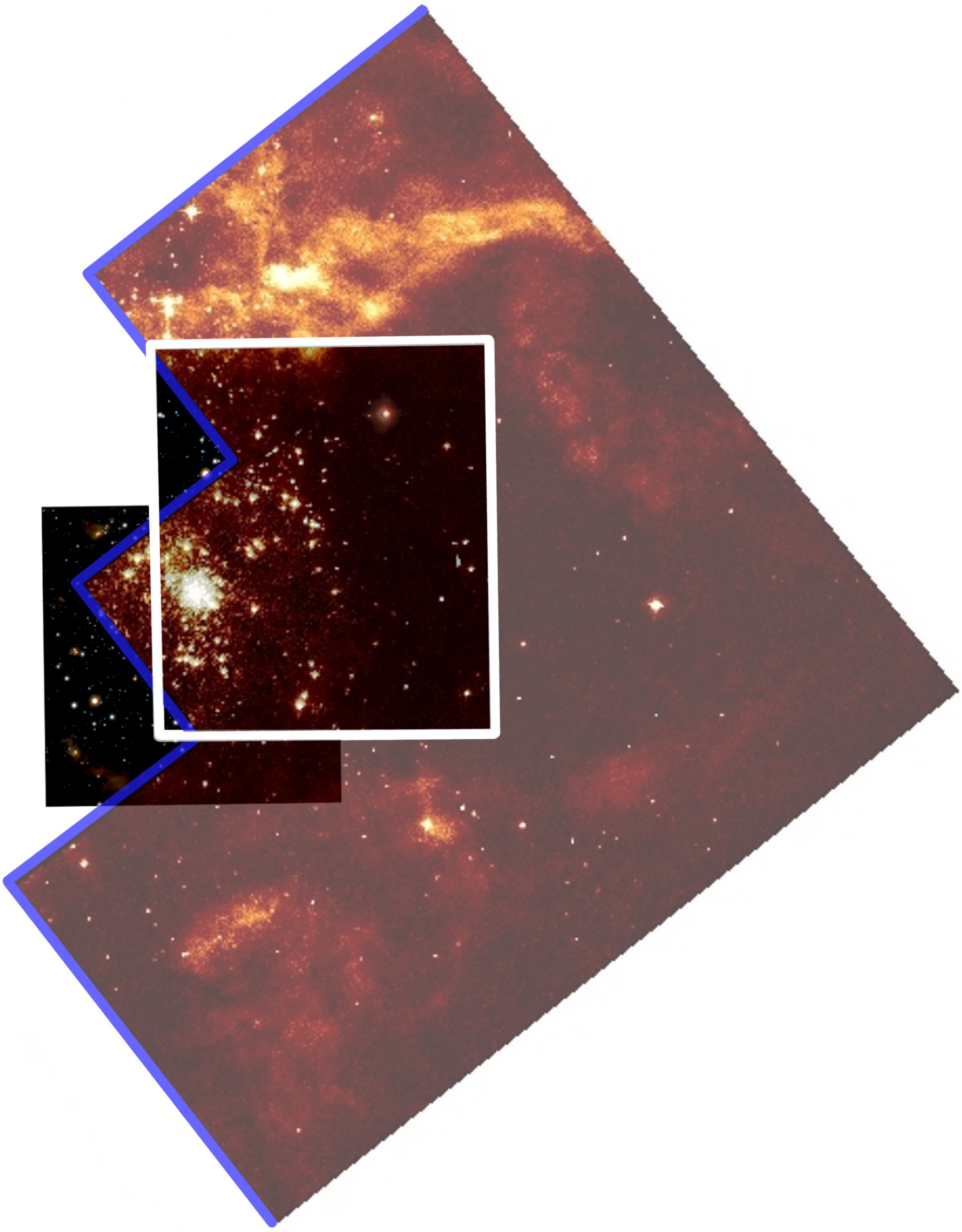

Figure 3.6: Comparison of *HST* and MAD regions. The white frame represents MAD Field 1, which most closely matches the radial profile of the *HST* radial profile. The *HST* data was truncated to the radial extent of the MAD Field 1 region when making a comparison. MAD Field 3 extends to the bottom left of Field 1.

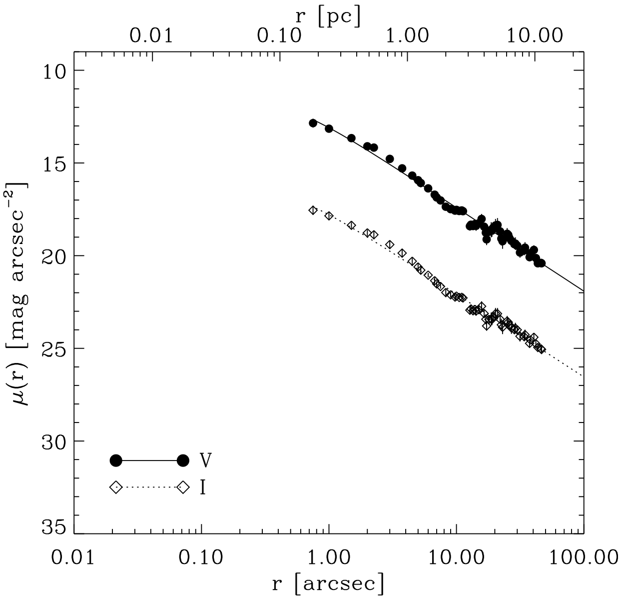

Figure 3.7: EFF fits to Mackey & Gilmore (2003) *HST* data.

cluster was considered.

3.4 Asymmetry

To understand the MAD results better in the context of RGE, the symmetry of R136 was investigated by studying the azimuthal star count density distribution. R136 is still in the early stages of its evolution. Being so young, it is unlikely that the cluster has had time to relax and so any structure within the cluster is likely to be a signature of the primordial cloud from which the cluster formed. Analysing the density distribution of the cluster may provide insight into the process of formation, while also providing an explanation to the lack of "bump" observed in the N-IR.

The azimuthal profile of R136 was investigated through the measured level of star counts from the MAD photometric catalogues. An `idl` program was written to split the image into angular "slices", each containing a roughly equal number of objects after completeness corrections were applied (thus the angular extent of each slice varies).

The radial positions of the observed stars were found, relative to the cluster core. Objects within a $2\farcs8$ radius of the core were removed (due to crowding affecting completeness as mentioned in Section 2.4.6). Due north from the cluster core was set as the angular origin. The azimuthal asymmetry was investigated for various radii, with the maximum radius set to accommodate a comparable sweep through Fields 1 & 3. Initially a 0.5° slice was created and the completeness and number of observed objects was determined. Completeness corrections were applied, finding the total number of objects for that slice. If it contained the required number, then the slice was accepted and the process was repeated for the next 0.5° slice. If, however, there were not enough objects, then the slice was increased to 1°. After completeness corrections, the total number of objects within that slice was again found. This iterative process was repeated until the set number of objects were contained. The number of objects required for each slice was set be high enough so that a large span of magnitudes was included within each slice, while small enough that spatial density information was not lost through low azimuthal resolution. The number of objects required varied depending on the radial extent of the slices.

Figure 3.8 shows the first azimuthal slice for K_s Field 1 with completeness corrections down 50% complete applied. The level of completeness correction was initially set at 50%, although to investigate the impact of completeness on the final distributions, test were carried out at the three different levels.

3.4.1 Results

The azimuthal variation around R136 (with $r_{\max}$=$28\farcs0$, $\equiv$ 1000 pixels) can be seen in Figure 3.9. Using a distance modulus to the LMC of 18.5 (Freedman et al., 2001), the projected radius of 28" corresponds to ~6.8pc (likewise, $22\farcs4$ = 5.4pc, $16\farcs8$ = 4.1pc, and $11\farcs2$ = 2.7pc). There is a clear asymmetry to the cluster, observable at all radii, except $r_{\max}$=$11\farcs2$. It is not clear if the asymmetry of the cluster disappears at the inner region, or if the completeness terms within this region become unreliable due to crowding effects, clouding any structure that may exist. Note that the H-band data goes

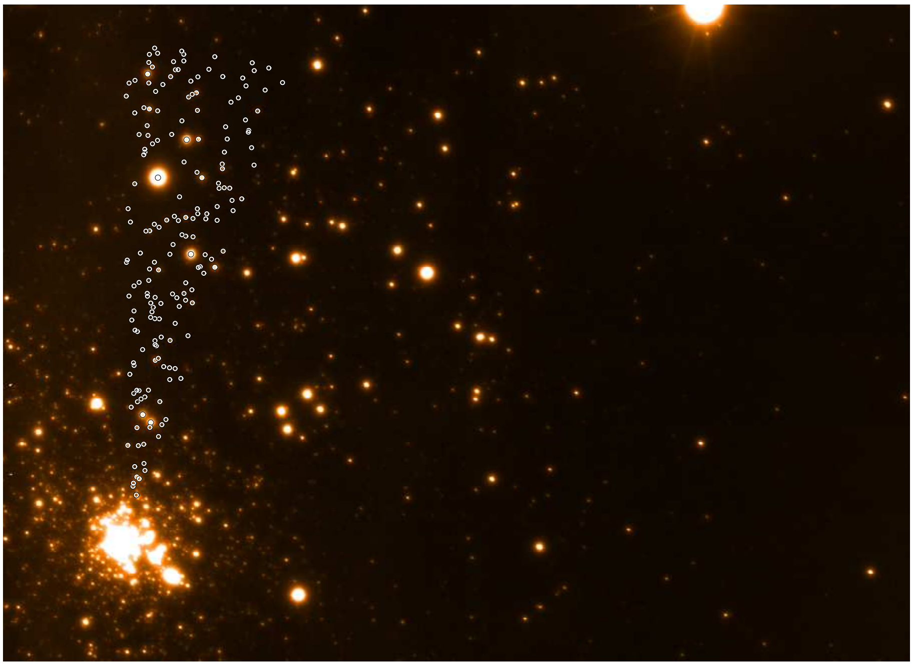

Figure 3.8: Detected objects within the first azimuthal slice for K_s Field 1.

deeper than the K_s observations and hence the density values are higher. Different radii appear to show a variance in the positions of the peaks and troughs of the distribution. This is a binning effect caused by each slice requiring the same number of objects. Different radii cause slices to have different angular extents and so become centred on different angular positions. The trend, however, is the same for all.

To confirm that completeness corrections have not artificially created the asymmetric distributions, different corrections were carried out. Completeness levels of 30% and 40% were applied (see Figures 3.11 and 3.10). Varying the level of completeness was found to have little effect on the resulting distribution. The cluster is seemingly unrelaxed, suggesting the asymmetry of the cluster is a consequence of the formation process. It is unsurprising to find regions of 'clumpiness' within such a massive and complex star-formation region.

The MAD data cover the central 2' of 30 Dor, which at a distance of $\sim 5 \times 10^4$pc corresponds to a physical size of $\sim$30pc. If this distance is projected to 10Mpc, the same structure would be contained within $\sim 0\overset{\prime\prime}{.}5$. Therefore it is important in distant,

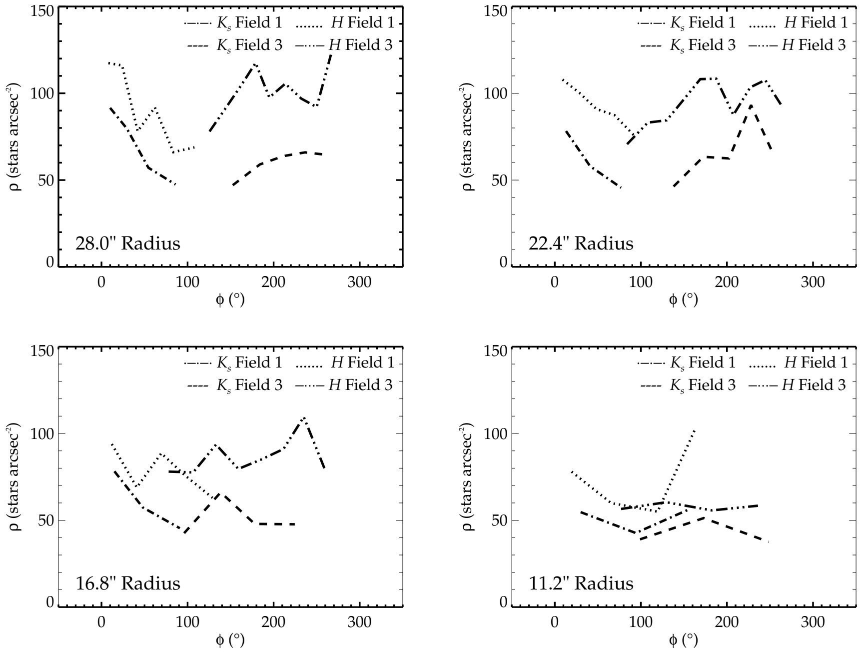

Figure 3.9: Azimuthal profiles for 50% completeness, for varying radii.

unresolved clusters to take into consideration the potential asymmetries that could affect the surface brightness profiles. Surrounding R136 are regions of triggered star formation which will inevitably become included in the outer regions of the cluster profile. These second generation objects will lead to unexpected increases in density at large radii, particularly in older clusters where enough time has elapsed for large scale triggered star formation to occur. For distant clusters different generations of star formation will be indistinguishable in integrated light profiles. These are important considerations when interpreting the radial luminosity radial profiles of distant clusters.

3.5 Summary

The N-IR radial profiles for the MAD data show no clear evidence for a bump as observed by Mackey & Gilmore (2003) in the optical with *HST*. If the excess light

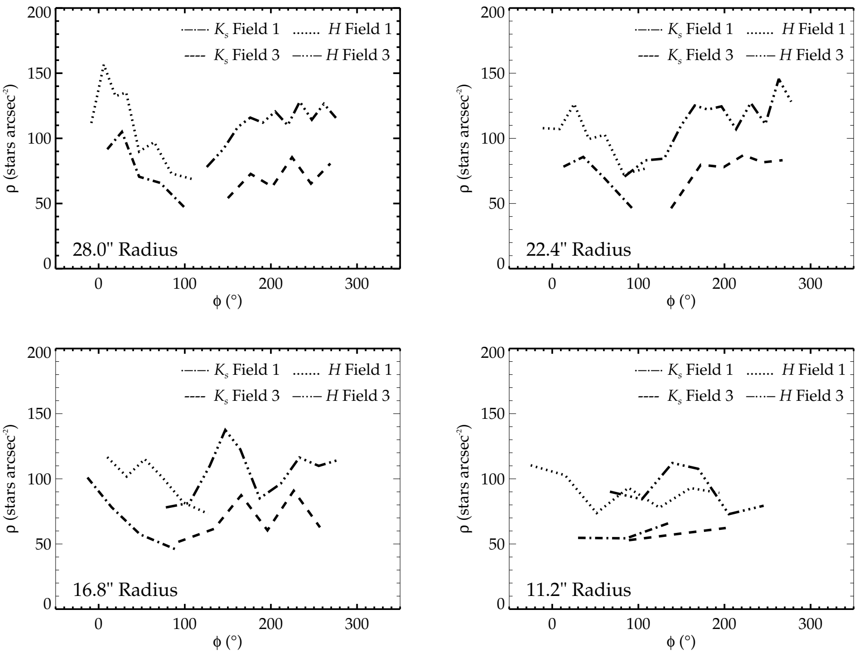

Figure 3.10: Azimuthal profiles for 40% completeness, for varying radii.

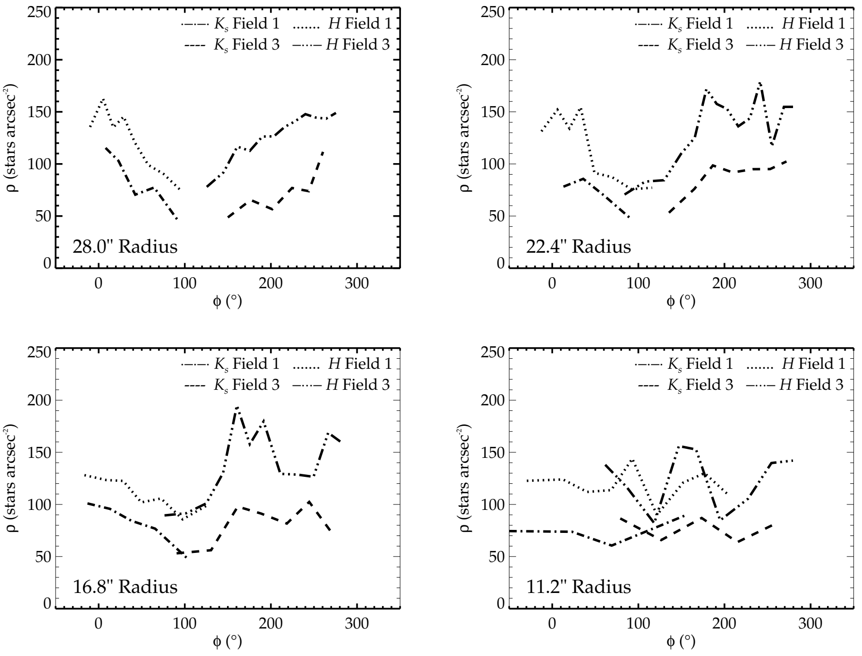

Figure 3.11: Azimuthal profiles for 30% completeness, for varying radii.

is created by ejected stars, it should be wavelength independent and so its signature should be observable in the N-IR data. This suggests that RGE is not occurring in R136, although it still could well account for the other profiles observed by Bastian & Gieles (2008).

The difference in profiles between the N-IR and optical make it tempting to attribute the second component in the optical data to variable extinction, where the effect is reduced in the N-IR. A visual inspection of R136 in the optical (see Figure 3.12) shows a notable 'void' of stars to the north-east (running from north-west to south-east) at $\sim$ 10” from the cluster core. This 'void' is also apparent in the MAD data (also see Figure 3.12), although less obvious. We suggest differences in the outer sections of the Field 1 & 3 profiles are likely a consequence of the azimuthal asymmetries observed across the cluster. Further support of this hypothesis is provided by inspecting the original Wide Field Planetary Camera 2 (WFPC2) images used by Mackey & Gilmore. The core of R136 is located off-centre of the detector, mainly sampling to the east of the core. This is essentially the same region as Field 1, where there is also a possible argument for the existence of a bump. Furthermore, Andersen et al. (2009) only fit EFF profiles out to $8\overset{\prime}{.}25$ from the cluster core citing that beyond this bright stars start to dominate, introducing “jitter in the surface brightness profile”.

Perina et al. (2009) found a similar break in the surface brightness profile for the brightest open cluster in M31, VdB0. After suggesting that the break in the profile might be due to the elongated distribution of the cluster, they re-calculated the surface brightness, fitting elliptical instead of circular apertures. This removed the break in the cluster. It is possible that the asymmetry in R136 is having a similar effect on the profiles of Field 1. Assuming the cluster is spherical is not adequate under these conditions.

This is not necessarily the 'end' of the RGE concept, but it does demonstrate that care should be taken in explaining such features in profiles of unresolved clusters.

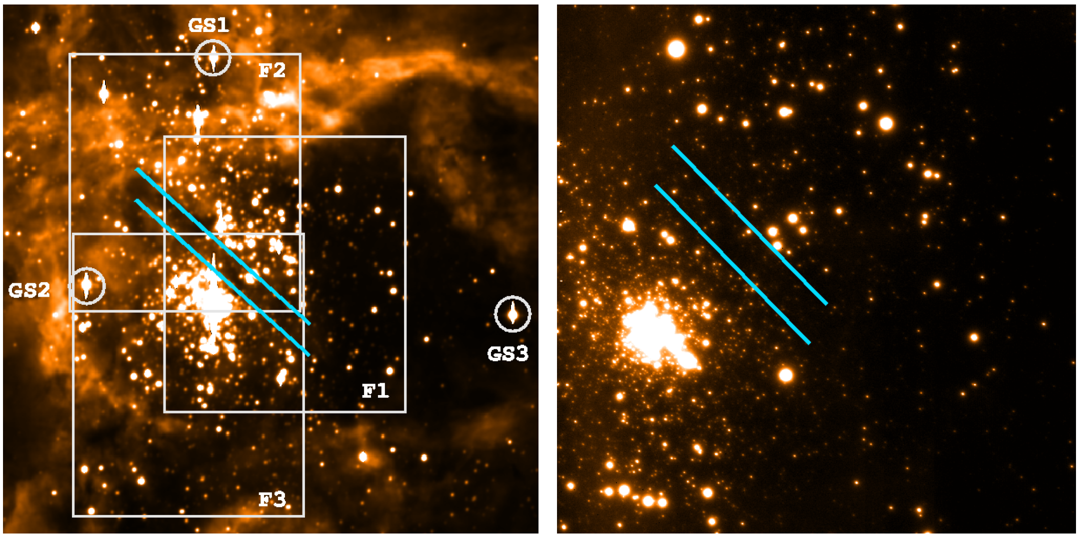

Figure 3.12: The region to the NE of R136 (highlighted by the blue tram lines), which appears to show a deficit of stars. *left*: WFI optical image; *right*: N-IR MAD K_sField 1.

Chapter 4

Young Stellar Objects with MAD and HAWK-I

The exceptional resolution provided by HAWK-I, and more so by MAD, presents the perfect opportunity to investigate the nature and morphologies of Young Stellar Objects (YSOs) surrounding R136. Previous surveys of YSOs in the 30 Dor region have been carried out in various wavebands (see Section 4.2). Two different groups investigated one data set using different section criteria. The different selection techniques resulted in differing numbers of YSOs. Part of the survey was carried out in the 30 Dor region of the LMC, giving the opportunity for the MAD and HAWK-I data to re-investigate the sources, distinguishing multiple systems and gleaning any other evidence suggesting/doubting the existence of a YSO. Multi-epoch VLT-FLAMES observations have also been gained for some objects, allowing the determination of spectral types and if they are binaries (see Section 4.3.1). The end aim is to determine which selection criteria results in the largest number of YSOs with little contamination. Can selection criteria be relaxed, or will this result in a largely contaminated catalogue?

4.1 YSO Introduction

YSOs can provide a wealth of information on the processes of star formation. The location and distribution of YSOs trace out new regions of star formation and can highlight the influence that surrounding environments have had in kick-starting the formation process. In the case of R136, this could indicate the influence of the YMC on the surrounding region as outflows and ionising radiation trigger a new generation of star formation (Walborn & Blades, 1997).

Recent observations (Davies et al., 2010) have suggested that intermediate to high mass (10-20$M_\odot$) stars form in a similar manner to low mass stars, gaining mass through accretion, and losing angular momentum through bipolar outflows (see Section 3.1.1). Whether this holds for even higher mass stars is unknown, especially the colossal stars ($>$200$M_\odot$) at the core of R136 revealed by the new analysis by Crowther et al. (2010) (see Section 6.1). Studying the properties and morphologies of YSOs provides insights into how massive stars gain such mass, while also providing opportunities to explore other remaining questions, such as how do the majority of stars form in binaries/multiples as observations suggest (Mason et al., 2009)?

YSOs exhibit different SEDs from main-sequence stars as they are yet to blow-out the surrounding dust which aids their formation. The dust absorbs stellar radiation and re-emits at IR wavelengths. With time, the dust is blown away and the IR excess diminishes. Lada (1987) describes the evolutionary state of a YSO in terms of its SED, distinguishing between type I, II, and III (see Figure 4.1). Chen et al. (2009) describes the types of YSO in terms of physical processes and evolutionary stage.

- Type I - compact accretion disc and a large infalling envelope with bipolar cavity. The SED is dominated by emission from the envelope, being broader than blackbody distributions and rising longward of 2μm.
- Type II - has dispersed most of the envelope and is surrounded by a flared disc. The SED is dominated by emissions from the central source and the disc (and is again broader than blackbody distributions). Longward of 2μm the distribution

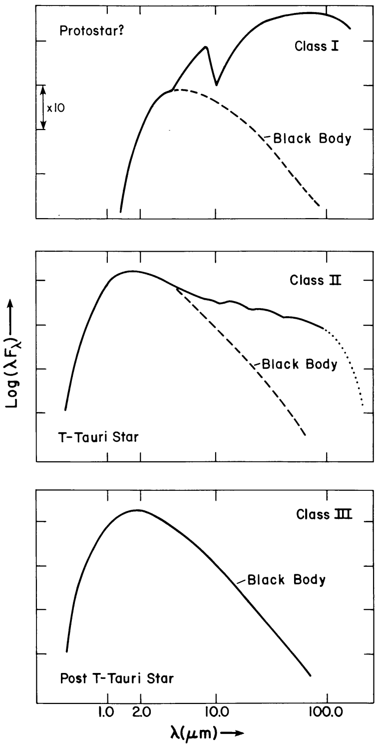

Figure 4.1: YSO SED classification plots from Lada (1987).

is flat or negative.

- Type III - has cleared most of the disc so its SED represents a reddened stellar photosphere of a star very near, or on, the Zero Age Main Sequence (ZAMS). There is little or no excess in the N-IR.

A number of YSO candidates have been investigated around R136, through work carried out by different astronomical groups. The rest of this chapter focuses on YSO candidates which were initially observed in the *Spitzer* SAGE survey (Meixner et al., 2006).

4.2 Surveying the Agents of a Galaxy's Evolution (SAGE)

The *Spitzer Space Telescope* is an 85cm IR space telescope launched in August 2003 (Werner et al., 2004). *Spitzer* operated at a temperature of 5.5K for five years before the coolant ran out, and is now operating in a second "warm mission" phase. During the first five years, two imagers and a spectrograph were operational, gathering measurements from 3.6 to 160µm. The InfraRed Array Camera (IRAC) has a FoV of $5\overset{\prime}{.}2\times5\overset{\prime}{.}2$, with four channels operating at 3.6µm, 4.5µm, 5.8µm and 8.0µm. It has a 256×256 pixel detector array, with a pixel size of $1\overset{\prime\prime}{.}2$ (Fazio et al., 2004). The Multiband Infrared Photometer (MIPS) operates at 24µm, 70µm and 160µm. The 24µm channel has a 128×128 detector array covering a FoV of $5\overset{\prime}{.}4\times5\overset{\prime}{.}4$.

'Surveying the Agents of a Galaxy's Evolution' (SAGE) is a survey that used IRAC and MIPS to image a $7^\circ\times7^\circ$ region of the LMC in order to "trace the life cycle of baryonic matter" (Meixner et al., 2006). SAGE measured photometry of stars (and studied the ISM), cross-matching objects with J, H and K_s-band 2MASS data. A key aim of the SAGE survey was to map the populations of IR sources down to the confusion limit of the telescope, gaining data on fainter, dustier objects than previous surveys, and with better resolution. SAGE also maps the emission from diffuse gas, molecular clouds, and HII regions. The survey was carried out over two epochs in 2005. Completeness tests by Gruendl & Chu (2009) found the photometric catalogue in the LMC to be 90% complete down to 16.0, 15.0, 14.3, 13.1, and 9.2^m at 3.6µm, 4.5µm, 5.8µm, 8.0µm, and 24µm respectively. These sensitivities should allow detection of YSOs down to a few solar masses (Werner et al., 2004).

Whitney et al. (2008) (WH08 hereafter) used CMDs from the SAGE survey to select candidate YSOs in the LMC. Informed by the location of YSOs in CMDs from models of radiative transfer (Robitaille et al., 2006), WH08 applied selection criteria which remove sources likely to be associated with other sources, such as background galaxies and evolved stars. They acknowledge that only accepting YSOs occupying

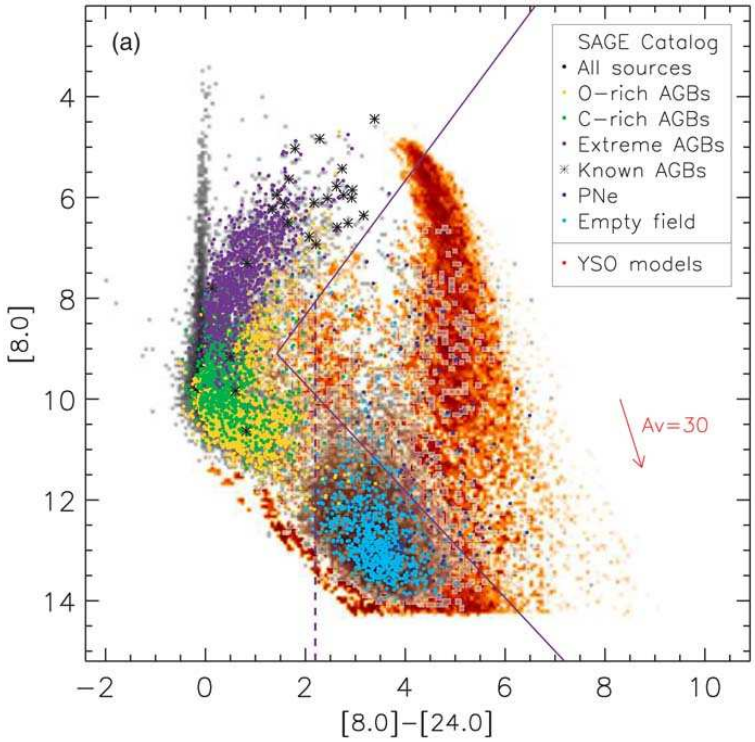

Figure 4.2: CMD from Whitney et al. (2008) indicating different populations. The purple lines divide YSOs from other populations.

CMD positions separate from other populations will miss some YSOs from the final list, but this was preferred to having a potentially more complete but more contaminated list. Figures 4.2 and 4.3 show the SAGE CMDs with the model YSO positions and selection criteria over-plotted. The simulated YSO CMD positions indicate that the selection cuts bias the sample towards younger evolutionary stages and intermediate to high mass YSOs. WH08 do not use the lower spatial resolution MIPS 70µm or 160µm data, making them insensitive to the youngest, heavily embedded sources. The most massive YSOs illuminate large volumes and so are also excluded from the YSO list as they do not appear as point sources. The remaining objects are cross-matched with other catalogues to remove contaminating sources, such as AGB stars and Planetary Nebula (PNe). Another colour cut (J-[3.6])≥3 was applied to remove extreme AGB stars.

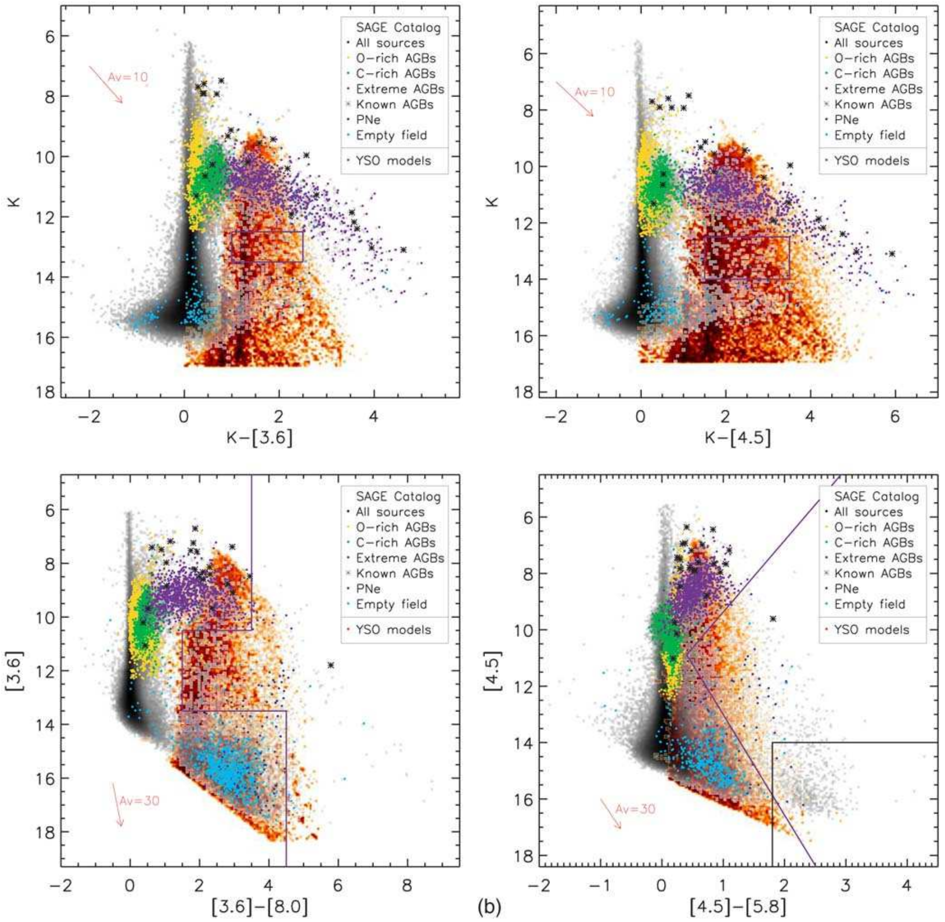

Figure 4.3: CMD from Whitney et al. (2008) indicating different populations. The purple line divides YSOs from other populations. The dashed line shows the colour cut employed to remove AGB stars and galaxies.

Independently, Gruendl & Chu (2009) (GR09 hereafter) have also used the SAGE data to find candidate YSOs in the LMC, but with less stringent selection criteria, in order to obtain a more comprehensive sample. To exclude normal and evolved stars, objects were selected to have [4.5]-[8.0]$>$2.0, and to exclude background galaxies, [8.0]$>$14-([4.5]-[8.0]). An assessment on the nature of the selected objects was made by studying their morphologies, spectral energy distributions (SEDs) from the optical to mid-IR, and inspecting the surrounding stellar environment. Each object was classed as either "definite", "probable", or "possible". In practice, "probable" means that the object is likely to be a YSO, but it cannot be ruled out as being something else. "Possible" means it is unlikely to be YSO but cannot be completely ruled out.

GR09 note that $\sim$70 of their "probable" YSOs are not in the WH08 catalogue due to their conservative point-source identification criteria. Furthermore, GR09 find that 20-30% of the YSOs from WH08 are background galaxies.

Both techniques are dependent on 2MASS data for J, H, and K_S-band photometry. 2MASS has a resolution limit of 2" (Skrutskie et al., 2006), while IRAC achieves a similar resolution ($1\farcs7$-$2\farcs0$) from 3.6 - 8μm. At a distance modulus of 18.5, a projection of 2" in the LMC corresponds to $\sim$0.5pc. In crowded regions such as 30 Dor, multiple components likely occupy regions 0.5pc in size and so it is likely that the photometric magnitudes are of composite sources.

Vaidya et al. (2009) (VA09 hereafter) examined the YSO candidates of Gruendl & Chu (2009) with Hα data from *HST*, and J and K_s data from the IR Side Port Imager (ISPI) on the 4m telescope at the Cerro Tololo Inter-American Observatory. ISPI has a pixel size of $\sim0\farcs3$ (Probst et al., 2003) and is seeing limited. They created Spectral Energy Distributions (SEDs) using data from the Digitized Sky Survey red images, *HST* Hα, ISPI J and K_s-band, and the *Spitzer* [3.6], [4.5], [5.8] and [8.0], and MIPS [24] bands. They also used the lower resolution MIPS [70] and [160] images. The SEDs are used to determine the evolutionary stage of the YSOs, as defined by Lada (1987). The high resolution *HST* images were used to determine if objects were resolved into multiple components and also to study the morphology and environment the YSOs reside in.

Table 4.1: YSO candidates from Gruendl & Chu (2009) within the MAD and HAWK-I frames.

Definition	RA and Dec (J2000)	[3.6]	[4.5]	[5.8]	[8.0]	[24]	Counterparts
Definite	05:38:39.24 −69:05:52.3	11.27	10.40	8.98	6.93		Multiple
Definite	05:38:53.88 −69:09:31.3	11.77	11.45	9.20	7.48	2.58	Single
Definite	05:38:05.64 −69:09:09.0	11.06	10.39	9.12	7.25	2.04	Multiple
Definite	05:38:15.24 −69:06:54.5	12.37	11.94	9.81	8.148	2.58	Multiple
Definite	05:38:33.09 −69:06:11.8	12.16	10.76	8.64	7.31	2.58	Single
Definite	05:38:34.77 −69:06:06.1		10.39	9.57	7.12		Multiple
Definite	05:38:39.69 −69:05:38.1	9.50	8.17	6.96	6.06		Multiple
Definite	05:38:45.15 −69:05:07.9	10.18	9.46	7.78	6.06		Multiple
Definite	05:38:31.62 −69:02:11.0	10.21	9.37	7.72	5.73		Single
Definite	05:38:48.17 −69:04:11.7	10.11	9.33	7.80	6.01		Multiple
Definite	05:38:49.27 −69:04:44.4	10.30	9.12	7.55	5.96		Single
Definite	05:38:52.67 −69:04:37.5	10.99	10.50	8.60	6.98		Multiple
Definite	05:38:58.42 −69:04:34.7	12.57	11.74	9.59	7.71		Single
Definite	05:38:56.48 −69:04:17.0	10.74	9.09	7.54	6.14	1.23	Multiple
Definite	05:39:04.42 −69:04:13.9	11.91	11.82	9.25	7.53	2.36	Single
Probable	05:38:45.99 −69:09:30.8	13.89	13.77	11.33	9.64		None
Probable	05:38:48.86 −69:08:28.0	14.60	13.53	12.37	11.13		Multiple
Probable	05:39:18.47 −69:07:40.5		12.77	10.61	8.87		None
Probable	05:38:21.10 −69:06:17.2	13.21	12.86	11.85	10.04		Multiple
Probable	05:38:22.44 −69:06:44.4	14.10	13.19	11.81	10.46		Single
Probable	05:38:27.39 −69:08:09.0	12.99	12.27	10.59	9.83		Single
Probable	05:38:38.46 −69:04:18.3	12.19	11.27	10.28	8.00	1.08	Single
Probable	05:38:41.23 −69:02:59.0	13.27	12.52	10.89	8.74	3.02	Multiple
Probable	05:38:09.98 −69:03:22.0	13.74	12.95	11.43	9.68		None
Probable	05:38:34.06 −69:04:52.2	9.88	8.88	7.59	6.12		Multiple
Probable	05:38:55.56 −69:04:26.5	11.69	11.37	10.48	9.12		Multiple
Possible	05:38:44.32 −69:03:29.9	13.12	12.70	10.84	9.09		Multiple
Possible	05:38:39.02 −69:02:06.2	13.14	13.27	10.44	8.68		None
Possible	05:38:43.52 −69:06:29.0	13.70	12.36	10.93	9.19		Multiple

Continued on next page...

Table 4.1: YSO candidates from Gruendl & Chu (2009) within the MAD and HAWK-I frames (continued).

Definition	RA and Dec (J2000)	[3.6]	[4.5]	[5.8]	[8.0]	[24]	Counterparts
Possible	05:39:14.78 −69:08:16.6	14.15	13.97	11.36	9.58		None
Possible	05:38:13.42 −69:06:44.4	12.91	13.00	10.11	8.33		None
Possible	05:38:25.21 −69:04:05.2	13.47	13.57	10.79	9.02		None
Possible	05:38:10.41 −69:02:22.1	14.24	13.83	11.98	10.17		None
Possible	05:38:00.29 −69:03:10.1	13.58	13.09		9.36		None

4.3 Spitzer YSO Candidates

With the benefit of the new, high-quality images, the YSO candidates from GR09, found within the MAD and HAWK-I frames, are now investigated; Table 4.1 gives the IR values measured by GR09. The “resolved” column details whether the objects have an obvious partner object within a 2" radius in the HAWK-I and MAD images and are classed as either “Single” or “Multiple”. If no counterpart is found then the location is marked as “None”.

- Definite YSOs

  There are 15 “definite” YSOs within the HAWK-I data, three of which are in the MAD frames. Postage stamps of the “definite” YSOs within the HAWK-I frames can be seen in Figures 4.4 & 4.5. Nine of the objects appear to have multiple counterparts in the HAWK-I frames. Nine are also very red in their N-IR colours and 13 appear to have gas associated with them.

- Probable YSOs

  There are 11 “probable” YSOs in the HAWK-I frames, none of which are in the MAD frames. Five appear to be multiples within 2". Three are either significantly offset from the *Spitzer* location or, more likely, are not visible in the HAWK-I frames and appear as gas. All of them are in gaseous regions, although it is not immediately clear if the gas is associated with them or not. Postage stamp images from the HAWK-I data can be seen in Figure 4.6.

- Possible YSOs

  There are eight “possible” YSOs in the HAWK-I frames, one of which is in the MAD frames. Two are resolved as multiples, however, the rest appear to have no counterparts in the HAWK-I data. The HAWK-I imaging of the possible YSO candidates is shown in Figure 4.7.

All of the GR09 candidates with apparent counterparts in the MAD and HAWK-I frames are summarised in Table 4.2, and overplotted on the HAWK-I K_S-band frames in Figure 4.8. Individual YSOs that have clear single or multiple counterparts within the MAD and HAWK-I frames are discussed in more detail in the following section.

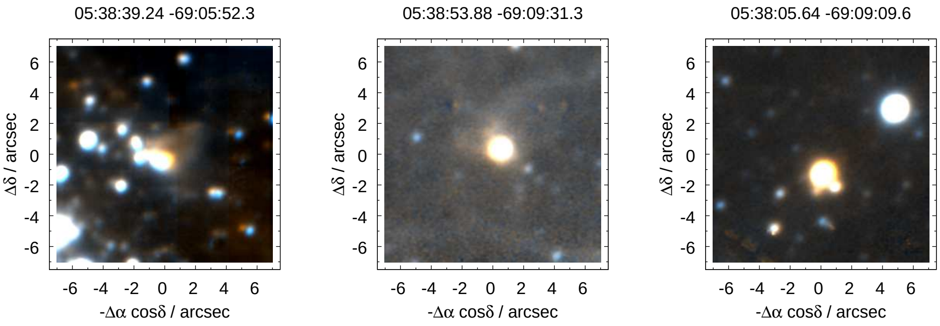

Figure 4.4: False colour HAWK-I images of “definite” YSO candidates from Gruendl & Chu (2009).

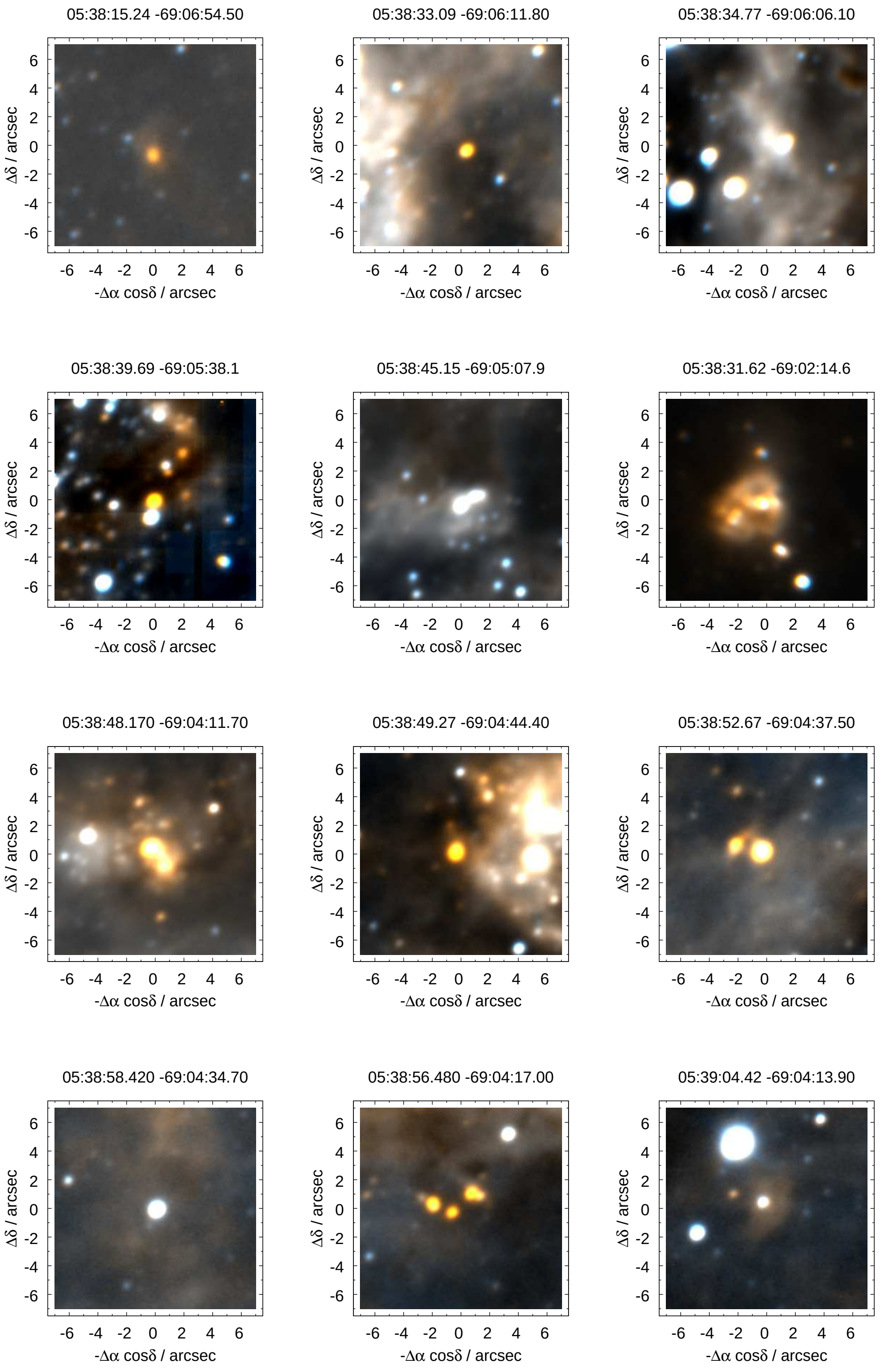

05:38:15.24 -69:06:54.50

05:38:33.09 -69:06:11.80

05:38:34.77 -69:06:06.10

05:38:39.69 -69:05:38.1

05:38:45.15 -69:05:07.9

05:38:31.62 -69:02:14.6

05:38:48.170 -69:04:11.70

05:38:49.27 -69:04:44.40

05:38:52.67 -69:04:37.50

05:38:58.420 -69:04:34.70

05:38:56.480 -69:04:17.00

05:39:04.42 -69:04:13.90

Figure 4.5: False colour HAWK-I images of “definite” YSO candidates from Gruendl & Chu (2009).

Table 4.2: GR09 YSO candidates with N-IR counterparts in the HAWK-I and MAD images. Quoted magnitudes are obtained through PSF-fitting photometry. Secondary counterparts are italicized.

Definition	RA and Dec (J2000)	HAWK-I		MAD		FLAMES?
		J	K_s	H	K_s	
Definite	05:38:39.24 −69:05:52.3	-	-	15.13	14.71	Yes
Definite	05:38:53.88 −69:09:31.3	-	14.59	-	-	No
Definite	05:38:05.64 −69:09:09.6	14.88	13.10	-	-	No
		17.74	*16.61*	-	-	
Definite	05:38:15.24 −69:06:54.5	-	-	-	-	No
Definite	05:38:33.09 −69:06:11.8	18.65	15.01	-	-	No
Definite	05:38:34.77 −69:06:06.1	-	-	-	-	Yes
Definite	05:38:39.69 −69:05:38.1	-	13.79	17.12	13.75	No
		-	*14.40*	*14.56*	*14.40*	Yes
Definite	05:38:45.15 −69:05:07.9	-	14.32	14.44	14.31	
Definite	05:38:31.62 −69:02:11.0	-	-	-	-	No
Definite	05:38:48.17 −69:04:11.7	15.39	-	-	-	No
Definite	05:38:49.27 −69:04:44.4	-	-	-	-	No
Definite	05:38:52.67 −69:04:37.5	16.67	13.67	-	-	No
Definite	05:38:58.42 −69:04:34.7	15.35	14.95	-	-	Yes
Definite	05:38:56.48 −69:04:17.0	-	16.01	-	-	No
		19.39	*15.55*	-	-	
		-	*15.61*	-	-	
		-	*16.72*	-	-	
Definite	05:39:04.42 −69:04:13.9	17.28	16.35	-	-	No
Probable	05:38:48.86 −69:08:28.0	15.73	15.57	-	-	Yes
Probable	05:38:21.10 −69:06:17.2	14.74	15.28	-	-	Yes
		15.92	*15.86*	-	-	Yes
		16.51	*15.59*	-	-	
Probable	05:38:22.44 −69:06:44.4	-	16.92	-	-	No
Probable	05:38:27.39 −69:08:09.0	15.62	15.54	-	-	Yes
Probable	05:38:38.46 −69:04:18.3	15.36	15.18	-	-	No

Continued on next page...

Table 4.2: GR09 YSO candidates with N-IR counterparts in the HAWK-I and MAD images (continued).

Definition	RA and Dec (J2000)	HAWK-I		MAD		FLAMES?
		J	K_s	H	K_s	
Probable	05:38:41.23 −69:02:59.0	13.89	13.64	-	-	Yes
Probable	05:38:34.06 −69:04:52.2	18.84	14.27	-	-	No
Probable	05:38:55.56 −69:04:26.5	13.56	12.47	-	-	Yes
		18.45	*17.10*	-	-	
Possible	05:38:44.32 −69:03:29.9	16.28	15.38	-	-	No
Possible	05:38:43.52 −69:06:29.0	-	-	18.16	17.15	No
		-	-	*17.05*	*16.87*	

4.3.1 VLT-FLAMES Tarantula Survey

Ten stars related to the YSO candidates in the HAWK-I imaging have been observed by the Tarantula Survey, recently carried out by the Fibre Large Array Multi Element Spectrograph (FLAMES). FLAMES is an multi-object, intermediate and high resolution fibre facility, covering a 25’ FoV on the VLT (Pasquini et al., 2002). The Tarantula Survey has obtained multi-epoch spectra of over 1000 stars in 30 Dor (Evans et al., 2010) using the GIRAFFE spectragraph. Three spectral ranges were observed, with a minimum of six epochs for LR02, and three for LR03 (see Table 4.3 for equivalent spectral ranges). Five LR02 observations were carried out within six months, with a sixth epoch taken six months later. LR03 observations were taken “back-to-back”, generally over a couple of days. One of the main motivations for the survey was to gain an understanding of the binary fraction within 30 Dor, hence the multi-epoch strategy.

The spectra have been used to classify the related counterparts and, if possible, to measure stellar and gas dynamics near the YSO regions. Radial gas velocities were calculated from Doppler shifted [OIII] nebular emission lines (4958.91 & 5006.84Å).

Table 4.3: Summary of FLAMES-GIRAFFE observations (Evans et al., 2010).

GIRAFFE setting	λ-coverage (Å)	R	Exposures
LR02	3980-4535	6500	6×(2×1815s)
LR03	4505-5050	7500	3×(2×1815s)
LR02	6470-6790	17000	2×(2×2265s)

Comparison of the gas and stellar dynamics informs whether the nebulosity and YSO are associated with each other. Spectra at different epochs allows detection of binary systems, while for spectra of single objects (or single-lined binaries) spectral classification was possible. These spectra are referred to in the following discussion of individual sources where appropriate.

A montage of the spectra is shown in Figures 4.9 & 4.10 (in which a cut has been applied to the data to remove the high-flux emission lines). The data have also been smoothed with a boxcar average over five pixels. Spectra have been shifted in flux to accommodate multiple spectra per plot.

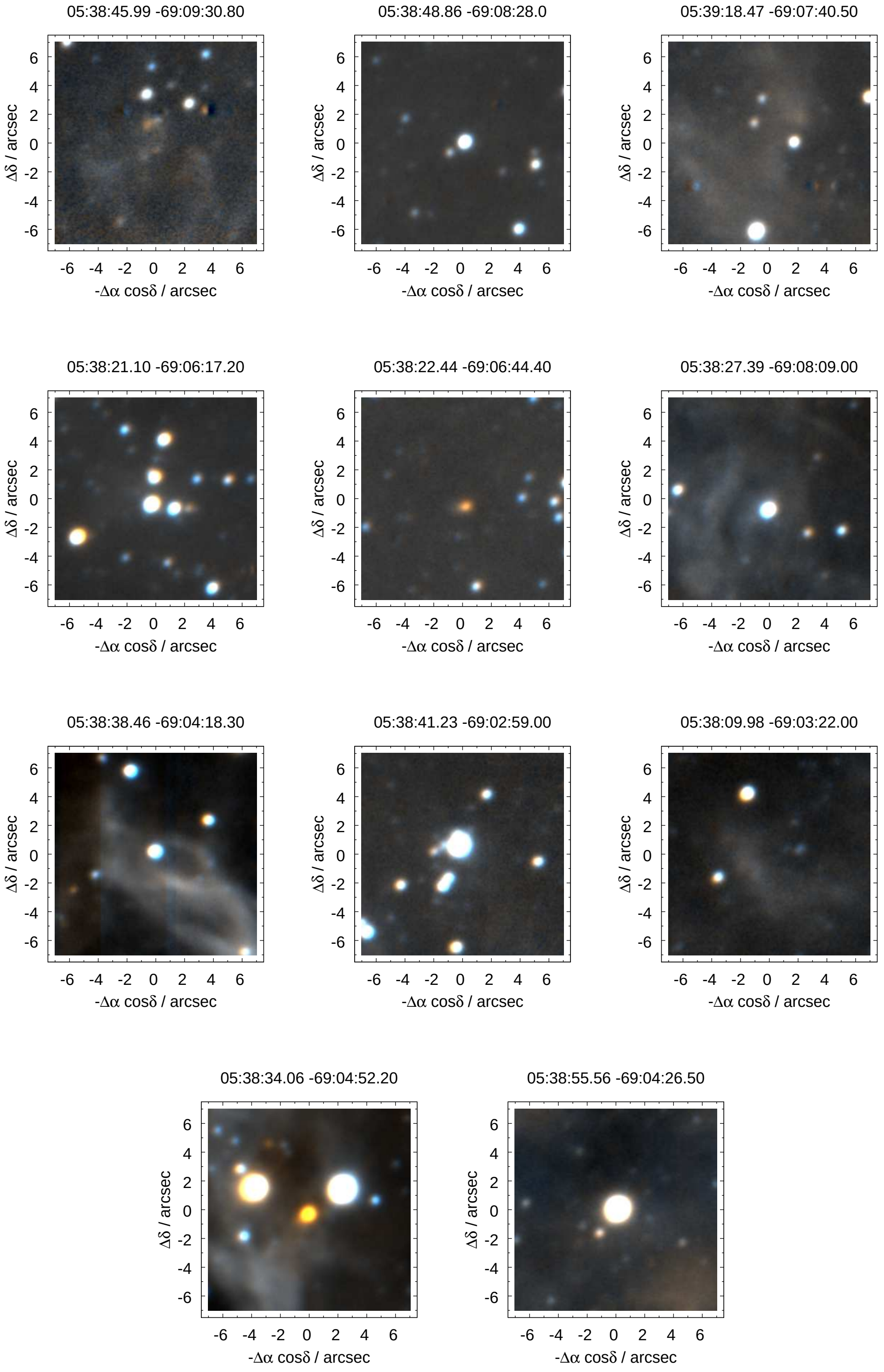

Figure 4.6: False colour HAWK-I images of “probable” YSO candidates from Gruendl & Chu (2009).

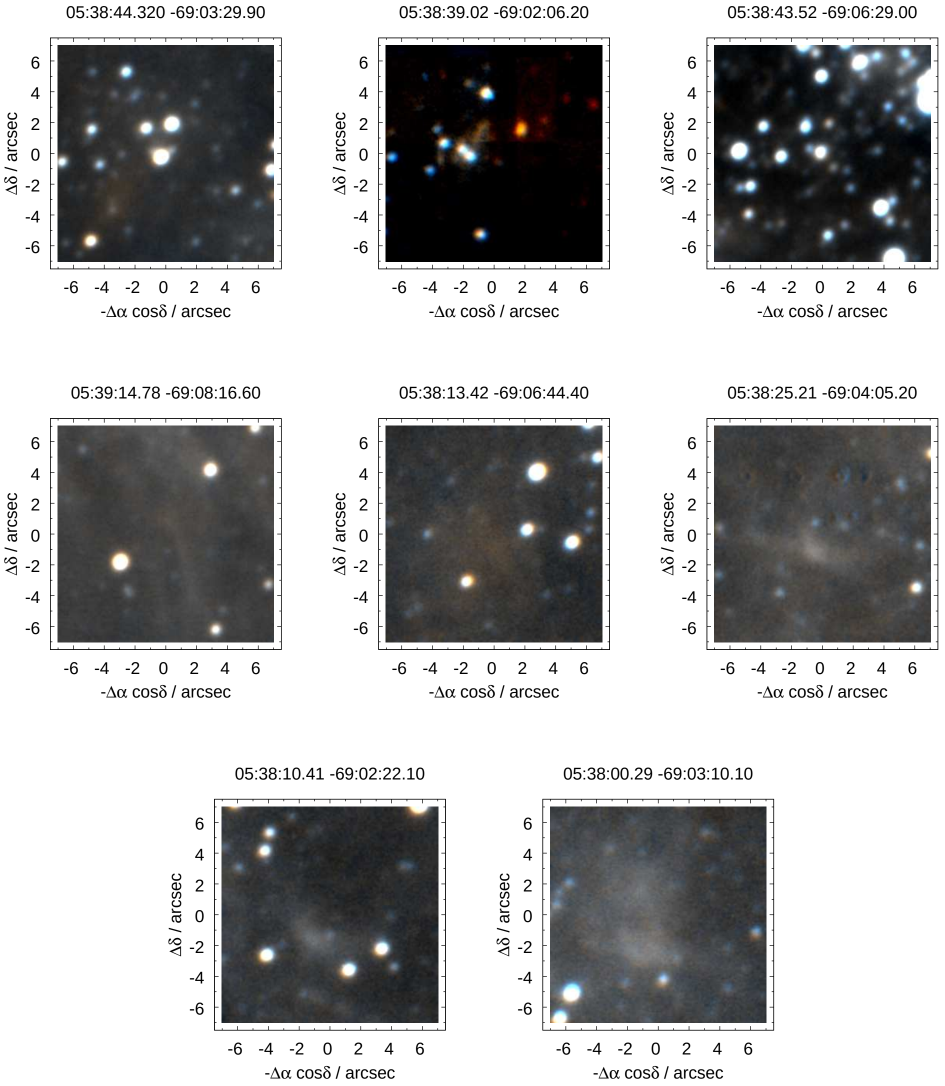

Figure 4.7: False colour HAWK-I images of "possible" YSO candidates from Gruendl & Chu (2009).

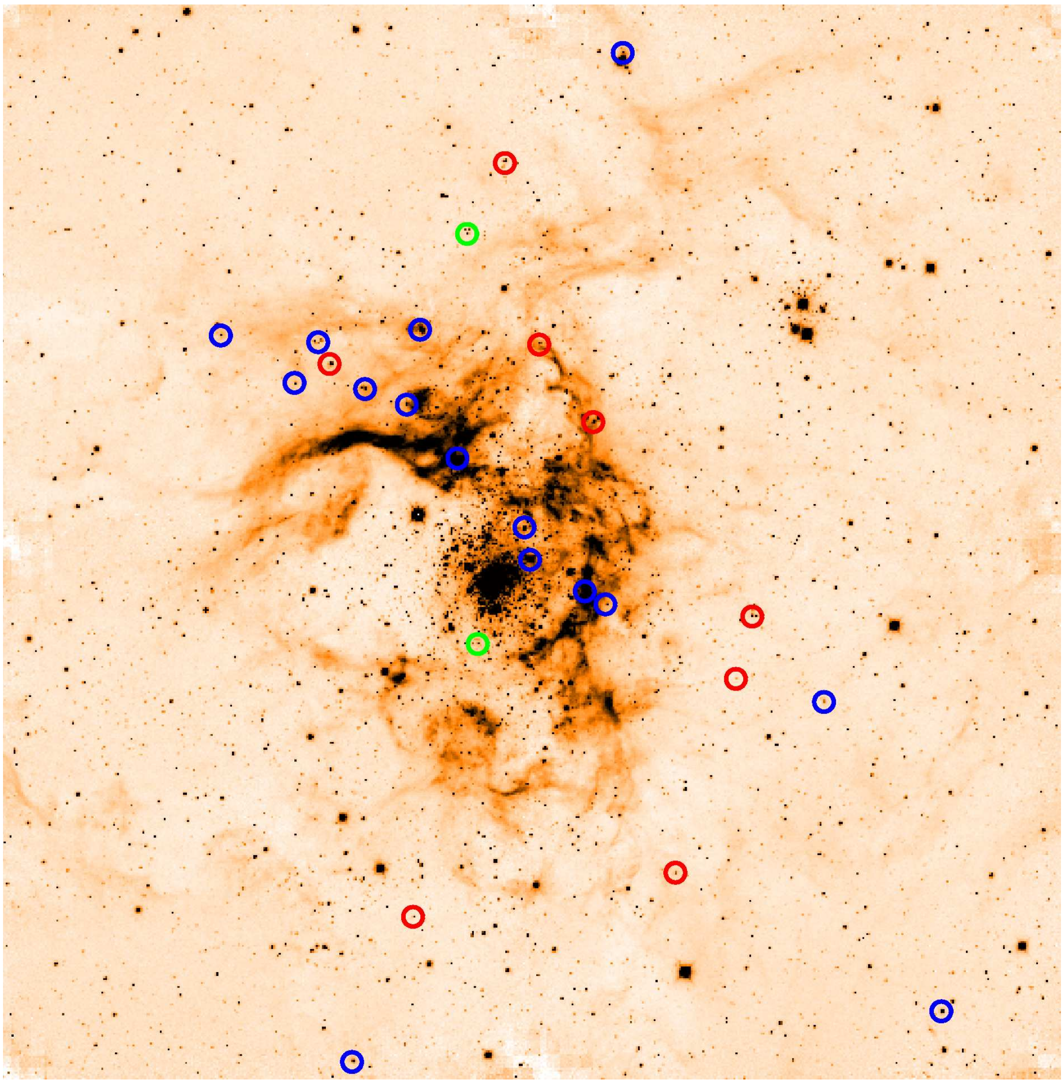

Figure 4.8: YSO candidates from Gruendl & Chu (2009) with N-IR counterparts overplotted on the combined HAWK-I K_s-band mosaic. *Blue*: GR09 "definite" YSOs, *red*: GR09 "probable" YSOs, *green*: GR09 "possible" YSOs.

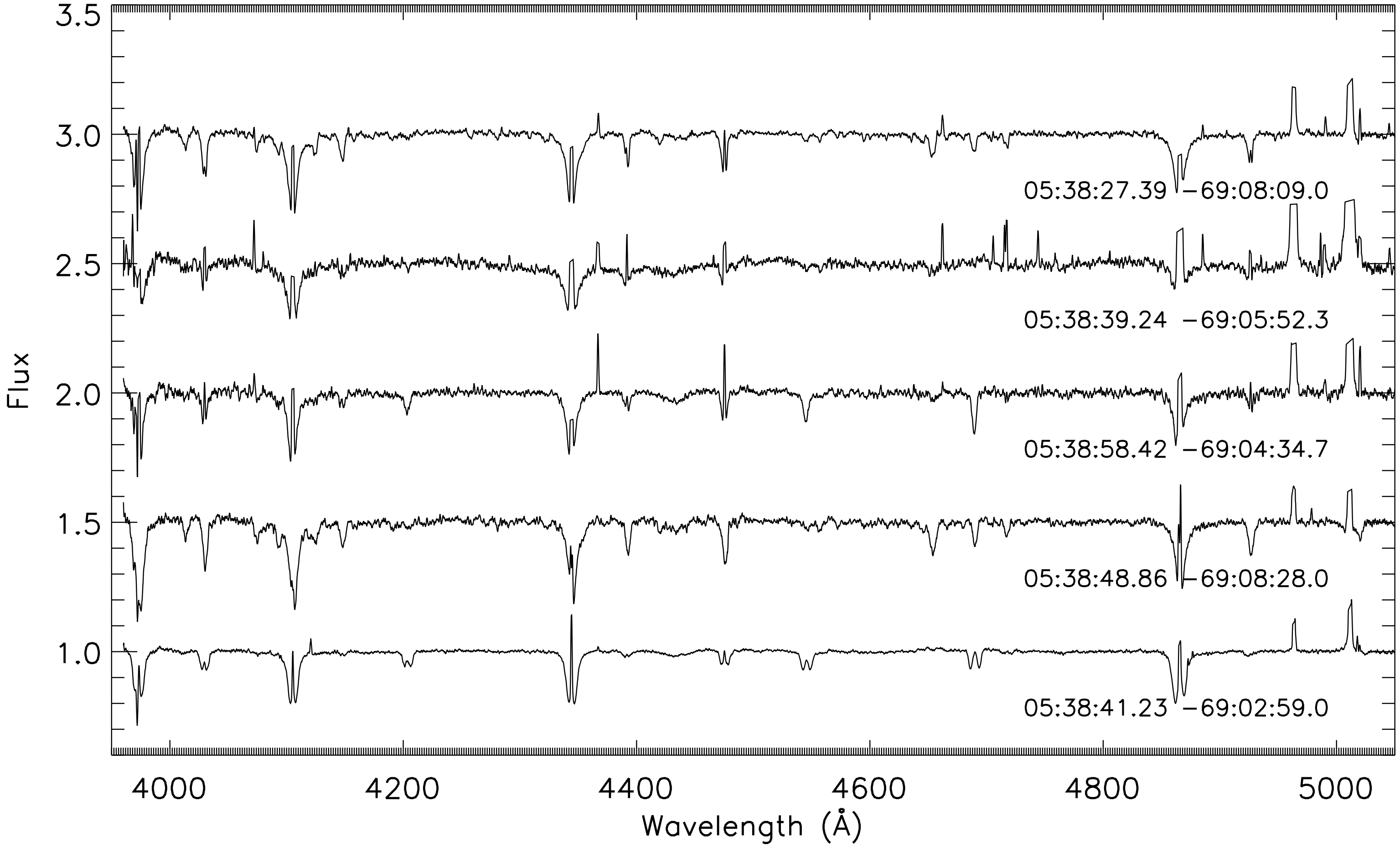

Figure 4.9: FLAMES spectra of the YSO candidates from Gruendl & Chu (2009).

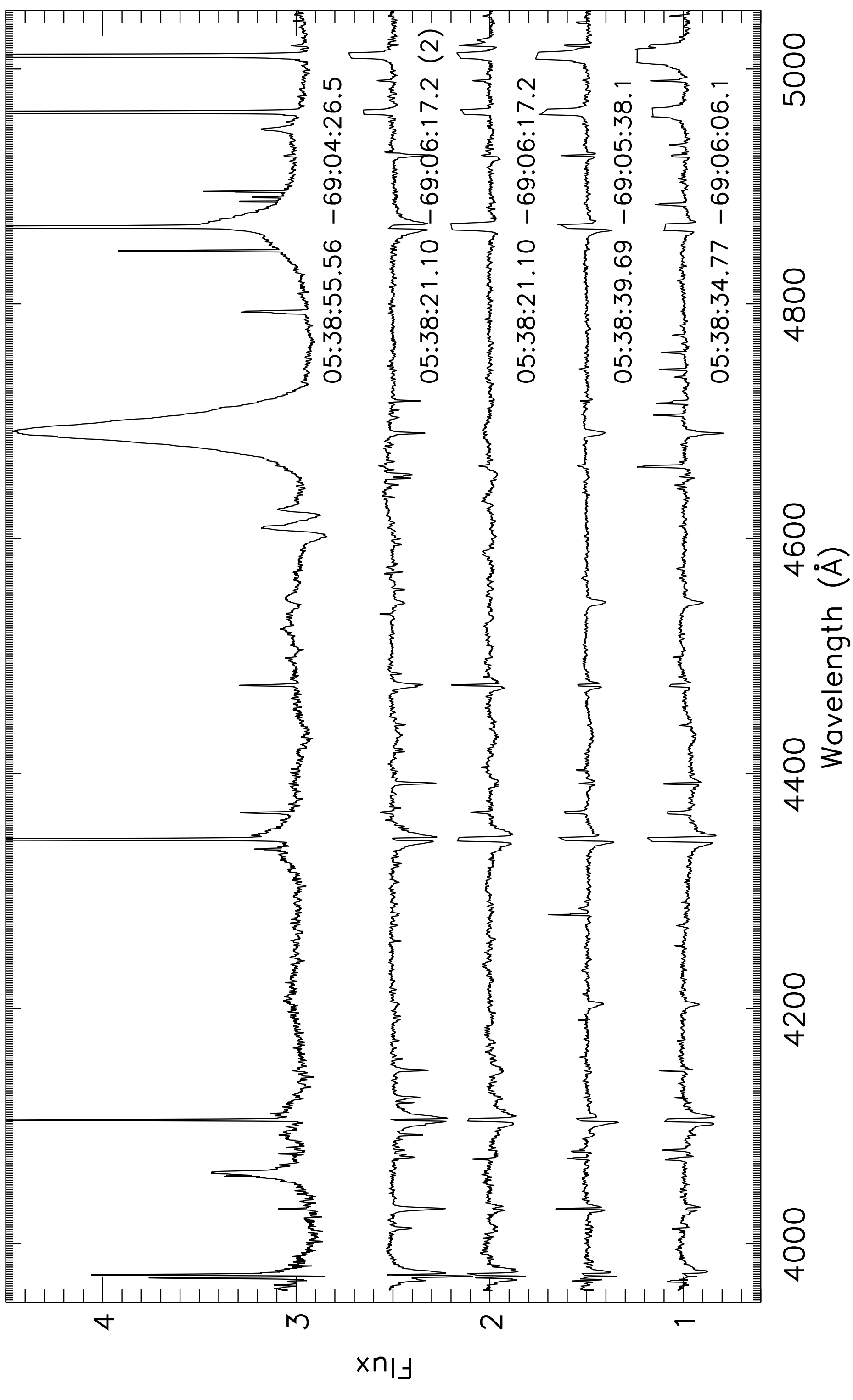

Figure 4.10: FLAMES spectra of the YSO candidates from Gruendl & Chu (2009). 05:38:21.10 −69:06:17.2 (2) is the object to the west of the GR09 object.

4.4 Discussion of Individual YSOs

4.4.1 “Definite” YSO candidates

Inspection of the Hawk-I and MAD frames shows ’gas’ within the frames. It is possible that this is reflection nebulosity from gas. For most of the “definite” detections there is either FLAMES spectra confirming the nebulosity being associated with the object, or CO emission from the region suggesting star formation. For the rest of the “definite” detections, due to the regions being extensive star forming regions, it is likely that it is gas associated with the objects, not reflection from dust in the background.

05:38:39.24 −69:05:52.3

Observed in both the HAWK-I and MAD frames, the YSO counterpart in the MAD images has $K_s = 14.71$ and $H-K_s = 0.42$, with another object separated by $\sim 0\farcs33$ (see Figure 4.11). Particularly striking is the apparent bow-shock, most easily seen in the K_s-band. This is almost, but not quite, aligned with the core of R136 approximately $19\farcs5$ away. Also of note in the same direction is R134/Brey 75 (Breysacher, 1981), classified as WN6(h) by Crowther & Smith (1997), at a distance of only $8''$.

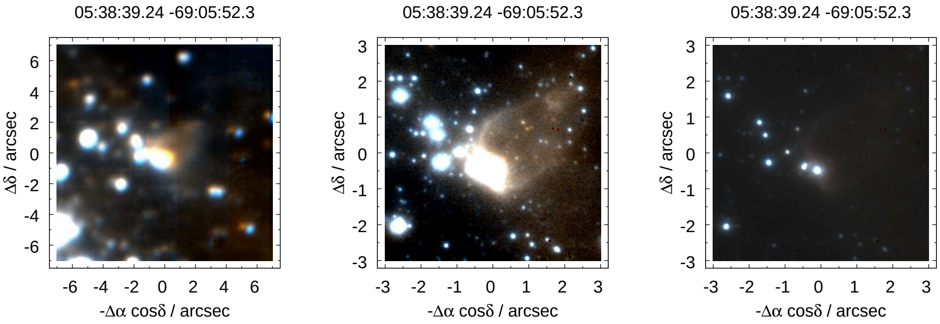

Figure 4.11: 05:38:39.24 −69:05:52.3. *Left*: HAWK-I false colour image, *centre*: MAD false colour image, *right*: MAD false colour image with lower contrast to resolve the two central components.

The FLAMES spectrum is shown in Figure 4.9 . The FLAMES spectra are swamped with nebular emission preventing stellar radial velocity measurements, but the [OIII] emission lines suggest a gas radial velocity of 260kms^{-1}, consistent with this part of the LMC (Bosch et al., 2009). Note that the FLAMES fibres are $1\overset{''}{.}2$ on the sky, so will include flux from both the central sources (but will be dominated by the brighter object). However, He I lines are visible within the FLAMES spectrum, without stray He II lines, indicating a star of classification B0-B1, which have typical main-sequence masses of around 12-15M$_\odot$ (Trundle et al., 2007).

05:38:53.88 −69:09:31.3

An isolated, seemingly singular object in the HAWK-I images, with K_S=14.59, compared to K_S=14.13 (and H-K_S=0.81) from 2MASS (which likely includes a contribution from the extended gas emission). From observations of CO gas, Kim et al. (2007) also report a YSO at this position, classifying it as in the intermediate stage of being surrounded by an infalling envelope and having an accretion disc. The K_S-band HAWK-I image clearly highlights the gas enshrouding it, with a gas cloud extending to the north-east for $2\overset{''}{.}8$. *Spitzer* spectroscopy of the YSO from Seale et al. (2009) finds PAH emission and fine-structure lines.

05:38:05.64 −69:09:09.0

The *Spitzer* position is offset $1\overset{''}{.}67$ from the location of a relatively bright source in the HAWK-I images (K_S=13.10). Another object is also present $\sim1\overset{''}{.}1$ from the brighter source (K_S=16.62 and $J-K_\mathrm{S}$=1.13). Visual inspection of the HAWK-I K_S-band frames suggests there is either another companion not fully resolved, or gas protruding from the object. From their CO observations, Kim et al. (2007) classify it as surrounded by an in-falling envelope.

05:38:15.24 −69:06:54.5

Appears as a single object within the HAWK-I images, but is slightly embedded such that it was rejected by the PSF fitting selection criteria. Aperture photometry provides K_s=16.01.

05:38:33.09 −69:06:11.8

The HAWK-I photometry for this source gives K_s=15.01 and J-K_s=3.64, in excellent agreement with the *HST* values from Brandner et al. (2001) (K_s=15.09 and $J-K_s$=3.59). The YSO lies near a large ionised region, although there is a void to the south-west which could be colder gas blocking light from stars embedded or behind. VA09 describe it as a YSO in a dark cloud with no optical counterpart and classify it as a Type I YSO.

05:38:34.77 −69:06:06.1

The *Spitzer* position is located within a dense gas knot, with a bright object $1.''31$ away which has not been detected through PSF fitting within the HAWK-I data, most likely due to the contribution from the gas. This object is Parker 409, classified by Walborn & Blades (1997) as an O3-6V type star, while Rubio et al. (1998) attribute magnitudes of K_s=14.29 and $J-K_s$=0.68, recognising it as an embedded early O type star. The multi-epoch FLAMES spectra (see Figure 4.10) reveal the star to be a single, with a radial velocity of $\sim$275kms^{-1} (matched to the gas velocity).

05:38:39.69 −69:05:38.1

This object appears as a somewhat extended or embedded source in the H-band MAD image (Figure 4.12), with $K_s = 13.75$ and $H-K_s = 3.37$. This source corresponds to IRSW-127 from Rubio et al. (1998), for which they found $K_s = 13.91$ and $H-K_s = 2.85$.

The bright star $1.''2$ to the south is Parker 733, for which $K_s = 14.40$ and $H-K_s = 0.16$, suggesting that this is a massive star. The He II and (strongly contaminated) He I lines

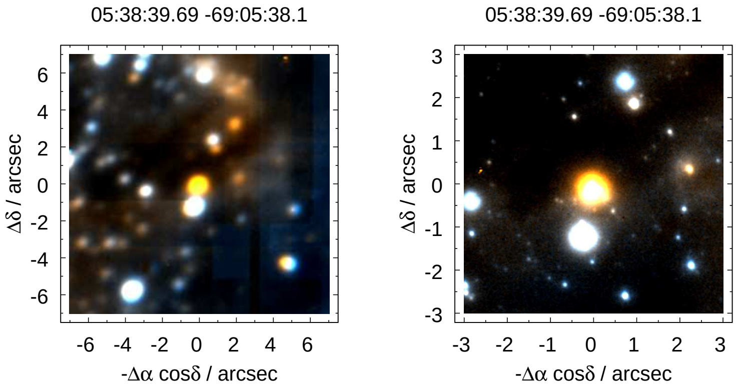

Figure 4.12: 05:38:39.69 −69:05:38.1. *Left*: HAWK-I false colour image, *right*: MAD false colour image.

from the FLAMES spectrum (see Figure 4.10) confirm that it is a mid O-type star. No variations are seen in the stellar radial velocities ($\sim$280kms^{-1}) which are matched to the gas velocities. The strong contrast in the colours of the two stars is immediately obvious from the composite-colour images in Figure 4.12.

05:38:45.15 −69:05:07.9

The GR09 position is approximately $0\overset{\prime\prime}{.}4$ north of P1222/S116/IRSN-101 (Parker, 1993; Selman et al., 1998; Rubio et al., 1998), which was classified as O3-6 V by Walborn & Blades (1997) from ground-based spectroscopy, later revised to O9 V(n)p by Walborn et al. (2002) from *HST* observations. Images of the region from both HAWK-I and MAD are shown in Figure 4.13.

This source lies within the dense nebular region referred to as ‘Knot 1’ by Walborn (1986), highlighted as young massive stars just emerging from their natal cocoons and imaged at optical and near-IR wavelengths with *HST* by Walborn et al. (1999, 2002). The relatively bright *Spitzer* magnitudes quoted by GR09 are in keeping with Parker 1222 as the most plausible counterpart. Indeed, the spectral energy distribution shown in Figure 13 of GR09 reveals increased magnitudes bluewards of 1 μm, as well as

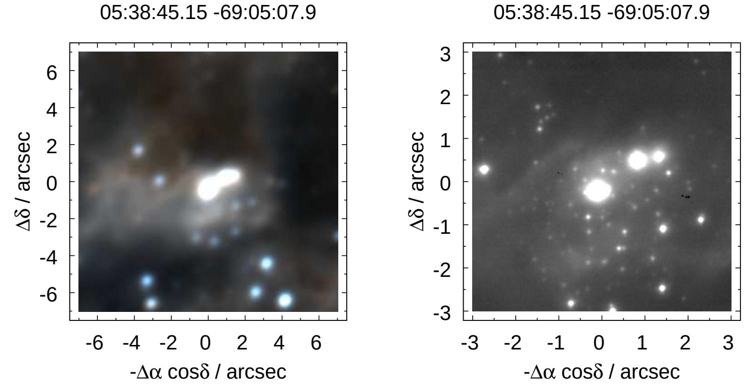

Figure 4.13: 05:38:45.15 −69:05:07.9. *Left*: HAWK-I false colour image, *right*: MAD *H*-band image.

redwards, consistent with a massive star with an IR excess. From the MAD images we find $K_{\rm s} = 14.31$ and $H - K_{\rm s} = 0.13$, as compared to $K_{\rm s} = 14.45$ and $H - K_{\rm s} = 0.03$ from the *HST*-NICMOS observations of Knot 1 by Brandner et al. (2001).

VA09 note the source as residing in a resolved H II region and, on the basis of the Hα luminosity (uncorrected for extinction), provide a lower bound on the inferred spectral type of the YSO of B0.5; evidently from the classification of Walborn & Blades, the star is slightly hotter.

05:38:31.62 −69:02:14.6

Appears as a single object in the HAWK-I frames, but is heavily embedded in gas so does not have $K_{\rm s}$ or *J*-band PSF-fitting photometry available. Its is possible that with higher resolution images the source will be resolved into multiple components. Other sources are visible within the cocoon of gas, even with the resolution of HAWK-I.

05:38:48.17 −69:04:11.7

Appears as a host of objects enshrouded in gas within the HAWK-I frame with only the brightest, central source detected by the PSF-fitting routines (only in the *J*-band, with J=15.39). Maercker & Burton (2005) obtained a comparable value of J=15.2 (with K_s=12.0).

Determined as a Type I YSO by VA09, in a dark cloud in the Hα images and with no counterpart object in the optical. This is consistent with the HAWK-I image.

05:38:49.27 −69:04:44.4

This red source is situated just to the west of a group of stars heavily embedded in gas. The object is not detected by the PSF-fitting, although there are two much fainter objects detected in the K_s-band images (K_s=18.92 & 17.84) at distances of $1\overset{\prime\prime}{.}93$ and $1\overset{\prime\prime}{.}78$. The main object is detected by 2MASS $0\overset{\prime\prime}{.}33$ away from the *Spitzer* location, with K_s=14.07.

VA09 describe it as a dark cloud without an optical counterpart and classify it as Type I, with the *Spitzer* spectrum from Seale et al. (2009) showing silicate absorption and PAH emission at 5-13μm.

05:38:52.67 −69:04:37.5

This object is very red with HAWK-I values of K_s=13.67 and $J-K_s$=3.00, with comparable photometry from both 2MASS and Maercker & Burton (2005). A second source is just under 2" away and also appears very red.

There appears to be gas in close proximity, with VA09 describing it as a TypeII/III YSO in a dark cloud with no optical counterpart. *Spitzer* spectroscopy by Seale et al. (2009) find it exhibits no silicate emission, but does have PAH emission between 5-13μm.

05:38:58.42 −69:04:34.7

Appears as an isolated object within the HAWK-I frames, with K_s=14.95 and $J-K_s$=0.40, with an apparently associated gas feature protruding from the source. VA09 describe it as being a type III YSO in an unresolved HII region, and *Spitzer* spectroscopy from Seale et al. (2009) finds no silicate emission, but PAH emission from 5-13μm. The

FLAMES spectra indicate it is a mid O-type single-lined binary (e.g. the He II 4542 line in Figure 4.14). There is a large amplitude in the range of measured radial velocities (see Figure 4.15), with the systemic velocity likely comparable to the gas velocity (260kms^{-1}; dashed line in Figure 4.15).

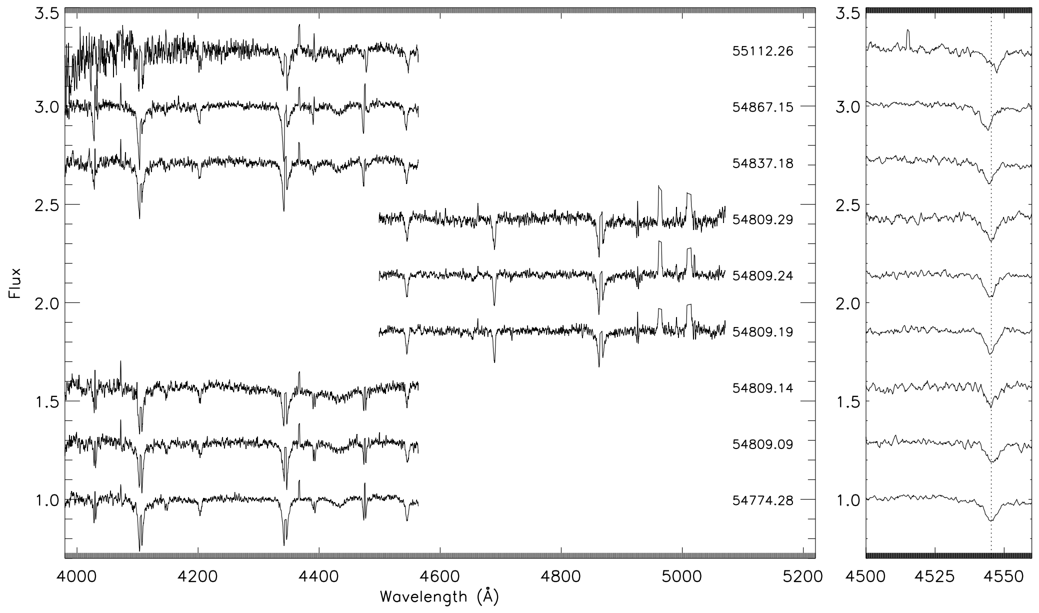

Figure 4.14: Spectra of 05:38:58.42 −69:04:34.7

05:38:56.48 −69:04:17.0

Perhaps a small association of YSOs, the GR09 object has at least four objects within a distance of ∼0.″6 from the *Spitzer* position, which has K_S=16.01 (central), 15.61 (west), 16.72 (further west), and 15.55 (east).

05:39:04.42 −69:04:13.9

Detected as an isolated object with K_S=16.35 and $J-K_S$=0.93, slightly surrounded by gas, *Spitzer* spectroscopy from Seale et al. (2009) find it does not have silicate absorption, but does have PAH emission from 5-13μm.

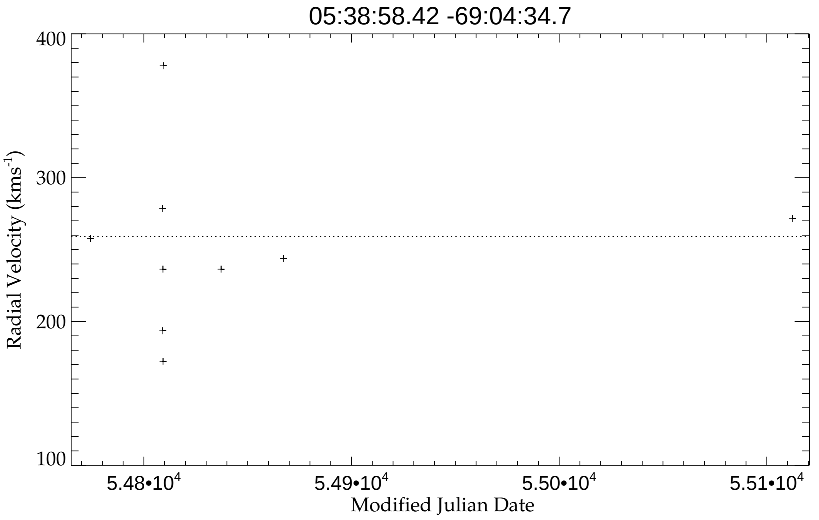

Figure 4.15: Radial velocity measurements of 05:38:58.42 −69:04:34.7. The dotted line is the radial velocity of the [OIII] nebular emission superimposed on the stellar spectrum.

4.4.2 "Probable" YSO candidates

As for the "definite" YSO detections, gas emission or reflection nebulosity from dust can be observed within some of the frames. Again, where FLAMES spectra or CO emission is available, it is clear that it is gas related to the object. Where these are not available, and due to the uncertainty of some of the objects, it is possible that it is reflection nebular, not related to the object in question.

05:38:48.86 −69:08:28.0

GR09 noted this object could be a normal star with excess IR emission. There are two objects visible within the HAWK-I frames, with the brighter object (located at the location of the *Spitzer* source) having K_S=15.57 and $J-K_S$=0.16.

From past spectroscopy, a spectral type of O9.5II has been assigned by Bosch et al. (2001) and also O9/B0II by Walborn & Blades (1997). The new FLAMES spectra for the object indicates it is a single-lined binary (see Figure 4.16), with radial velocities shown in Figure 4.17. The nebular emission lines exhibit two radial velocity components, perhaps indicating an expanding shell of gas.

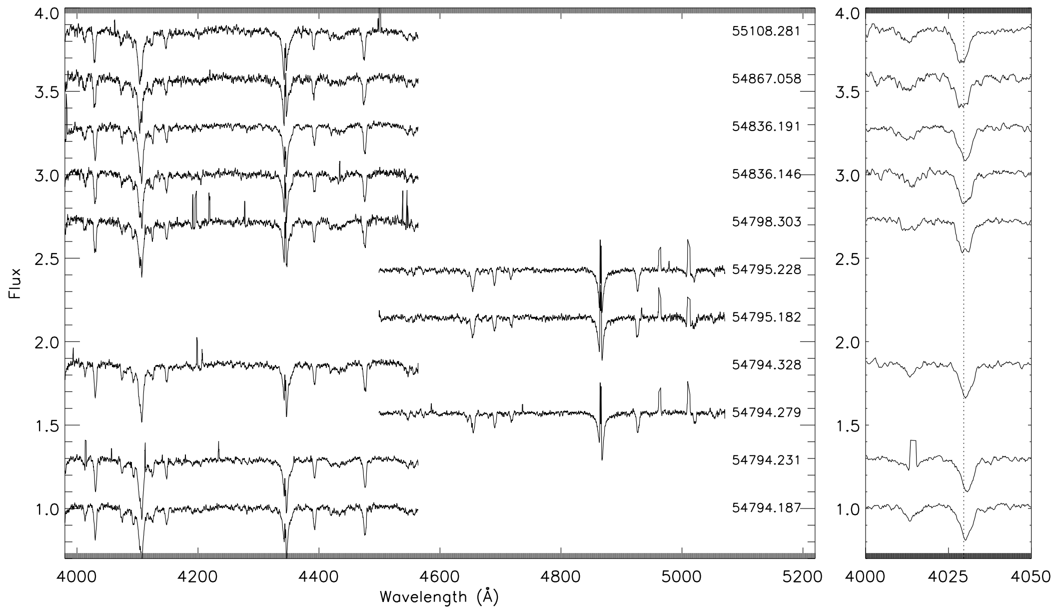

Figure 4.16: Spectra of 05:38:48.86 −69:08:28.0. *Left*: Full spectral range, labelled by Modified Julian Date of observations. *Right*: Doppler shifts of the He I (λ=4025.61) line caused by binary orbit.

05:38:21.10 −69:06:17.2

There are multiple objects detected around the *Spitzer* location. The central object has K_S=14.74 and $J-K_S$=0.54 in the HAWK-I images. The object to the north has K_S=15.59 and $J-K_S$=0.92 and the object to the west has K_S=15.86 and $J-K_S$=0.16. An object is detected in 2MASS (although the objects are likely unresolved in the 2MASS detections) with K_S=15.29 and $J-K_S$=0.39.

The FLAMES spectrum of the GR09 source shows the gas in the region is associated with the object as both have a radial velocities of $\sim$250kms^{-1}. The object is classified as a Be-type star (see Figure 4.10). The FLAMES spectrum of the object to the west has a radial velocity of $\sim$285kms^{-1}, a gas radial velocity of $\sim$265kms^{-1}, and is classified as type B0V (see Figure 4.10).

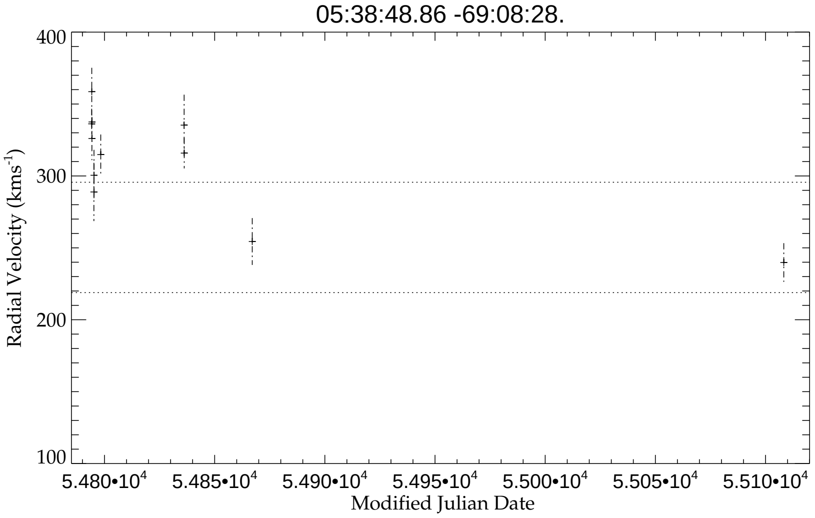

Figure 4.17: Mean radial velocities for each epoch for 05:38:48.86 −69:08:28.0. Also shown are the two radial velocity [OIII] components (dotted lines) superimposed on the stellar spectrum.

05:38:22.44 −69:06:44.4

A detected HAWK-I object is 0.″19 from the *Spitzer* position, with an asymmetric PSF suggesting it could be surrounded by gas. The object is red, with K_S=16.92, somewhat fainter than the other counterparts, suggesting it as a lower-mass YSO.

05:38:27.39 −69:08:09.0

Both bands in the HAWK-I data show an object distorted by gas at a location of 0.″49 away from *Spitzer* position, with K_S=15.54 and $J-K_S$=0.08. An object 0.″43 from the *Spitzer* location is also in the 2MASS catalogue, with J=15.22, H=15.20, and K_S=14.10. The K_S value differs greatly from the HAWK-I K_S value, however the quality flag for 2MASS in the K_S-band was '*U*'.

The star is Parker 103, classified as B0V by Bosch et al. (2001). The FLAMES spectrum (Figure 4.9) confirms the previous specification, and indicated that the gas and object are associated, with radial velocities of $\sim$290kms^{-1}.

05:38:38.46 −69:04:18.3

Situated at the edge of the HAWK-I detector, bright ionised regions surround the object. The HAWK-I images record K_s=15.18 and $J-K_s$=0.18, at a distance of $1\overset{\prime\prime}{.}22$ from the *Spitzer* location. The star is Parker 649, classified by Bosch et al. (2001) as O8-9V.

05:38:41.23 −69:02:59.0

From inspection of the HAWK-I frames, there are four objects detected around the *Spitzer* location, although it is unclear if one of the detections is a star or a dense, heated filament associated with the brightest object, for which HAWK-I gives K_s=13.64 and $J-K_s$=0.25. The other objects have K_s magnitudes of 16.5-17.5$^{\rm m}$. The bright star (Parker 861) was classified as O7V by Bosch et al. (1999). Kim et al. (2007) also identified the star as a YSO surrounded by an infalling envelope. This is backed-up by Townsley et al. (2006) who detect it as an x-ray source, possibly caused by material accreting onto the object.

The FLAMES data reveals the bright star is a double-lined binary, with roughly similar, mid-O spectral types (see Figure 4.18).

05:38:34.06 −69:04:52.2

A very red object is detected $1\overset{\prime\prime}{.}3$ from the *Spitzer* position, with K_s=14.27 and $J-K_s$=4.57 and there are also two bright stars nearby. VA09 detect a Type I YSO in a dark cloud (in the Hα) with no optical counterpart.

05:38:55.56 −69:04:26.5

The HAWK-I counterpart has K_s=12.47 and $J-K_s$=1.10 (compared to K_s=12.66 and $J-K_s$=1.07 from 2MASS). VA09 detect it in an unresolved HII region and classify it as a Type III YSO. The FLAMES data have revealed this star as a new, previously unknown, Wolf-Rayet star (see Figure 4.10) , classified as WN5h [Evans et al. in preparation].

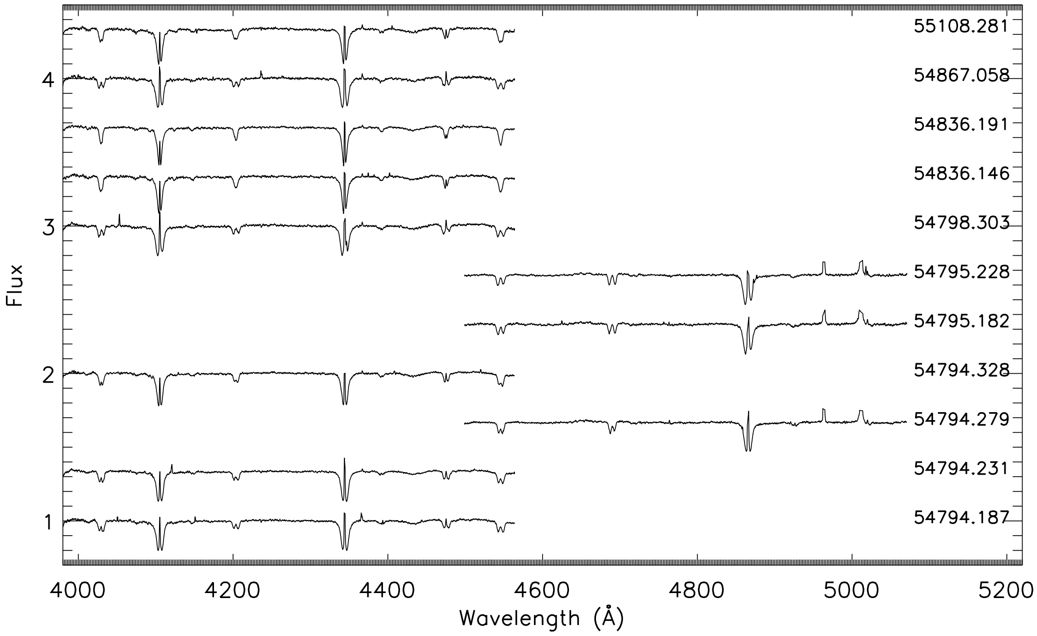

Figure 4.18: Spectra of 05:38:41.23 -69:02:59.0. *Right*: Modified Julian Date of observations labelled down the right-hand side.

4.4.3 "Possible" YSO candidate

05:38:44.32 −69:03:29.90

This object appears to have gas associated, although, without FLAMES spectra it is impossible to determine if this is emission and not reflection nebulosity from dust in the background. Photometric values of K_S=15.38 and $J-K_S$=0.90 were measured, suggesting it could be a class III YSO. Two other objects are ∼2" away, with K_S=16.57 and $J-K_S$=0.62, and K_S=15.70 and $J-K_S$=0.57.

05:38:43.52 −69:06:29.00

Appearing as a single object in the HAWK-I images, the MAD data resolves two objects (see Figure 4.19). The red, suspected GR09 object has $K_S = 17.15$ and $H-K_S = 1.01$. The adjacent object ($0\farcs25$ to the northeast) is Parker 1064, with $K_S = 16.87$ and $H-K_S = 0.18$, for which the spectral type is unknown. VA09 note this source as being in a dark cloud and as comprising multiple YSOs in the *Spitzer* PSF, one with an optical counterpart in the Hα *HST* images, and one without; the MAD imaging substantiates this claim.

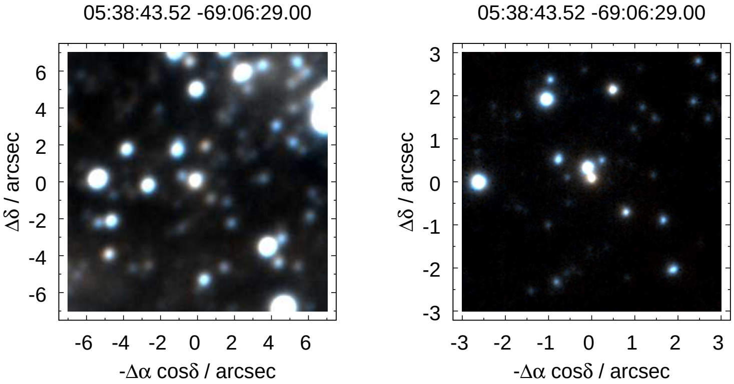

Figure 4.19: 05:38:43.52 −69:06:29.00. *Left*: HAWK-I false colour image, *right*: MAD false colour image.

4.5 Discussion

The YSO candidates can be summarised as two varieties. There are the OB-type stars which appear to have already joined the main sequence, and the (presumably) early-phase, red sources. The spectral classes of the OB-type stars indicate that they have masses of 9$M_\odot$ and above. For instance, comparing a K_s=16.35 star (the faintest OB-type counterpart detected) with the ischrone overplotted in Figure 2.17, arrives at a mass estimate of $\sim$16$M_\odot$. Gaining mass estimates for the redder objects will involve fitting pre-main sequence evolutionary tracks and will be carried out in the future.

It would be intriguing to know the source of the IR excess for the OB-type stars. It is likely a remnant of the natal cloud in the final stages of being dispersed, but perhaps we are observing Oe/Be stars and the excess is from a disc of material expelled from the star. The fact that one of the counterpart spectra looks like a Be-type star

(05:38:21.10 −69:06:17.2) adds credence to this idea. It is also possible that for some of the sources, the IR excess is the result of unresolved sources. The “possible” YSO located at 05:38:27.39 −69:08:09.0 is a good example of this. When observed at the seeing-limited resolution of HAWK-I the object appears as a singular blue source, however, the AO-assisted MAD images inform that there is also a reddish object at a small separation. Follow-up AO assisted imaging of the other HAWK-I YSOs would provide an estimate on the occurrence of such blending.

There is an over density of YSOs to the north and north-east of R136, near the bright ionised filament, where eight YSO candidates reside. This is the region referred to as being in the ’Orion Phase’ by Walborn & Blades (1997) where new star formation has been triggered by the ionising core. The YSOs in this region are mainly type III objects which have already joined the main-sequence. CO emission across 30 Dor has been mapped by Johansson et al. (1998), revealing good correlation when compared to the CO gas.

Of the eight OB-type stars which have FLAMES spectra, two of them are single-lined binaries and one is a double-lined binary. Light curves could be gained from long-term photometric data and a more focused spectroscopic follow-up will inform of the orbital parameters. Producing light-curves for the double-lined binary will also inform if the binary is an eclipsing system and, if so, it should be possible to gain a mass estimate.

4.5.1 Summary

Of the “possible” candidates investigated by the more lenient selection criteria of GR09, 75% were found to have no obvious counterparts within the HAWK-I and MAD frames. However, all of the “definite” and 8/11 of the “probable” sources did have promising counterparts. This suggests that the less stringent selection criteria of GR09 did result in a high YSO detection rate with little contamination.

The SAGE consortium are currently investigating probing the lower-mass YSOs in the LMC [Meixner, et al. private communication]. The lower mass YSOs occupy regions of the CMD shared with other populations. Probing the low-masses increases the likelihood of contamination from non-YSO sources. However, this study suggests that using the selection criterior used by GR09, accepting “definite” and “probable” objects will result in a catalogue with little contamination.

Chapter 5

CANARY

This chapter addresses the instrumentation side of my work. I have worked on several aspects of an MOAO demonstrator instrument, CANARY, to be installed on the 4.2m William Herschel Telescope (WHT) on La Palma. My involvement has concerned the telescope and atmospheric turbulence simulators.

5.1 CANARY Concept

The backdrop for CANARY is the anticipated next generation of large telescopes with diameters in the range of 25-42m, ELTs (see Section 1.1). The theoretical angular resolution of a telescope is inversely proportional to its diameter and so larger telescopes can resolve smaller separations. In practice the resolution of ground based telescopes is limited by the distortion effects of the atmosphere. This limit can be overcome with the use of AO (see Section 1.2). To make best use of the potentially large FoVs, ELT instruments must apply AO corrections over a large area. For fields of 1' or larger, we need to look at either MOAO or MCAO technologies for improved resolution and image quality.

CANARY is designed to demonstrate the feasibility of MOAO technology on-sky and is the precursor to the Extremely large telescope Adaptive optics for GaLaxy Evolution (EAGLE) instrument. EAGLE is a proposed N-IR multi-object spectrometer for the 42m E-ELT. The FoV will be 5 to 10', over which $\sim$20 Integral Field Units (IFUs) are deployed to gather 3-D spectroscopy (Cuby et al., 2009). It is necessary to employ MOAO technology for EAGLE as GLAO does not provide the required performance, and MCAO systems are impractical over such a large FoV. An MOAO system will use a combination of sodium LGS and NGS to calculate the turbulence at selected points across the FoV, with each IFU channel containing an individual DM, making corrections for that field only. The sodium LGS create beacons in the upper atmosphere ($\sim$100km) and the NGS correct for low-order effects occurring above this. EAGLE is an ambitious project, so the novelty of the MOAO technology warrants on-sky demonstration. The multiple channels of EAGLE use the same correction methods and so demonstration of only a single channel will provide evidence that the technique is feasible.

CANARY is a single channel MOAO demonstrator to be installed at the Nasmyth platform on WHT at the Roque de Los Muchachos Observatory on La Palma. The project is headed by Centre for Advanced Instrumentation (CfAI) at the University of Durham and is operating on a budget of $\sim$£2M. Collaborators include the UKATC and the Laboratoire d'études Spatiales et d'Instrumentation en Astrophysique (LESIA). Reaching the complexity of the EAGLE MOAO system is achieved through three phases (Morris et al., 2010):

- Phase A - Concentrates on wavefront sensing with three NGS and applying low-order corrections with an 8x8 actuator open-loop DM. On sky testing is planned for late 2010.

- Phase B - Four Rayleigh LGS are introduced, with wavefront sensing used for computing low-order corrections concurrently with the NGS. On sky testing is planned for 2011.

- Phase C - Combines high and low-order corrections by introducing the “woofer” and “tweeter” DM configuration proposed by EAGLE. The “woofer” DM attends to the low-order distortions, already tested in phase A and B. The “tweeter”

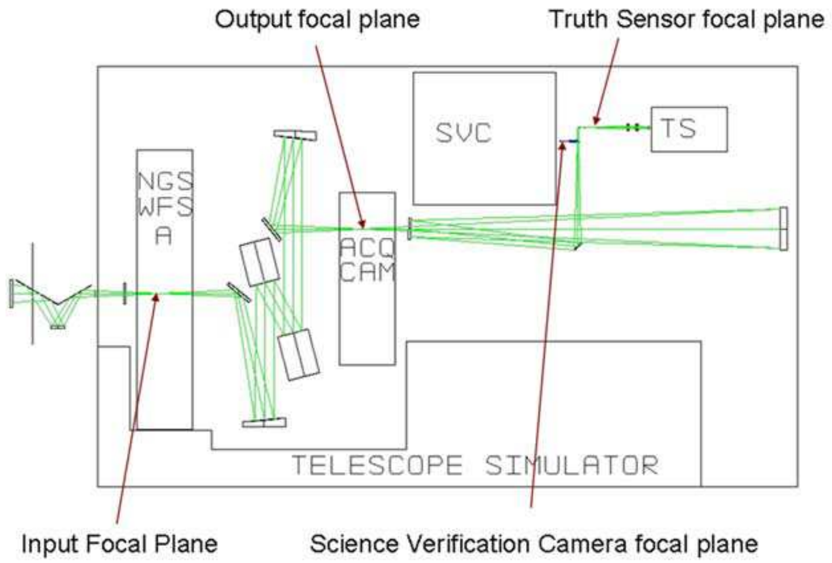

Figure 5.1: CANARY layout during phase A. ACQ CAM=Acquisition Camera. SVC=Science Verification Camera. TS=Truth Sensor. Courtesy of Morris et al. (2010).

DM will perform high-order corrections with 32x32 actuators. On sky testing is planned for 2012.

CANARY is designed to scale with EAGLE. CANARY will use Rayleigh LGS which operate at 1/10th the altitude of sodium LGS at ∼10km. With a primary aperture of 4.2m, WHT is therefore a 1:10 scale of the proposed E-ELT. Using Rayleigh LGS with a 1/10th scale telescope will imitate the focal anisoplanatism, (see Section 1.2.6) that will be experienced by an E-ELT with sodium LGS.

The optical layout for phase A is shown in Figure 5.1. Three NGS are located within a 2$'\!.$5 diameter of the input focal plane, observed by three SHWFS working in open-loop with the DM. The performance is monitored by a truth sensor imager and on-axis NGS. In practice, the truth sensor is a SHWFS, performing closed-loop corrections on the on-axis NGS. The performance of the whole system is very much dependent on the quality of the alignment. Simulations have shown that a pupil shear (where the pupil entrance is de-centred on the exit pupil) of 1/70th of a pupil can cause degradation in performance (Morris et al., 2010). A telescope simulator has been

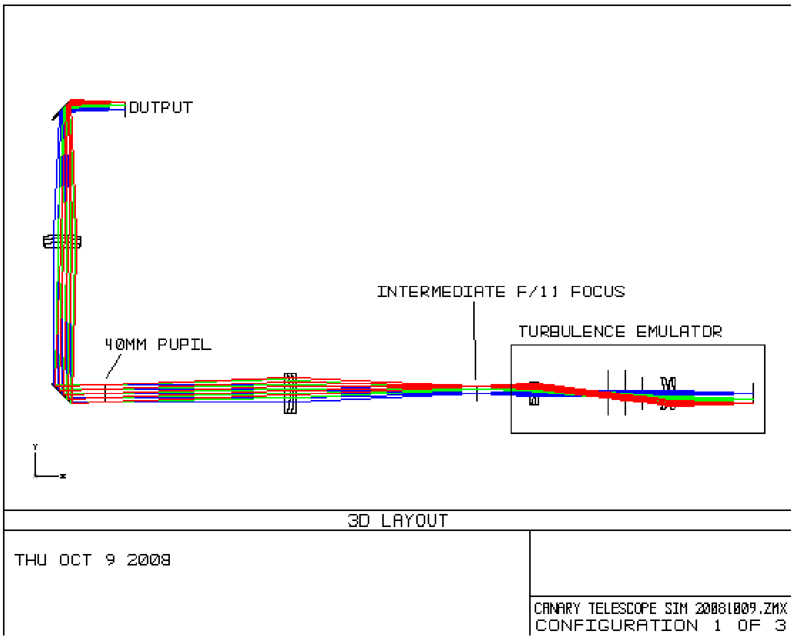

Figure 5.2: Telescope simulator layout. Image taken from CANARY design review, 2008.

used as the alignment reference during the laboratory set-up and will be used as the alignment reference at the telescope.

The UKATC has designed and constructed the telescope simulator and calibration unit, as well as the derotator for phase A. The telescope simulator contains a turbulence emulator and relay optics (see Figure 5.2). My work has concentrated on simulating and testing the telescope simulator. The turbulence emulator (in greater detail in Figure 5.3) contains the NGS and LGS simulation light sources. The NGS are attached to motors to allow the positioning of different asterisms. Although three NGS are required per asterism, there are four NGS to gain complete coverage of the FoV. Two NGS fibres are connected to the same motor stage (see Figure 5.4). There is also a central fibre with a N-IR source to simulate the on-axis science object. There are eight motors, four operating in a horizontal motion, and four vertically. Six of the motors position the NGS and two position the central science target. The LGS will be configured to give a symmetrical pattern whose separation can be changed manually as it is expected to be required only infrequently.

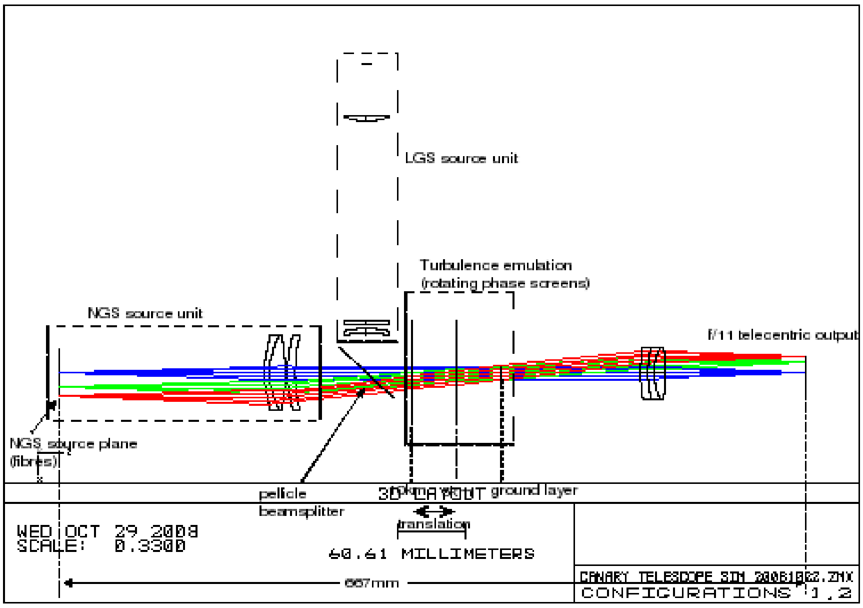

Figure 5.3: Turbulence simulator layout. Image taken from CANARY design review, 2008. Flipped horizontally relative to Figure 5.2.

Light travels through the collimating optics to the turbulence simulator. The phase screens are positioned such that the optical path samples an aperture on the outside edge of the phase screen. The phase screens are circular discs, with turbulence patterns etched onto the surface. Turbulence is simulated by each 'pixel' of the phase screen containing a variable optical path length. A planewave travelling through the phase screen results in a wavefront with spatially varying phase. The etched pattern is created from a Kolomogrov power spectrum. The phase screens are rotated to obtain a continuously altering turbulence, simulating wind velocity. A rotational velocity of 1rpm corresponds to a turbulence wind speed of ∼1m/s. The brackets containing the phase screens can be seen in Figure 5.5. The phase screens operate on sliding bars within the optical path, allowing the position of the phase screens to be altered. The location of the phase screens in the optical path determines the altitude at which the turbulence is simulated.

Beyond the phase screens, optics re-image the collimated beam, producing a f/10.84

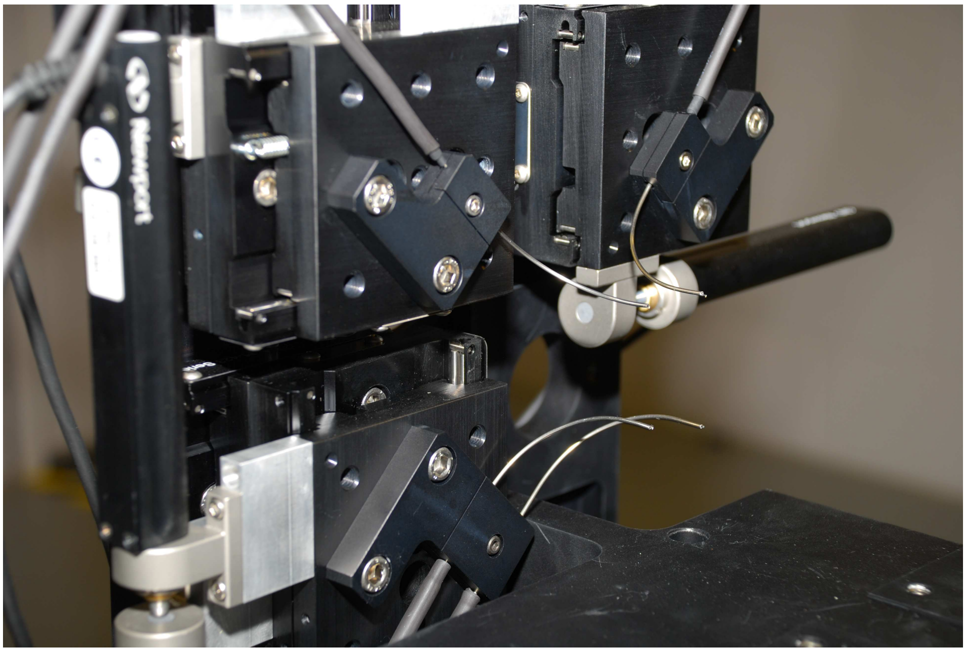

Figure 5.4: NGS motors layout. Three pairs of motors control the four NGS, with two NGS fibres attached to the bottom motor stage. The science target light stage sits between the NGS fibres, although not shown in this image.

telecentric output, the same as the WHT. The simulator optics create a focal plane with the same plate scale as the WHT, which during laboratory testing is the input to CANARY. The LGS module seen in Figure 5.3 is not installed until phase B.

The aim of CANARY is to test the on-sky feasibility of MOAO technology and has not been conceived to investigate solutions to mitigate the effects of spot elongation. Spot elongation is seen as a large obstacle to overcome when using sodium LGS with large aperture telescopes. The layer in the atmosphere where sodium resides is approximately 10km thick. When measured by a SHWFS, the central sub-apertures measure a circular spot as the beacon is seen along the line of sight. If the telescope aperture is small then the sub-apertures at the edge of the SHWFS also measure a fairly circular spot. As the telescope diameter increases, the spot becomes elongated (as illustrated in Figure 5.6). Using trigonometry and small angle approximations, the elongation of the beacon is given by:

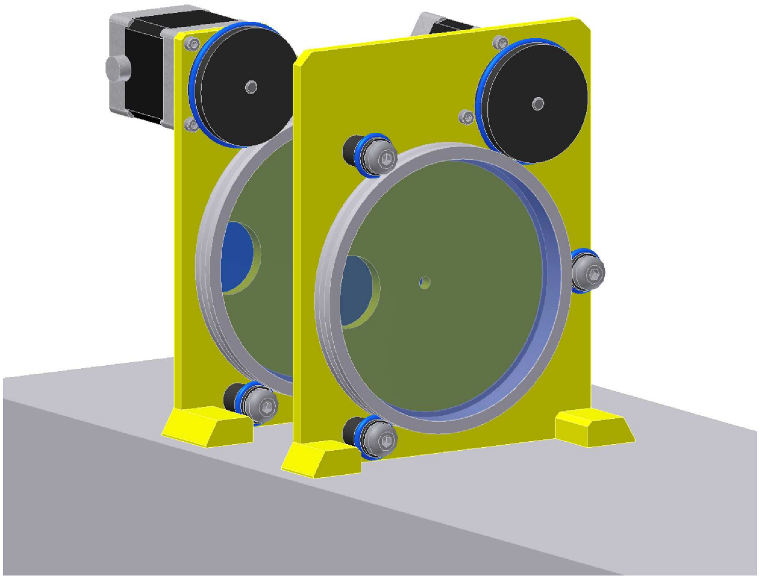

Figure 5.5: CANARY turbulence simulator. The cogs at the top rotate, determining the rotational velocity of the phase screens and so the simulated wind velocity.

$$\theta \simeq \frac{L\Delta H}{H^2 + H\Delta H} \tag{5.1}$$

The accuracy in reconstructing the wavefront is dependent on the ability to centroid the spot. Spot elongation reduces this centroiding ability and hence reduces the wavefront reconstruction accuracy. Consider a SHWFS, each sub-aperture contains $n \times n$ pixels. As the tilt of the wavefront over that sub-aperture increases, the centroid location moves further from the centre. The maximum gradient measurable is determined by the distance the spot can travel within the sub-aperture, known as the dynamic range. If the gradient of the wavefront sub-aperture increases to a large value, the sub-aperture spot will travel into the adjacent sub-aperture detector region, causing considerable problems for wavefront reconstruction. This is a particular issue for open-loop systems, where the actual wavefront tilts are measured, unlike the residual tilts of closed-loop systems. Travelling into adjacent sub-apertures is an issue for all open-loop systems, however, spot elongation increases this likelihood. It is sometimes overcome by adding a buffer around the outside of the sub-apertures, but again this

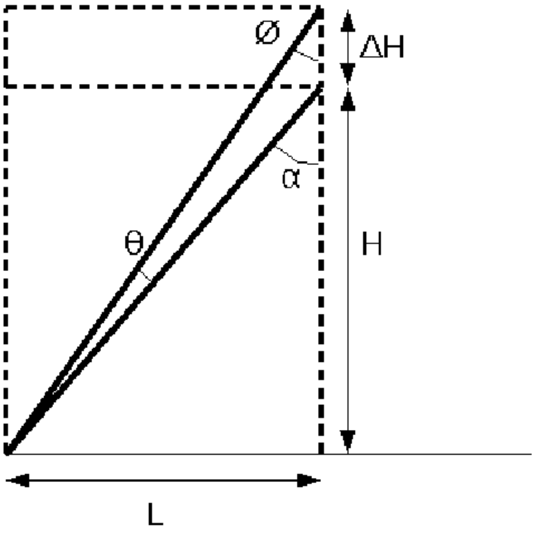

Figure 5.6: Elongation of beacons from sodium LGS as telescope aperture (D) increases. L is distance of the sub-aperture to the LGS, H is altitude of sodium layer, and ΔH it the depth of the sodium altitude layer.

affects wavefront reconstruction as sections of the wavefront are missing. For the E-ELT, the spot elongation will be ~5". EAGLE will use open-loop WFS, meaning large wavefront tilts will be measured on top of the 5" spot elogation. Either the dynamic range will be reduced for the outer sub-apertures or, the dynamic range will be increased for all sub-apertures, and so will reduce the sub-aperture resolution across the wavefront.

Spot elongation also spreads any LGS signal over more pixels, reducing the Signal-to-Noise Ratio (SNR). This is not as great an issue as it would be for NGS as the power of the laser can be increased, raising the SNR.

Currently it is unknown to what extent these issues will effect wavefront reconstruction, or how WFS will have to adapt in order to handle the large dynamic ranges involved. Although there will be no direct attempts to address this issue with CANARY, there are plans to investigate WFS accuracy with elongation by altering the Rayleigh LGS range gate.

5.2 Optical Aberrations

I have been involved in the alignment of the telescope simulator relay optics and measuring the wavefront error introduced by optical aberrations. For a perfect optical system, a sharp diffraction-limited image is formed at the image plane. Slight imperfections in the system lead to blurring and distortion effects, reducing image quality. There are various forms of aberration caused by the geometry of an optical system. Some aberrations are due to wavelength dependence, while others are monochromatic (Wyant & Creath, 1992). The optical system of a optical/N-IR telescope can be considered circular and rotationally symmetric.

’Piston’ refers to a shift in the zero phase location of the wavefront. ’Tilt’ causes a shift in location of the object in the image plane. Neither of these terms are strictly aberrations as, if only these terms are present, a perfect image will still form in the image plane.

Figure 5.7 illustrates various forms of aberration. Defocus results in a longitudinal shift of the focal point and results in a loss of sharpness. The light from an astronomical target can be assumed to have come from an infinite distance and so telescopes are focused at infinity. Spherical aberrations occur when rays near the optical axis have a different focal length to rays further away and so do not converge to a single point. A system with coma aberrations will focus an on-axis object perfectly, but off-axis objects will be out of focus, causing an off-axis object to appear “comet like”. Astigmatism occurs when the optics are not perfectly symmetric, with the focal point along one axis shifted relative to the other. Field curvature occurs when the optical system causes a flat object to lay along a curved image plane, rather than a flat image. Distortion causes the shape of an image to change depending on its field position, with on-axis objects remaining in focus, while off-axis rays are distorted. The most common form are radially symmetric distortions.

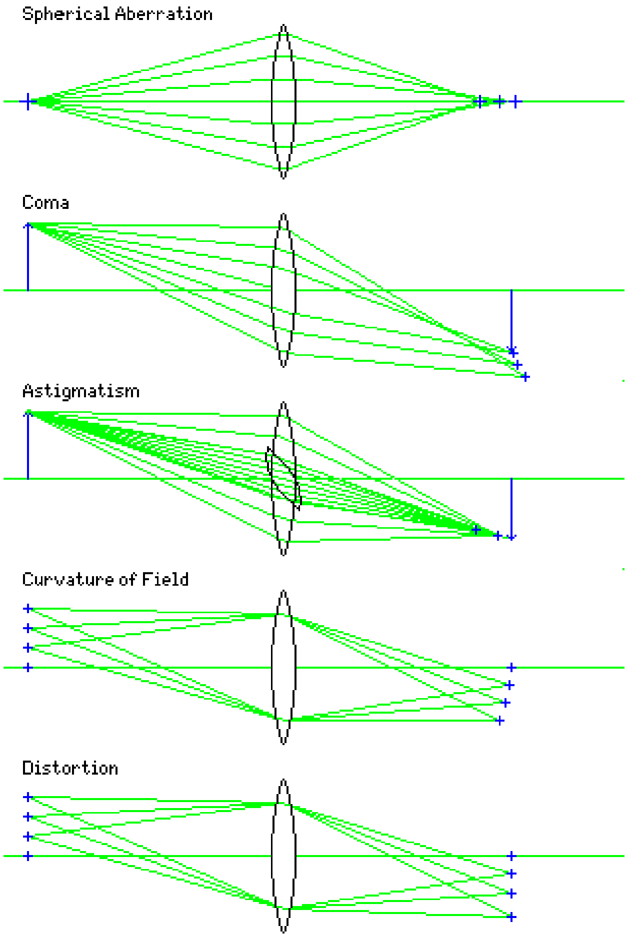

Figure 5.7: An illustration of various forms of monochromatic aberration. The blue crosses indicate the focal points for various rays. Courtesy of John J. G. Savard.

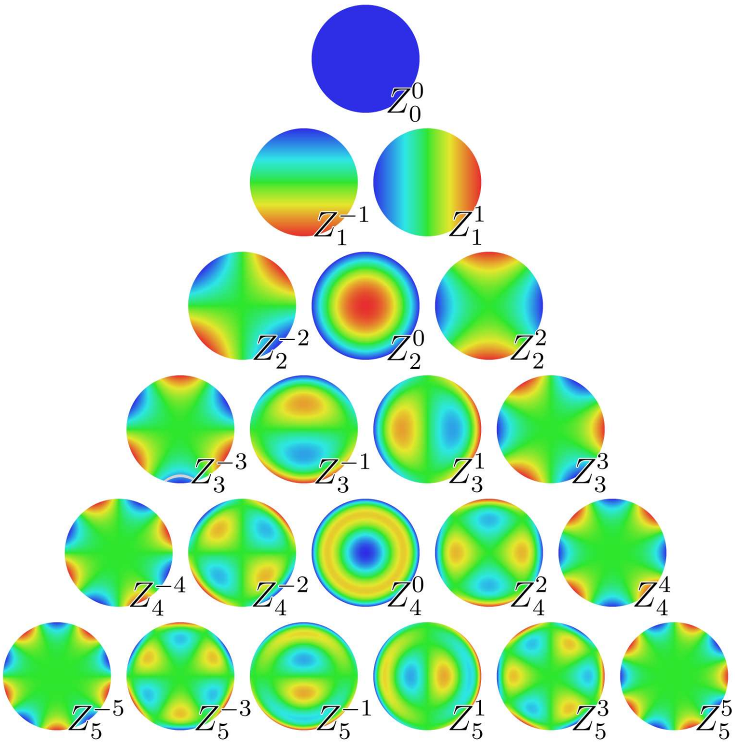

Figure 5.8: The first 21 Zernike polynomials, courtesy of Claudio Rocchini.

5.2.1 Zernike Polynomials

A useful method for describing a wavefront and so the contribution of particular aberrations is through Zernike polynomials. Zernike polynomials are an infinite set of orthogonal polynomials over a unit disk which, when combined, can perfectly recreate an aberrated wavefront. An aberrated wavefront that contains no high frequency distortions, such as a plane wave distorted by a telescope optical system, can be accurately defined by the first set of polynomials. This is because each polynomial is similar in form to a type of aberration (see Fdigure 5.8). Even and odd Zernike polynomials are described by *sine* and *cosine* terms as indicated in Table 5.1. ϕ refers to the azimuthal angle, ρ is the radial distance of the unit circle, and m & n are non-negative integers defining the polynomial. Zernike polynomials were used to determine the aberrations in the optical system during alignment, as described in the next section.

Table 5.1: Table of the first 15 Zernike polynomials. ϕ is the azimuthal angle, ρ is the radial distance of the unit circle, and *m* & *n* are non-negative integers defining the polynomial.

	n	m	Function	Aberration
1	0	0	1	Piston
2	1	1	$\rho sin(\phi)$	Tilt (y-direction)
3	1	-1	$\rho cos(\phi)$	Tilt (x-direction)
4	2	2	$\rho^2 sin(2\phi)$	Astigmatism 1^{st} order 45°
5	2	0	$2\rho^2 - 1$	Defocus
6	2	-2	$\rho^2 cos 2\phi$	Astigmatism 1^{st} order 0°
7	3	3	$\rho^3 sin(3\phi)$	Trefoil 30°
8	3	1	$(3\rho^3 - 2\rho) sin(\phi)$	Coma (y direction)
9	3	-1	$(3\rho^3 - 2\rho) cos(\phi)$	Coma (x direction)
10	3	-3	$\rho^3 cos(3\phi)$	Trefoil 0°
11	4	4	$\rho^4 sin 4\phi$	Tetrafoil 22.5°
12	4	2	$(4\rho^4 - 3\rho^2) sin(2\phi)$	Astigmatism 2^{nd} order 45°
13	4	0	$6\rho^4 - 2\rho^2 - 1$	Spherical
14	4	-2	$(4\rho^4 - 3\rho^2) cos(2\phi)$	Astigmatism 2^{nd} order 0°
15	4	-4	$\rho^4 cos(4\phi)$	Tetrafoil 0°

5.3 Telescope Simulator Alignment

This section describes tests carried out to determine if the telescope simulator optics perform within the specifications. The specifications require that when the beam travels through a SHWFS with 15x15 sub-apertures, the average local gradients are less than $0\farcs3$ as determined by the SHWFS centroiding ability. The telescope simulator was aligned using an interferometer in which the lenses were aligned by overlapping the laser reflections from the optic surfaces.

After the telescope optics were aligned, the maximum slope across the wavefront was determined using the independent methods of an interferometer and a WFS. The

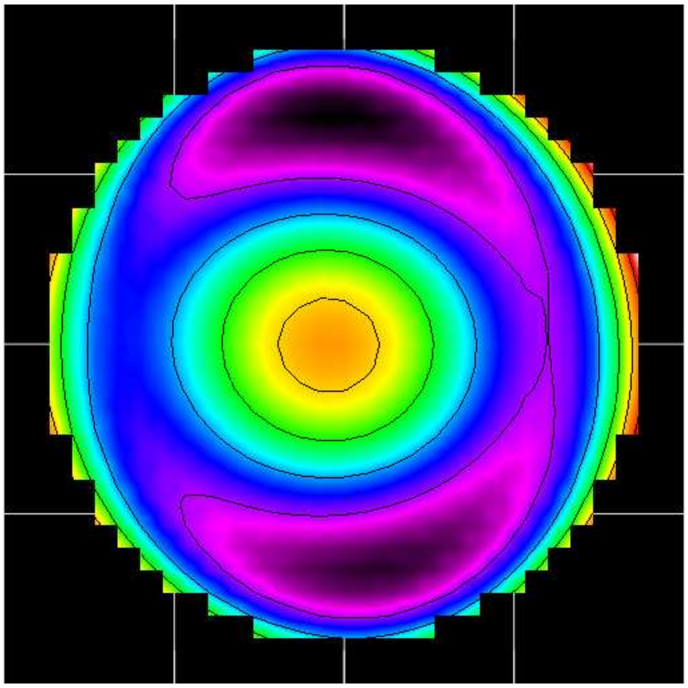

Figure 5.9: Output aberrated wavefront from WFS constructed from Zernike polynomials for on-axis when measuring optical alignment.

data were analysed using purpose-written `idl` programs. A wavefront was constructed from the binary output data from the interferometer. Similarly, a wavefront was formed from Zernike polynomial coefficients, calculated by the WFS positioned at the aperture plane (see Figure 5.9). The programs divide each image into 15x15 sub-apertures and the subsequent average gradients in both x and y axes were found. Least squares matrix calculations were used to determine the gradients in both x and y axes. Wavefronts were measured using both on and off-axis sources.

5.3.1 Results

Due to the circular nature of the aperture, some of the (15×15) sub-apertures are empty or only partially contain data, as highlighted in Figure 5.10. The sub-apertures at the edge of the field contain the least data and this is also where the largest distortions occur. As these apertures do not give a fair representation of the average wavefront

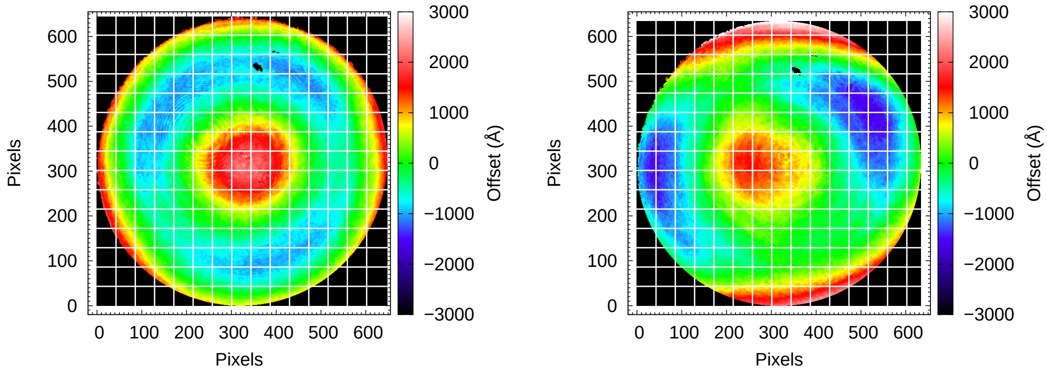

Figure 5.10: Output wavefronts from the interferometer for alignment wave aberration measurements. The overlying grids depict the wavefront split into sub-apertures. *Left*: on-axis, *right*:off-axis.

gradient compared to the filled sub-apertures, the results have been compiled in two formats. Table 5.2 provides the minimum and maximum gradients in x and y over all apertures for various source positions (on and off-axis). Table 5.3 gives the minimum and maximum values for sub-apertures which are filled by 50% or more.

The quoted positions relate to the light source positions in the focal plane, where (0,0) refers to the centre of the field. The off-axis measurements recorded by the WFS were positioned using the off-axis fibres with locations calculated using the positioning programme described in Section 5.4. The interferometer data were positioned using only the on-axis fibre motors.

Most of the results remained well within the slope requirements, with all but one term from the WFS data being above the $0\overset{\prime\prime}{.}3$ requirement. When all apertures were considered, the interferometer data contained six instances where the specifications were breached. However, when reduced to apertures that are 50% occupied or more, all of the results were well within the requirements.

The tests conclude that the optical system alignment is satisfactory and performs within specifications.

Table 5.2: Maximum and minimum wavefront error recorded across 15x15 sub-apertures. The first nine rows represent the WFS data, the lower five rows represent the interferometer data. x and y positions are given in focal plane positions relative to the on-axis fibre [0,0].

x pos [mm]	y pos [mm]	Max x [arcsec]	Min x [arcsec]	Max y [arcsec]	Min y [arcsec]
0	0	0.14	-0.20	0.16	-0.14
-18.27	-0.18	0.06	-0.07	0.20	-0.16
-22.89	-0.11	0.13	-0.13	0.23	-0.50
37.08	0.04	0.07	-0.15	0.19	-0.16
32.04	0.04	0.07	-0.08	0.24	-0.21
0.81	-17.22	0.16	-0.22	0.09	-0.06
0.81	-22.19	0.25	-0.26	0.09	-0.11
-8.75	9.9	0.19	-0.19	0.07	-0.07
-8.75	14.8	0.24	-0.33	0.12	-0.12
0	0	0.22	-0.11	0.46	-0.11
-14	0	0.43	-0.14	0.21	-0.14
14	0	0.48	-0.23	0.41	-0.23
0	-14	0.62	-0.11	0.70	-0.11
0	14	0.19	-0.09	0.29	-0.09

5.4 Positioning Algorithm

An algorithm was written to translate the movements of the NGS fibre motors to asterism positions. The program has been used for laboratory testing at the UKATC, and will also be used for asterism positioning when testing CANARY in the laboratory at WHT.

A focal-plane camera recorded the asterism positions (in pixel space) over a grid of motor positions. Using various distances across the grid, the distance scale between motor movements and resulting focal plane movements was found. There are six mo-

Table 5.3: Maximum and minimum wavefront error recorded across 15x15 sub-apertures, only including regions where over 50% of the sub-aperture contain data. The first nine rows represent the WFS data, the lower five rows represent the interferometer date. x and y positions are given in focal plane positions relative to the on-axis fibre [0,0].

x pos [mm]	y pos [mm]	Max x [arcsec]	Min x [arcsec]	Max y [arcsec]	Min y [arcsec]
0	0	0.12	-0.17	0.13	-0.11
-18.27	-0.18	0.06	-0.07	0.19	-0.15
-22.89	-0.11	0.13	-0.13	0.22	-0.49
37.08	0.04	0.05	-0.13	0.16	-0.14
32.04	0.04	0.07	-0.08	0.22	-0.20
0.81	-17.22	0.14	-0.20	0.07	-0.06
0.81	-22.19	0.23	-0.25	0.09	-0.12
-8.75	9.9	0.17	-0.18	0.06	-0.06
-8.75	14.8	0.23	-0.31	0.12	-0.13
0	0	0.12	-0.11	0.13	-0.11
-14	0	0.16	-0.14	0.08	-0.14
14	0	0.22	-0.20	0.11	-0.20
0	-14	0.08	-0.07	0.16	-0.07
0	14	0.11	-0.09	0.18	-0.09

tors controlling the NGS, three of which operate vertically and three horizontally. A travel of 1mm by the motors results in an a NGS focal plane movement of 0.7mm in both the horizontal and vertical directions. All the motors are independent from one another and so there was an angular offset between all the horizontal axes and likewise for the vertical. The grid of data points was used to find the angular offset between the axes and all motors were calibrated to a single horizontal and vertical reference axis.

The central reference position for the focal plane was set as the centre of the focal plane, where the central fibre is located. Each fibre only has a certain range of motions and to avoid collisions only the central fibre covers the reference position. Therefore, interpolation was used to determine what movement would be required to reach the central reference for the other axes. With all the axes calibrated to the same system and with the ratio of motor-to-focal plane movement known, accurate, repeatable asterisms can be created. When CANARY is moved to different test beds or the telescope, the motors are disassembled and so re-calibration is required. The algorithm is adaptable from different configurations, with only a new set of input grid positions required.

The accuracy of the algorithm was tested through moving the motors to various random positions within the camera FoV. An image of the asterism was taken and pixel and motor positions recorded. The pixels values were converted into focal plane positions (in mm). These were then compared with values predicted by the algorithm. All results were found to exhibit an error of less than ±0.05mm. There are two main sources of error. The camera detector is not uniform across the whole FoV and so in the corners of the image the number of pixels does not correspond to the same focal plane distance as in the centre. Secondly, the pixel centroids were measured through a detection routine within the STARLINK package, GAIA. The camera exposure time was set to its shortest setting, but many of the final images still contained saturated PSFs. This affected the centroiding ability of the object detection program. The accuracy and repeatability of the motors have not been tested and so the effect of positional uncertainties are unknown, however, motor travel is not expected to vary over long testing periods.

The specifications state a positioning accuracy of 1" is required. The scale at the WHT focal plane is 4.51arcsec/mm and so ±0.05 corresponds to a positioning accuracy of 0.″22, well within the requirements.

5.5 Asterisms

AO systems require bright GS to measure and correct atmospheric distortions, while their angular separations determine the volume of turbulence covered. The asterisms must be bright enough for the SHWFS to obtain robust centroids, with this magnitude limit being derived through instrument simulations at the University of Durham. The magnitude range is expected to be $\sim$10-13$^{\mathrm{m}}$ in the V-band.

For tomographical corrections, the three NGS and the science object must lie within a small FoV. A number of factors limit the maximum separation between sources. The maximum acceptable separation is dependent on the isoplanatic angle (hence atmospheric turbulence and wavelength) and the correction algorithm. If the stars are over-separated, the phase fluctuations between the different directions are no longer correlated and tomographic reconstruction becomes difficult. A maximum separation is also imposed by the size of the FoV, which is limited to a 2' diameter due to the instrument derotator. In practice it is this parameter which limits the maximum NGS separations for CANARY, not the tomographic constraints.

CANARY must have a selection of suitable asterisms which fill these criteria accessible all year round so that, in principle, it can be used at any time. From WHT this means they require declinations between 28.3 $\pm$ 60°. The position of the Moon must also not hinder observations of the asterisms. A total of 207 asterisms meeting the specifications (from the Tycho-2 catalogue (Høg et al., 2000)) were selected by collaborators at the Observatoire de Paris (Kellerer, 2008). Asterism 1 is shown in Figure 5.11. Of all the asterisms selected, six were highlighted in the appendix of the CANARY final design review. For the telescope simulator to be as accurate and realistic as possible, the telescope simulator must be able to re-create the asterisms precisely for laboratory testing. Tests validating this are now presented.

5.5.1 Method

Of the six suggested asterisms, three contained more than the minimum four stars. These asterisms were used to create variations of asterisms containing only three NGS, in order to test as many asterisms as possible. This created a total of 12 potential asterisms, along with the inversion of each, to create 24 tests. The NGS fibres were configured to each asterism pattern in the focal plane, with the central star located

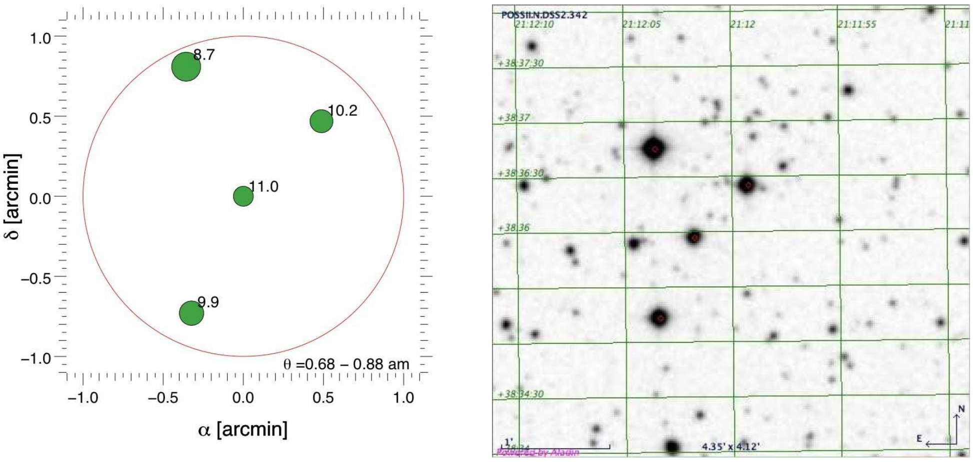

Figure 5.11: Asterism 1 from the CANARY design review (2008). *Left*: θ values at the bottom represent max and min source separations. *right*: *I*-band image from the DSS survey.

on-axis. The ability to rotate the telescope focal plane allows any azimuthal configuration. If it was not initially possible to re-create the asterism with the fibre motors, the asterism was rotated to an alternate position and re-tested.

5.5.2 Results

All of the asterisms could be re-created by the fibres at the focal plane. It was often the case that the asterism needed to be rotated for the fibres to be able to reach the required positions. Even so, when the best azimuthal position configuration was used, two of the asterisms required the motors to be on the limits of travel. All asterisms are satisfactory and will be used in the laboratory to simulate on-sky conditions and to test the performance of the AO system.

5.6 Turbulence Simulations

A three year study of r_0 at the WHT found a median seeing value of $0\farcs69$ (Breare & Mahony, 1996). The turbulence phase screens are therefore required to produce PSF FWHMs of $0\farcs6$ - $0\farcs7$. The phase screen turbulence patterns were designed using a specifically written PYTHON program, created by Dr. Tim Butterley from the CfAI.

The phase screens contain turbulence patterns prescribed by the Kolmogorov model of turbulence, containing both an inner and outer scale length. Although phase screens can re-create PSFs similar to that of atmospheric turbulence, there are some manners in which the turbulence simulator is not consistent with the atmosphere.

- The telescope simulator of CANARY only contains two atmospheric layers, each of constant depth. In reality the atmosphere is continuous and can contain multiple strong layers of varying depth and altitude contributing to the distortion.
- The inner and outer scale of the atmosphere change temporally, whereas this is not possible with the phase screens.
- The change in phase from the phase screens is created by etching new layers on top of each other. This results in phase changes occuring in discrete steps. The phase distortions from the atmosphere are continuous, lacking both “pixel” size and step height.
- The phase screens rotate, causing the phase distortions repeat themselves; the atmosphere is always evolving, with little repetition.

Currently no system can perfectly replicate the atmosphere within a laboratory enviroment, however, this is not necessary for most tests. The benefit of having a predictable phase distortion set-up is that it allows excellent characterisation of the system, determining where any potential errors within the system occur.

Tests have been carried out to determine whether the phase screens produce the required seeing values. A specifically written `idl` program has modelled the turbulence simulator, using the turbulence phase screen maps to generate expected PSFs. The computer generated PSFs have also been compared to results using the telescope simulator in the laboratory. If the results from the telescope simulator show the specifications have not been met, computer models could help determine whether the cause is due to the phase screen turbulence maps, or the telescope simulator.

5.6.1 Computer Simulated PSFs

This section describes the program I have created to generate PSFs from the turbulence phase screen maps. The turbulence maps used to create the High altitude Phase Screen (HPS) and Ground Layer Phase Screen (GLPS) were read into an `idl` program. The phase screens have a diameter of 900 pixels and the telescope beam corresponds to an aperture diameter of 120 pixels. The on-axis source samples the phase screen at a radius of 285 pixels from the phase screen centre. The HPS and GLPS contain the same turbulence pattern, but the etched steps have different optical path lengths. Most turbulence is generated in the lowest layers of the atmosphere and so to create greater distortions, the optical step size was larger for the GLPS. The starting rotation positions of the turbulence maps were varied by rotating the HPS pattern by 180° relative to the GLPS. The wavefront distortion for the HPS was determined for both an on-axis and off-axis source. The distorted wavefronts are then aberrated by the GLPS, creating the final wavefront. The atmosphere immediately above the ground is sampled by all GS, regardless of their angular distribution, and so both the on-axis and off-axis sources sample the same section of the GLPS.

Theoretical intensity distributions were created by applying Fourier transforms to the turbulence patterns. The intensity pattern created by constant turbulence is effectively a scintillation pattern. After calculating one intensity pattern, the turbulence maps were rotated by θ, so that the central position of the apertures shifted by one pixel. The intensity pattern for each rotation was recorded and combined to create a co-added PSF. The phase screens were rotated through 360° to create the final combined PSF.

The computer generated PSFs are extremely oversampled and so to make an accurate prediction of what will be observed by CANARY, the PSFs were resampled to the pixel scale of WHT. Each pixel of the Fourier transform has a size of $1/NT$ where N is the number of pixels within the array in each direction, and T is the sampling at the telescope pupil plane. A 4.2m telescope over a 60 pixel aperture radius corresponds to 0.035m/pixel. The final pixel scale of the simulations is given by:

Table 5.4: Computer model results of turbulence simulations. Position 0,0 corresponds to on-axis position, 0.1 is a shift to off-axis by 0.1 of a phase screen.

Position	Direct FWHM (arcsec)	Gaussian FWHM (arcsec)
0.0	0.58	0.57
0.1	0.67	0.61
0.2	0.69	0.63
0.3	0.66	0.65
0.4	0.68	0.66
0.5	0.68	0.65
0.6	0.68	0.68
0.7	0.67	0.64
0.8	0.67	0.66

$$p = \frac{\lambda}{NT}. \tag{5.2}$$

For red light (633nm) this gives a pixel scale of 0.0073 arcsec/pixel. The WHT has a FoV of $2\overset{\prime}{.}5$ over 2048 pixels giving a pixel scale of 0.073 arcsec/pixel. The numerically simulated PSFs were resampled to to this pixel scale, in line with the WHT.

Results

The theoretical FWHMs were measured using the IMEXAMINE package within IRAF. Values were determined through direct measurements and Gaussian fitting, as shown in Table 5.4.

The quoted positions correspond to the radial offsets between the apertures sampled by on and off-axis NGS. The position of 0.0 corresponds to the on-axis results, while for 0.5 there is a radial shift of half an aperture (60 pixels) for the off-axis HPS aperture relative to the on-axis.

Results provide good agreement with expectations with all, bar the on-axis sources ($0\farcs57$), performing well within the specifications. When combined with the wavefront errors from the optics, the delivered on-axis FWHM will be $\geq 0\farcs6$ and so all results are deemed acceptable. This indicates that the turbulence phase screen *theoretically* reproduce the normal seeing conditions at WHT.

5.6.2 Measured PSFs

Laboratory tests were carried out to determine if the empirical effects of the phase screens lives up to their expectations and also to validate the accuracy of my PSF generating model. The rotating phase screens were imaged by a CCD camera placed at the focal plane. The phase screens were illuminated by the on-axis single-mode fibre. When the phase screens were removed, the central fibre produced a PSF with FWHM of $<0\farcs1$. Several series of measurements were taken with both phase screens in stationary positions and at various rotational velocities. When performing AO corrections, the velocity of the phase screen determines how often the corrections need be applied. When measuring the PSF, the rotational velocity and exposure time only define how much simulated turbulence has been experienced by the beam. Tests were carried out completing various fractional rotations of the phase screen, sampling different regions each time. This was done by keeping the exposure time the same, and varying the phase screen rotational velocity. The maximum rotation considered made one complete rotation.

Results

The PSFs were analysed using the IMEXAMINE package within IRAF. The specifications require FWHMs of $0\farcs6$-$0\farcs7$, and as Figure 5.12 shows, the phase screens performed as required. When a large fraction of the phase screens are sampled, a smoother, more symmetrical PSF is created, as expected. When the rotational fraction is <0.1 for both phase screen, the PSFs are unsymmetrical, which causes varying

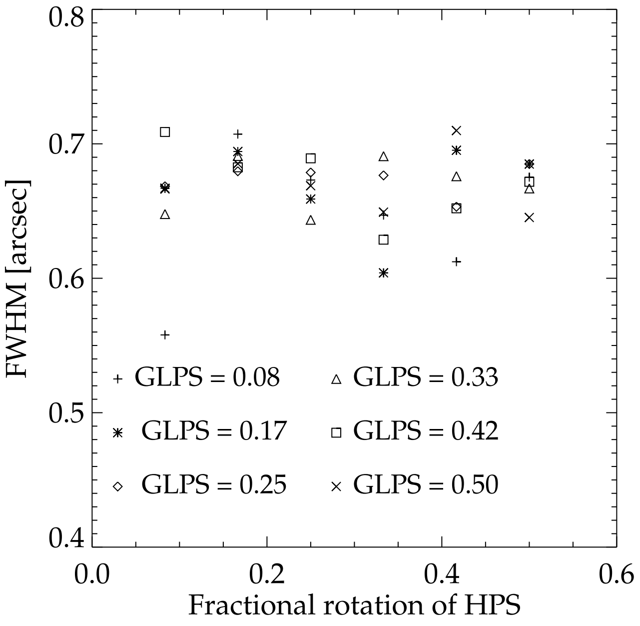

Figure 5.12: PSF-FWHMs created by sampling the phase screens by varying amounts.

FWHM values (see Figure 5.13). The results show that to guarantee reaching this range for an individual exposure, a rotation of at least one sixth of a phase screen is required per observation.

Both the computer simulations and telescope simulator results conclude that the phase screens perform within the specifications. The results also validate the simulated PSF program works accurately (a comparison between the computer generated PSF and laboratory PSF can be seen in Figure 5.14).

5.7 SLODAR

It is important to understand where all the sources of error occur in a novel system. Using Rayleigh LGS for turbulence corrections results in layers in the upper atmosphere being uncorrected for and so still contributing distortions to the final PSF. The sodium LGS on the E-ELT will measure the turbulence up to much higher altitudes than the

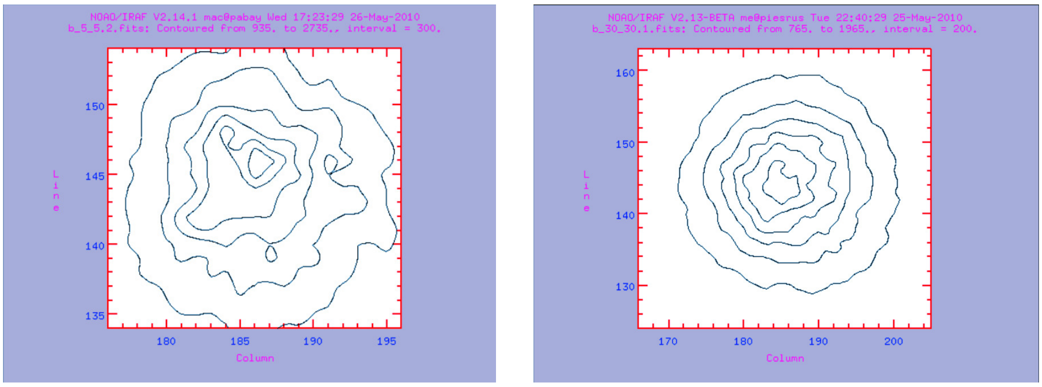

Figure 5.13: PSF contour plots for, *left*: both phase screens completing ∼0.1 of a revolution, *right*: both phase screens completing ∼0.5 of a revolution.

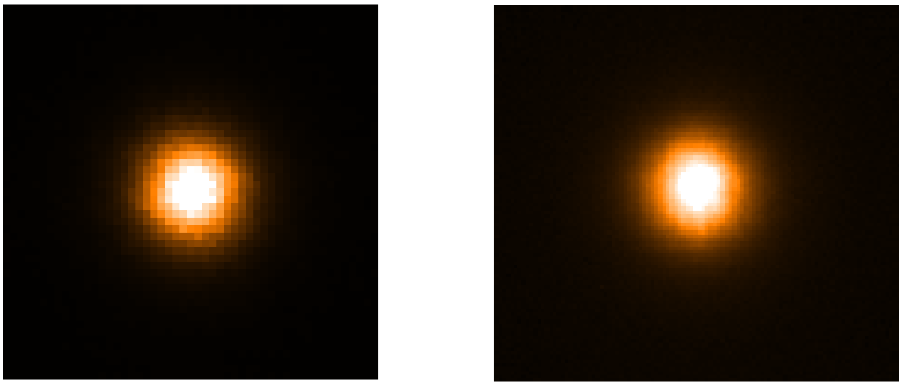

Figure 5.14: Simulated PSFs. *Left*: computer-generated PSF sampled at pixel scale of the WHT; *right*: telescope simulator PSF for both phase screens completing a full revolution.

Rayleigh LGS of CANARY. Knowing the complete turbulence profile above the WHT will provide insight into the correction performance of CANARY and the expected differences compared to EAGLE.

The vertical turbulence profile above the WHT will be mapped with a SLODAR instrument (see Section 1.2.3), which uses the CANARY SHWFSs. A second SLODAR instrument will also take measurements from the roof, increasing the maximum profile altitude to 20km. The WHT also has MASS-DIMM instruments and so the profile of the whole atmosphere can be determined.

The SLODAR technique can also be applied to the telescope and turbulence simulators to determine the influence of each phase screen on the observed PSF. Phase screen C_N^2 profiles can be compared to turbulence generated above the WHT, analysing the turbulence simulator accuracy. I have created computer simulations modelling the expected outputs from SHWFSs when observing various NGS asterisms through the turbulence simulator. Dr Richard Wilson at CfAI has a program which analyses SLODAR results, reproducing C_N^2 profiles. Comparison with laboratory SLODAR measurements determines whether the system is acting as expected. If there are any variations, the simulations can be used to determine the cause.

5.7.1 Numerical SLODAR Tests

Wavefront distortions were created for on- and off-axis sources, as done for the PSF simulations. The off-axis NGS has an angular separation from the on-axis NGS and varying the off-axis separation effectively alters the altitude with which results are taken. The angular separation corresponds to a radial offset between the central position of the on- and off-axis NGS sampling the HPS. Output wavefronts are created by multiplying the phase shifts by the wavelength ($\lambda = 633nm$). On sky, the pupil plane would be imaged by a SHWFS to determine the wavefront tilt over each sub-aperture. This was simulated by splitting the wavefronts into 7x7 sub-apertures as illustrated by Figure 5.15.

Due to the circular nature of the aperture, not all sub-apertures fully sampled the

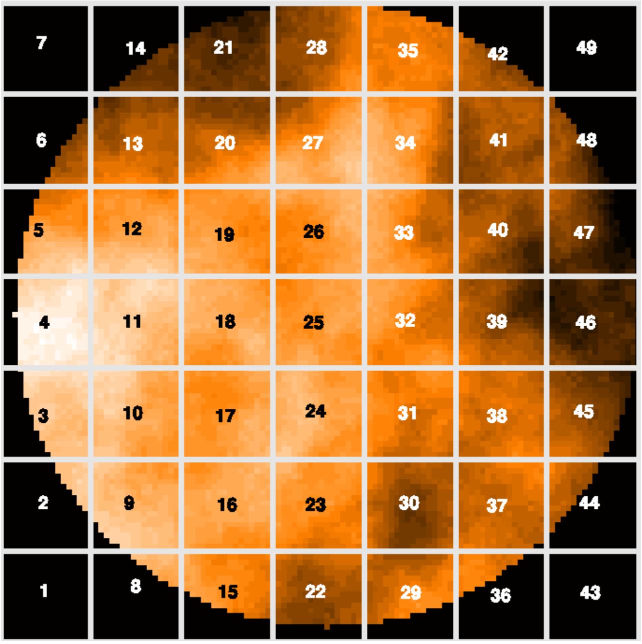

Figure 5.15: On-axis wavefront sub-apertures for θ=0°. Numbers reference the sub-aperture layout.

wavefront as mentioned in Section 5.3 (see Figure 5.15). A least squares linear plane function was fitted to the wavefronts in each sub-aperture, determining the x and y gradients in arcsec for each (see Figure 5.16).

To mimic the phase screen rotation, the whole process was repeated after re-centering the NGS apertures on the phase screens. The position of the re-centred apertures corresponds to an angular shift of θ from the centre of the phase screen. In practice, at the sampling radius, this resulted in a ∼1 pixel movement from the previous aperture position. The newly sampled apertures were then rotated by $-\theta$. This re-aligns the turbulence pattern to mimic the real rotation that occurs for the phase screens. The computational rotation introduces a form of smoothing through interpolation. As the phase screens are designed in steps this diverges from the laboratory process, however, it will simulate the on-sky situation more accurately as the atmosphere does not act in steps.

Tilt values were produced for a complete 360° rotation, with the output saved in data-cube FITS files. Results were for HPS offsets of 0.1-0.8 of a phase screen, with a 0.1 increment, between the on- and off-axis NGS.

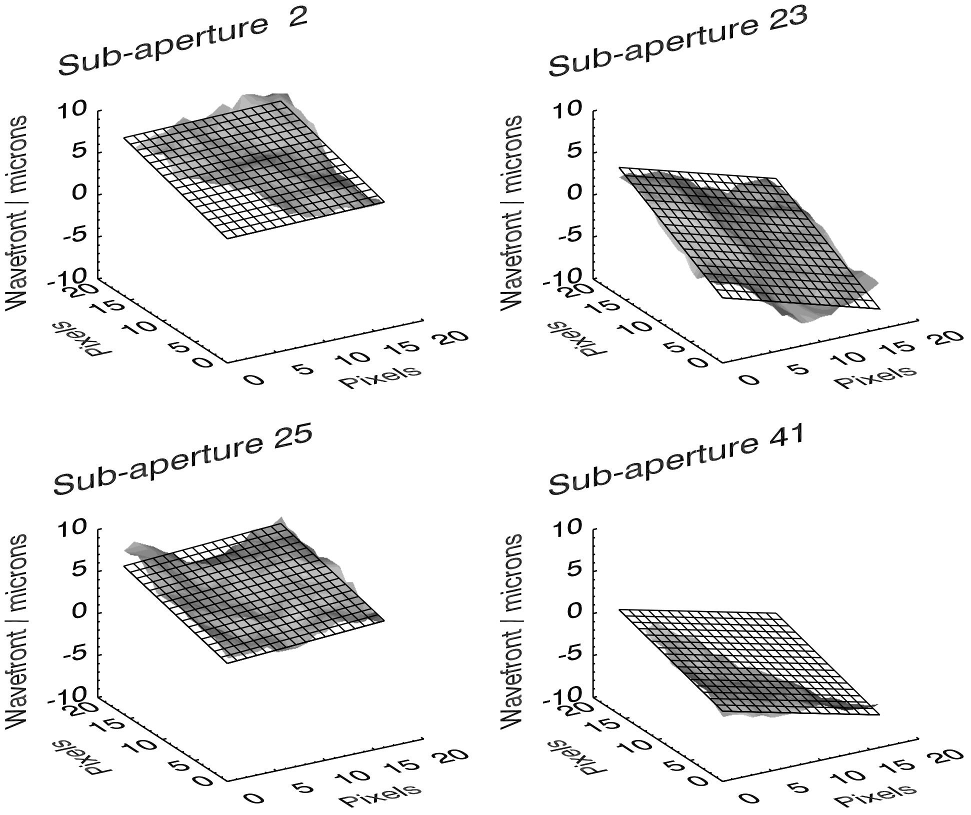

Figure 5.16: Linear plane functions fit to wavefront sub-apertures.

Results

At the time of writing, the program at the CfAI to analyse the SLODAR results was not at the stage to create C_N^2 profiles. However, to check that the SLODAR simulator was performing as required, Dr Richard Wilson from CfAI ran the results through a cross-correlation program (see Figure 5.17). For all results there is a clear peak in correlation for a zero offset, indicating the detection of GLPS turbulence experienced by both NGS. A second peak in correlation is also observable when an offset is applied between the stars. The peak becomes clearer when the angular separation between NGS increases and is difficult to resolve from the central peak when only an offset of

0.1-0.2 is applied. The central peak is a lot stronger than the offset peak. This could be due to the ground layer being perfectly centred on the central pixel, whereas the offset peak is not centred on a pixel. It is unclear why there is so much noise in the right and extreme left sides of the cross-correlations.

The results show that the influence of both phase screens can be observed, validating that the program simulating SHWFS observations through the turbulence simulator is working as expected.

5.7.2 Empirical SLODAR Tests

SLODAR tests were carried out in the laboratory using the telescope simulator. The SHWFSs were used to measure the local gradients of the wavefronts for three NGS and the central fibre. Results were taken rotating both phases at 4rpm, recording 250 images a second, creating a total of 3750 frames for each test. This corresponds to a full phase screen rotation as completed by the simulator. To confirm that the influence of both phase screens was observable, measurements were recorded with only the GLPS and then only the HPS rotating. The two phase screens operate on movable slides within the optical path and altering the positions on the slide determines at which altitude the atmospheric turbulence occurs. Measurements at various altitude positions were taken in the laboratory to determine whether the varying turbulent layer altitudes are resolvable and that they occur where predicted. Results were also taken keeping the phase screen altitude positions constant, while varying the rotational velocities of the phase screens. Varying the phase screen velocities has the effect of varying turbulence wind velocities. To ensure a constant 360° phase rotation, the number of frames recorded was adjusted with phase screen rotation velocity. The phase screen velocities ranged from 1-5rpm.

Results

From initial cross-correlation results it appears there are constant offsets across the WFSs which is inhibiting clear correlation peaks. It is likely this is due to a misalignment of the SHWFS when taking results. After subtracting the mean offset from the results, correlation peaks were observed (see Figure 5.18), however, applying a correct mean correction is difficult as each sub-aperture measurement, due to the nature of phase screens, contains a variable wavefront slope. This will be investigated in the future.

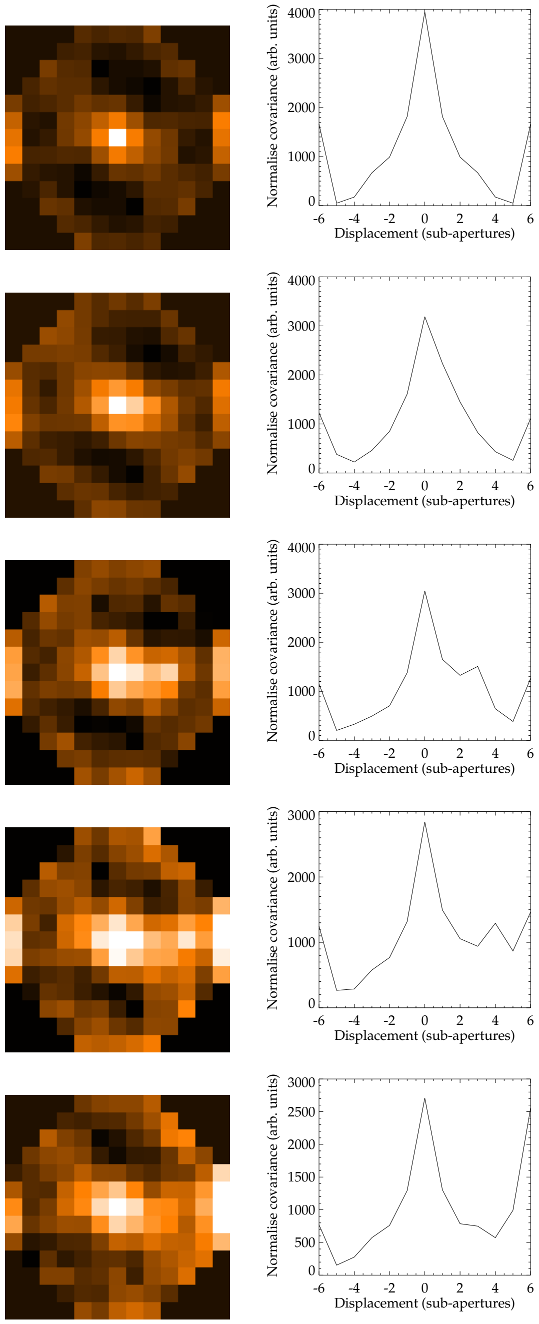

Figure 5.17: SLODAR cross-correlations for simulated data with. *Left*: two-dimensional cross-correlation plot; *right*: One dimensional slice through the two-dimensional correlation function in the direction of the binary star separation. The *top* panels are for results when there was a zero offset between the binary stars. The binary separation increase by 0.2 of a aperture radius, down to the *bottom* panel with a 0.8 offset.

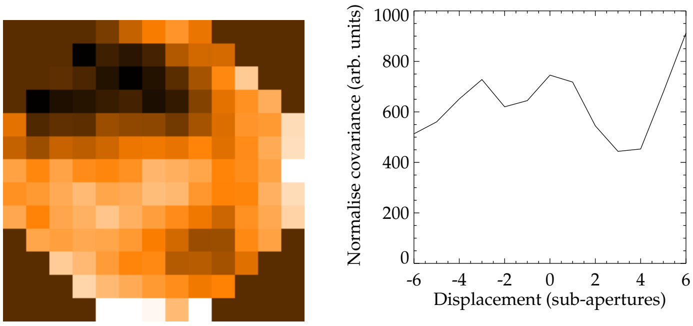

Figure 5.18: SLODAR cross-correlations for laboratory data. *Left*:two-dimensional cross-correlation plot for laboratory data after offset has been subtracted; *right*:One dimensional slice through the two-dimensional correlation function in the direction of the binary star separation.

Chapter 6

Summary

6.1 MAD

The angular resolution and image quality of the MAD data is truly impressive, confirming the high potential performance of MCAO technologies. Strehl ratios as high as $\sim$30% were achieved in the R136 observations, with uniform PSF FWHMs of $\sim 0\farcs1$ provided across the 1 arcmin FoV. The high image quality achievable with MAD is illustrated in the false colour image shown in Figure 6.1.

The difficulty in performing photometric calibrations on the MAD data (Chapter 2) has highlighted potential calibration problems when using high angular-resolution data. Without the HAWK-I images, large uncertainties would remain in the MAD magnitudes. Surveys such as the VISTA Hemisphere Survey (VHS; P.I, R. McMahon) will probe deeper than 2MASS at seeing limited resolutions of $\sim 0\farcs7$. Surveys such as these will provide a greater number of high-quality calibration sources, but for many regimes, particularly in distant galaxies (which will be resolvable by an E-ELT), there will be limited numbers of calibration stars available for future AO observations.

Furthermore, the angular resolution of the ELT will be an order of magnitude better than that of MAD, so many potential calibration stars will likely be resolved into separate components (as found in the MAD-2MASS calibrations); great care will be required for accurate calibration of ELT photometry.

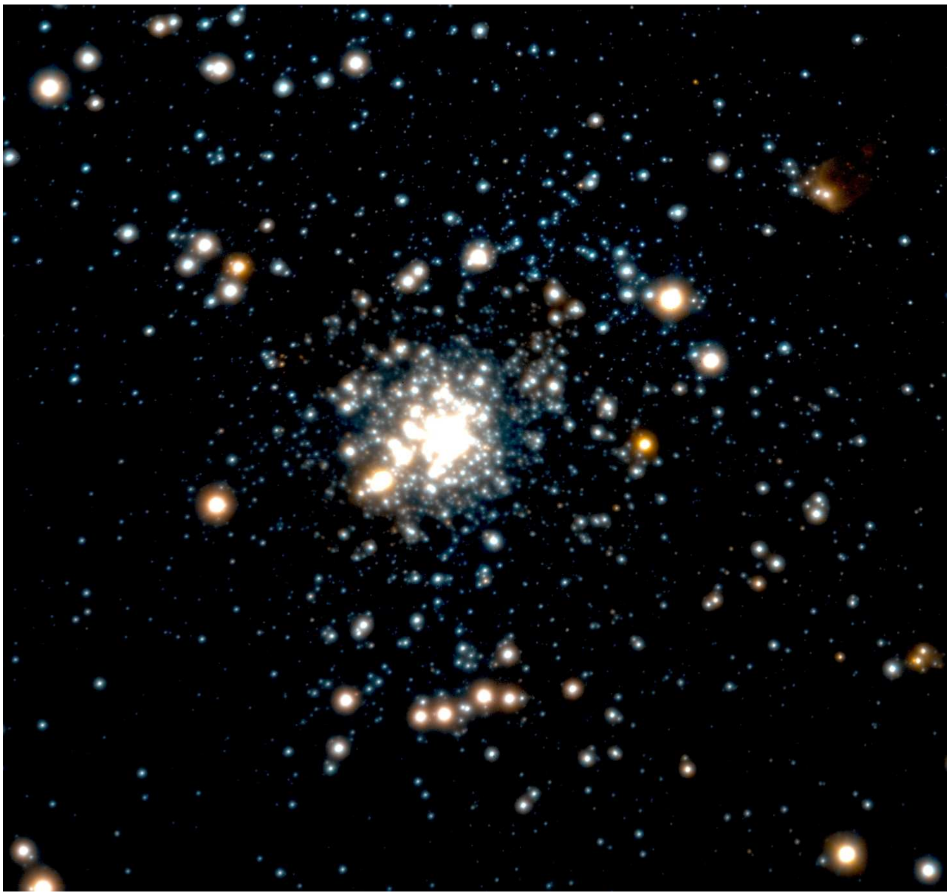

Figure 6.1: A false colour MAD image of R136.

MAD has demonstrated that science calibre observations are possible with MCAO, as demonstrated by the analysis of R136 presented in this thesis. Although the best method of data reduction and PSF-fitting takes some iteration, the technique is relatively straight-forward, after allowing the PSF to vary with spatial location. Three months before publishing the MAD R136 paper (Campbell et al., 2010), Andersen et al. (2009) published their long awaited *HST*-NICMOS paper on R136. The paper was 10 years in the making due to the difficulties in understanding the spatially varying, diffraction-limited PSF. Relative to the analysis of the *HST* data, the methods for PSF-fitting photometry from the MAD data were easy. Furthermore, the angular resolution of the MAD images is somewhat better than the IR *HST* image and arguably, the image quality of the MAD images exceeded that of *HST*. The slopes to the fits of the radial surface brightness profiles of both investigations were in good agreement. MAD has therefore demonstrated that *HST* quality observations can be gathered from the ground!

This does not suggest that with the advancement of AO technologies, space telescopes will become redundant. The high sensitivities possible in the N-IR from working above the atmosphere are difficult to match from ground based facilities. However, an important synergy will be formed with space telescopes such as *JWST*, with ELTs providing follow-up, at unmatched angular resolutions, probing regions that would otherwise be unresolvable with the smaller apertures of space telescopes.

A good example of what can be achieved with the benefit of wide-field AO systems is the recent re-analysis of the most massive stars in R136 (Crowther et al., 2010), using a combination of data from the SIngle Faint Object Near-Infrared (SINFONI) on the VLT and our published MAD photometry. SINFONI is an AO-assisted N-IR integral field spectrometer and was used by Schnurr et al. (2009) to observe the most massive stars within R136 (see Figure 6.2). The MAD K_S-band values were used to fit the spectra to evolutionary tracks, which estimated these colossal stars as having initial masses of $>200M_\odot$.

The demonstration of MCAO technology by MAD has paved the way for future instruments to take advantage of the wide-field correction techniques. One such instrument is the Phase A study of th Multi-conjugate Adaptive Optics RelaY module (MAORY) (Foppiani et al., 2010) for the E-ELT, which proposes using a combination of LGS and NGS to deliver a 2’ corrected field of view to a N-IR imager (called MICADO) (Davies & Genzel, 2010).

6.2 R136

6.2.1 Cluster Profile

As previously mentioned, the slopes of the surface brightness profiles are in agreement with the *HST* observations of Andersen et al. (2009). An explanation for the γ value

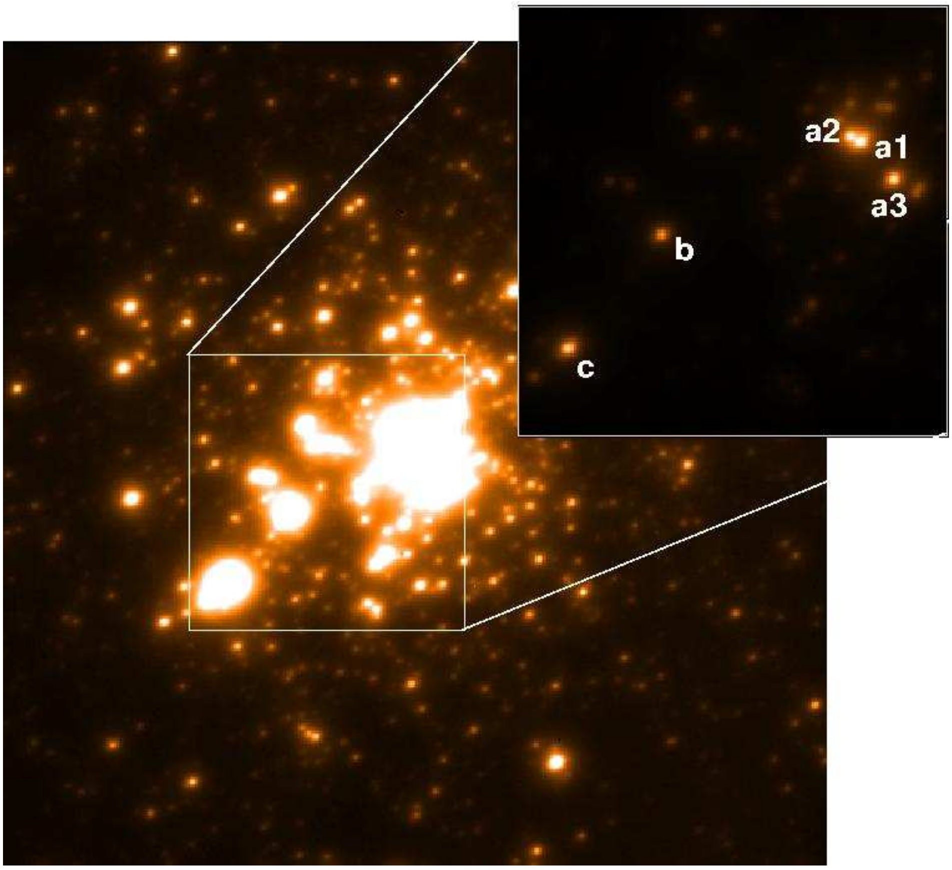

Figure 6.2: The collosal stars at the centre of R136 resolved in the K_S-band MAD images.

of ~1.55 seen in the surface brightness profile could be the result of a cloud collapse, with star formation occurring in the early phases of collapse, such that the dynamical interactions between the stars determine the properties of the cluster.

The MAD surface brightness profiles in Chapter 3 do not exhibit a “bump” at ~10" as seen in the optical. Excess light from stars would be wavelength independent and so this indicates that RGE is not the cause of the “bump” in the optical. Further investigation into the azimuthal profile of R136 from the MAD data suggests that the previous results were caused by cluster asymmetries.

The Vista Magellanic Clouds (VMC) survey plans to observe the entire Magellanic Clouds in Y, J, K_S-bands, reaching a sensitivity down to Y=21.9, J=21.4, and K_S=20.3 with a signal to noise of 10. Surveys such as this will produce data on a large number of YMCs, allowing RGE to be investigated on a statistical basis. As previously mentioned, the R136 profile has shown that cluster asymmetries should not be taken likely when interpreting the nature of excess light. Analysing the spatial distribution of YSOs around the periphery of R136 also suggests that YMCs are likely to instigate new surrounding regions of star formation. This triggered population is visible within the HAWK-I (and partially in the MAD) images and is easily distinguishable from R136. It should be noted that this will not be the case for much more distant clusters, and could be another cause of confusion when studying cluster profiles. In distant clusters, excess light from a triggered population may not be disentangle from the main cluster and could be misconstrued as evidence for RGE.

That said, these results do not suggest that RGE is an implausible phase of cluster evolution. In fact, it is likely that many cluster candidates suggesting RGE will be detected in the near future. However, care will be required in future investigations of RGE, with all empirical possibilities taken into consideration before a conclusion is drawn.

6.2.2 YSOs

The study of the YSO population of the region will be taken further with the new VMC data, combined with the FLAMES spectra, and additional follow-up. The VMC data will be used to search for photometric variables, allowing the detection of a large number of binaries over the entire Magellanic Clouds. Coupled with the spectra from FLAMES and other spectroscopic programs, information will be gained on the binary fraction within YMCs, adding to our knowledge of both star and cluster formation.

The importance of AO in such work is highlighted by Figure 4.19, where the seemingly normal star in the HAWK-I image is resolved into a blue star with a red companion. Follow-up AO observations in complex regions such as the periphery of R136 are necessary in order to achieve completeness, even just down to the intermediate-mass YSOs.

6.3 CANARY

At the time of writing, CANARY has arrived in La Palma and is being assembled in the laboratory at the telescope in preparation for alignment, before being moved on-sky. On-sky tests are planned for before the end of the year.

The simulation and laboratory SLODAR results (from Chapter 5) have been handed over to the CfAI and are awaiting completion of the analysis software. This will allow complete characterisation of the phase screens, determining the strength of the atmosphere generated by the two layers. Comparisons can then be made with the on-sky SLODAR measurements, assessing how realistic the phase screen generated C_N^2 profiles are.

The next two CANARY phases are on schedule and operations with both NGS and LGS are still planned in 2012.

6.4 ELT Summary

The site selection for the E-ELT has been made (Cerro Armazones, not far from Paranal), and the project is moving into the construction stage. In the coming months decisions on the instrumentation to be taken forward for first-light will be made. As this thesis has documented, adaptive optics systems are in a healthy position, providing ever improving corrections. Large telescopes around the world have plans to, or are currently installing AO system (such as GRAAL, the GLAO system for the VLT, of which HAWK-I will take advantage).

MCAO will be a key technology for E-ELT instrumentation, while the outcome of the CANARY observations will likely promote MOAO for future instruments. To make the most of the exciting potential that ELTs can provide, a range of technology and project issues will need to be optimised (an example of such can be seen in Appendix A). There are still challenges that need to be overcome before building an ELT. However, one thing is certain; MCAO and MOAO technologies will play a crucial role in achieving the outstanding high angular-resolution that ELTs offer.

Appendix A

Appendix

A.1 Serendipity

During my studies, I spent eight months at the Instituto de Astrofisca in Tenerife. I was involved in the development of a Multi-Object Spectrograph (MOS) EMIR and this section describes a piece of work looking at carrying out serendipitous measurements with EMIR.

As telescopes increase in size and complexity, the cost of the science produced follows suit. As we near the age of ELTs it becomes ever more important that they are run efficiently. The scientific community has noticed this and efforts to improve efficiency are being carried out in numerous different areas, from the design of the instruments, to increased organisation of proposals from the user community. Proposed telescopes such as the E-ELT and TMT, along with current facilities such as the 10.4m Gran Telescopico Canarias (GTC) and the 8m VLT need to make optimum use of their focal planes during each observation. On a telescope such as the E-ELT, it will be unattractive to accept a proposal wanting spectroscopy of one object over an eight hour integration time if multiple candidates are within the FoV. MOS instruments have been designed to increase the science output from each observation through the use of smart focal-planes, to observe multiple spectra simultaneously across a large FoV.

Multi-Slit Instruments

There are two main varieties of multi-slit instruments: slit masks and configurable slit mechanisms. Slit masks require a new mask to be created for each specific observation. This can be an expensive process, continuously requiring new materials, time overheads, and, in the case of GMOS, the cost of shipping each mask internationally. However, it can produce excellent results as each mask is specifically tailored for the individual observation (assuming the pointing, and object positions are accurate). Masks need to be swapped over fto be swapped over for every observation, but as the masks are ready before the observations, at optical wavelengths, with an experienced team, the time overhead need not be so large. In the N-IR this causes a problem as the mask and instrument need to be cooled, with instruments such as the Long-slit Intermediate Resolution Infrared Spectrograph (LIRIS) on the WHT require mask changes during the 'warm' engineering time.

Configurable slit mechanisms use sliding bars to produce different slit configurations. They are reconfigured for each observation and are versatile to different operational modes. The slits need to be reconfigured after each observation, at a small time overhead - the configurations are fast and much less intensive than replacing or swapping a whole mask. Furthermore, slit mechanisms have recently been proven to be operable at cryogenic temperatures, hence can be used in the N-IR range (e.g. the slit-unit built and tested for the KECK MOSFIRE). This greatly increases the observational time available per night, and so a great advantage over slit mask instruments.

An example of this technology is the Espectrografo Multiobjeto Infra-Rojo (EMIR), a N-IR MOS under construction for the GTC i n La Palma. With over 100 configurable bars, its multiplexing capabilities will allow up to 55 objects to be observed at once (see Figure A.1) (Garzón et al., 2007). Aligning the slits produces a long slit mode, while retracting all the bars creates an imaging mode. The imaging mode is an important inclusion as it allows direct target acquisition, removing any inaccuracies in telescope pointing and known target positions. Imaging also presents greater scientific opportunities, such as allowing deep imaging of faint, distant targets.

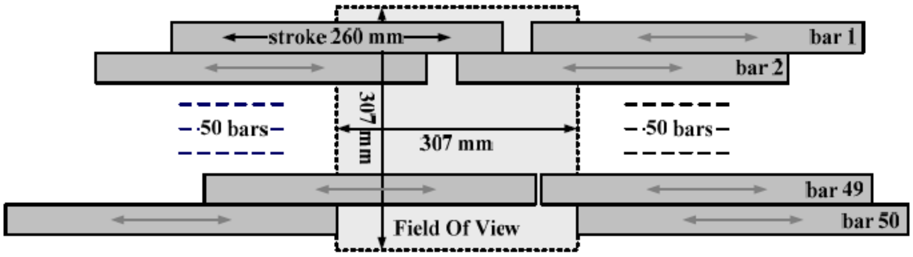

Figure A.1: Concept layout of EMIR configurable slit unit.

The spectral resolution can be altered by adjusting the slit widths, and so can be fine-tuned for specific targets. Since there are negligible light losses with slit spectroscopy, they are well suited for faint targets.

There are, however, limitations to using configurable slit mechanisms compared to other smart focal plane devices. The bar motion is along one axis, therefore it is only possible to target one object along that axis per exposure, limiting the spatial distribution of potential targets. Instrument rotation allows the number of observed objects to be optimised, however potential objects on the same axis will always be lost. Sometimes the objects will fall upon the bridge between two bars, although this can be overcome by aligning two slits together; extended objects can be observed in a similar manner. Dedicated slits can be used for sky measurements, using beam switching to alter between the sky and science frame (or depending on the type of target, objects can be dithered within the slits). Although diffraction effects can occur from the bars in the spatial direction, cross contamination of spectra is not a large issue.

Serendipity with EMIR

The ideal situation is that, for an instrument like EMIR, all slits are used in every exposure. However, this will not be possible for all science cases due to the source densities and spatial distribution of targets within the FoV. Serendipitous observations on EMIR to exploit unused slits will increase the scientific output, while keeping the cost the same. By simulating proposed science cases for EMIR, the possibility to carry out a long-term spectroscopic survey explicitly at unused slits is now investigated.

EMIR contains 55 configurable slits, providing spectroscopy over a wavelength range of 0.9μm - 2.5μm (Garzón et al., 2007). The imaging FoV is $6\overset{\prime}{.}7$x$6\overset{\prime}{.}7$, while the spectroscopic FoV is $6\overset{\prime}{.}7$x4'.

The number of slits used by the primary science case is determined by the number of science objects, their distribution within the FoV, and the position of their required sky slits. EMIR has the ability to maximise this number through a rotation axis.

An `idl` program was written to simulate the EMIR setup. The EMIR Associated Scientific Team (EAST) have prepared science proposals describing areas of interest from the scientific community. By applying the observational parameters of each science case to the EMIR simulator, the potential of carrying out serendipitous observations in the background to each primary science program was investigated. The number of extra targets available per exposure for each individual science case has been calculated, making estimates on the gains of implementing a serendipitous survey.

There were 16 EAST science proposals, five were viable for serendipitous observations (i.e. using the multi-slit mode, with low-to-moderate source densities. Each proposal supplied an estimated observational time, giving 72hrs of planned MOS time which could lend themselves to serendipitous observations.

Each proposal provided the expected number of primary targets within the EMIR FoV and the galactic latitude of the observations. As an example of a potential serendipitous follow-up program, the number of extra targets available per FoV were obtained at the required galactic latitude from the Large Area Survey (LAS) third data release (Lada et al., 2007). The various EMIR spectroscopic readout modes mean that the magnitude of the primary target does not restrict the observable magnitude of the potential extra objects. As different detector strips can be readout independently, bright serendipitous objects need not saturate the detector when observing faint primary objects. Likewise, faint objects can collect light for longer than is required for bright primary objects.

Program Description

The end product of the program is to calculate for a given number of primary objects, how many extra objects can be observed in the EMIR multi-slit configurable mask. Primary objects refer to targets that come from the main science case, and extra objects are 'serendipitous' objects within the FoV which can be observed.

Random positions are generated for the required number of primary and extra objects within the EMIR FoV. The program calculates which orientation and slit configuration maximises the number of primary objects observable. Each primary object requires a sky slit which must be situated in the adjacent slit to allow an ABBA dither pattern. The sky slit can be either side of the object slit, although it must be the same for all objects in that observation. This is a slight restriction from real operations where there will be more sky modes and dither patterns available. For some observations it will be possible to use one sky slit for two objects, reducing the number of sky slits. In this context the simulation is slightly pessimistic about the number of serendipitous slits available. The number of extra targets which can be observed by the remaining slits is found. These targets also require a sky slit, and if none are available then the object is rejected. If there are two configurations that observe the same number of primary targets, then the configuration that includes the most extra targets is accepted as the optimum configuration.

Point sources only occupy one pixel within the simulation. The real point source targets will have a FWHMs of around 3-4 pixels. This means that the distribution of some stars will result in them being spread across more than one slit. Each slit will occupy $\sim$37 pixels and so the FWHM of a point source occupies $\sim 10\%$ the slit. Therefore the results will be slightly optimistic in terms of the number of slits available for serendipitous observations.

The galactic latitudes for each EAST case were used to determine the density of objects within that region which in turn was converted into the number of objects that would be detected within the EMIR FoV. For each proposal, the number of primary targets along with the density of objects within a FoV at the particular pointing were run through the simulator. Due to the random distribution of objects within the simulator, each observation was tested 10 times and the mean number of serendipitous objects available was calculated, resulting in a total value for each EAST proposal.

Science Proposals

The EAST proposals were used to extract the relevant data for the EMIR serendipity simulations, such as exposure times, number of primary targets expected within the EMIR FoV, and RA and Dec (or galactic latitude) of the observations. The five cases are listed below, with the results summarised in Table A.1

- Searching for Brown Dwarf-Like Secondary Stars in Cataclysmic Variables
- IR Spectroscopy of Highly Obscured X-Ray Binaries
- Near-IR Spectroscopy of Isolated Planetary-Mass Objects and Low-Mass Brown Dwarfs in σ Orionis
- Constraining the Evolution of Early-Type Galaxies in Clusters with the Ca II Triplet
- N-IR Spectroscopy of Brown Dwarf Candidates in Distant Young Open Clusters

114±9 objects

Results

Combining the results from the five relevant proposals, a total of ~700 extra objects can potentially be observed (see Table A.1). Of course, due to the different types of science case analysed, 72hrs of MOS observing time does not always equate to ~700 extra objects being obtainable. Some science cases stay on one pointing for several hours, whereas another pointing will have an exposure time of a few minutes. However, if the number of primary objects per FoV is known, along with the number of pointings and the galactic latitude, the number of extra objects observable per science case can be found.

Table A.1: Total Number of extra objects observable over the 5 investigated science cases.

Science Case	Number of Pointings	Observing Time (hours)	Extra Objects
1	4	3	63±3
2	9	4	223±9
3	10	24	132±14
4	11	22	164±12
5	8	16	114±9
Total	41	72	696±47

Some proposals are more open to serendipitous measurements than others, with results being specific to each science case put forward. In order to examine the number of serendipitous objects observable for future proposals, the number of extra targets that are potentially observable was calculated for a given number of primary targets in various field densities. For example, if there are 15 primary objects within a FoV, by distributing 100-400 extra targets within the FoV, how many serendipitous targets could be observed? The 100-400 extra object range mimics the lowest to highest density regions (from $|\mathrm{b}| = 80-20^{\circ}$) in the LAS K_{s}-band images. As a by-product, the test would also investigate for a certain number of primary targets within a FoV, how many could spectra be obtained through various slit orientations.

Due to the random distribution of targets, the `idl` program was run six times for each set of parameters, with the mean outputs recorded, as shown in Figure A.2. The plot titles indicate how many primary objects were in the FoV. The key inside the graphs refer to how many primary and extra objects could be observed. The total key refers to the number of slits occupied, which includes primary and extra objects, along with their sky slits.

Of course, the number of extra targets is dependent on the number of primary sources within the FoV but, 5-20 extra targets can be observed per field.

Conclusion

The difficulties that arise from carrying out serendipitous observations are largely related to issues such as data storing, configuration planning, and data reduction and are all solvable. Thus, unoccupied EMIR slits can be used to observe additional objects for no extra exposure time. Of the five science cases examined an extra $\sim$700 objects could be observed over an 87hr period. This shows that EMIR could carry out a general survey (such as UKIDSS-LAS follow-up) while other astronomers complete specific proposals. Increasing apertures to ELT size will only increase the attractiveness of such surveys, as large focal planes will provide more space for serendipitous sources.

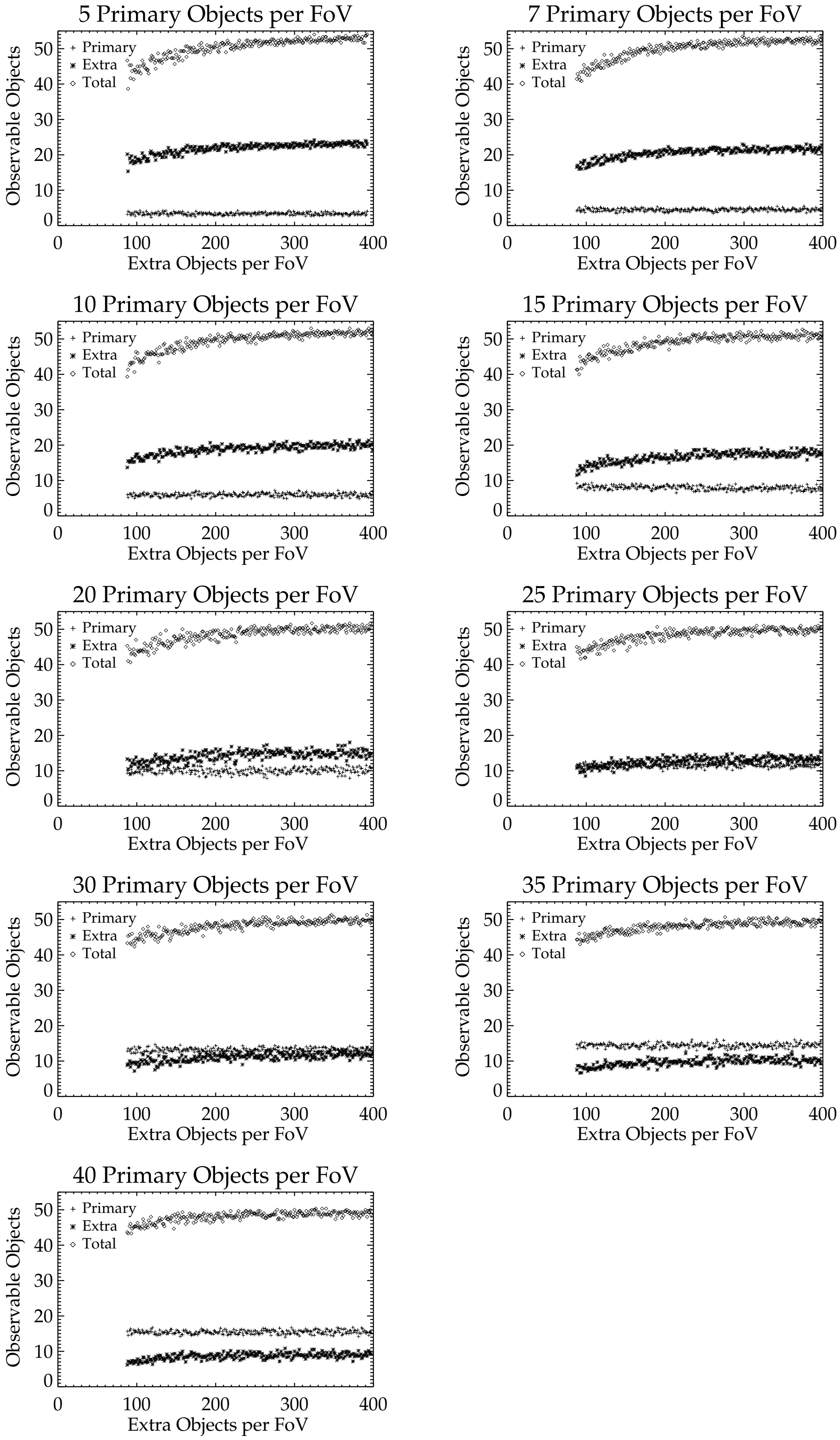

Figure A.2: Results from serendipitous measurements for varying number of primary objects per FoV.

References

Alves J. F., Lada C. J., Lada E. A., 2001, Nature, 409, 159

Andersen M., Zinnecker H., Moneti A., McCaughrean M. J. et al., 2009, ApJ, 707, 1347

Ascenso J., Alves J., Lago M. T. V. T., 2009, Ap&SS, 324, 113

Ballesteros-Paredes J., Klessen R. S., Vázquez-Semadeni E., 2003, ApJ, 592, 188

Bastian N., Gieles M., 2008, in Astronomical Society of the Pacific Conference Series, Vol. 388, Mass Loss from Stars and the Evolution of Stellar Clusters, A. de Koter, L. J. Smith, & L. B. F. M. Waters, ed., pp. 353–+

Bastian N., Goodwin S. P., 2006, MNRAS, 369, L9

Bate M. R., 2010, MNRAS, 404, L79

Bate M. R., Bonnell I. A., Bromm V., 2003, MNRAS, 339, 577

Baumgardt H., 2006, ArXiv Astrophysics e-prints

Baumgardt H., Makino J., 2003, MNRAS, 340, 227

Bonnor W. B., 1956, MNRAS, 116, 351

Bosch G., Selman F., Melnick J., Terlevich R., 2001, A&A, 380, 137

Bosch G., Terlevich E., Terlevich R., 2009, AJ, 137, 3437

Bosch G., Terlevich R., Melnick J., Selman F., 1999, A&AS, 137, 21

Bouy H. et al., 2008, A&A,, 477, 681

Brandl B., Sams B. J., Bertoldi F., Eckart A. et al., 1996, ApJ, 466, 254

Brandner W., Grebel E. K., Barbá R. H., Walborn N. R. et al., 2001, AJ, 122, 858

Breare M., Mahony N. O., 1996, IEEE Spectrum, 10, 6

Breysacher J., 1981, A&AS, 43, 203

Campbell B., Hunter D. A., Holtzman J. A., Lauer T. R., Shaya E. J., Code A., Faber S. M., Groth E. J., 1992, AJ, 104, 1721

Campbell M. A., Evans C. J., Mackey A. D., Gieles M. et al., 2010, MNRAS, 405, 421

Casali M., Ageorge N., Alves de Oliveira C., Biereichel P. et al., 2009, in Science with the VLT in the ELT Era, A. Moorwood, ed., pp. 315–+

Chen C., Chu Y., Gruendl R. A., Gordon K. D. et al., 2009, ApJ, 695, 511

Crowther P. A., Schnurr O., Hirschi R., Yusof N. et al., 2010, MNRAS, 1103

Crowther P. A., Smith L. J., 1997, A&A, 320, 500

Cuby J., Morris S., Parr-Burman P., Lehnert M. et al., 2009, in Society of Photo-Optical Instrumentation Engineers (SPIE) Conference Series, Vol. 7439, Society of Photo-Optical Instrumentation Engineers (SPIE) Conference Series

Davies B., Lumsden S. L., Hoare M. G., Oudmaijer R. D. et al., 2010, MNRAS, 402, 1504

Davies R., Genzel R., 2010, The Messenger, 140, 32

de Marchi G., Nota A., Leitherer C., Ragazzoni R. et al., 1993, ApJ, 419, 658

Ebert R., 1955, ZAp, 37, 217

Elmegreen B. G., 1983, MNRAS, 203, 1011

—, 2007, ApJ, 668, 1064

Els S. G., Travouillon T., Schöck M., Riddle R. et al., 2009, PASP, 121, 527

Elson R. A. W., Fall S. M., Freeman K. C., 1987, ApJ, 323, 54

Evans C. J., Bastian N., Beletsky Y., Brott I. et al., 2010, in IAU Symposium, Vol. 266, IAU Symposium, R. de Grijs & J. R. D. Lépine, ed., pp. 35–40

Fazio G. G., Hora J. L., Allen L. E., Ashby M. L. N. et al., 2004, ApJS, 154, 10

Foppiani I., Diolaiti E., Lombini M., Baruffolo A. et al., 2010, in Adaptative Optics for Extremely Large Telescopes

Freedman W. L., Madore B. F., Gibson B. K., Ferrarese L. et al., 2001, ApJ, 553, 47

Fried D. L., 1966, Journal of the Optical Society of America (1917-1983), 56, 1380

—, 1990, Journal of the Optical Society of America A, 7, 1224

Fusco T., Meimon S., Clenet Y., Cohen M., Schnetler H., Paufique J., Michau V., Amans J., Gratadour D., Petit C., Robert C., Jagourel P., Gendron E., Rousset G., Conan J., Hubin N., 2010, in Society of Photo-Optical Instrumentation Engineers (SPIE) Conference Series, Vol. 7736, Society of Photo-Optical Instrumentation Engineers (SPIE) Conference Series

Garcia-Lorenzo B. M., Fuensalida J. J., Eff-Darwich A. M., 2004, in Society of Photo-Optical Instrumentation Engineers (SPIE) Conference Series, Vol. 5572, Society of Photo-Optical Instrumentation Engineers (SPIE) Conference Series, J. D. Gonglewski & K. Stein, ed., pp. 384–391

Garzón F., Abreu D., Barrera S., Becerril S. et al., 2007, in Revista Mexicana de Astronomia y Astrofisica, vol. 27, Vol. 29, Revista Mexicana de Astronomia y Astrofisica Conference Series, pp. 12–17

Grebel E. K., Chu Y., 2000, AJ, 119, 787

Greenwood D. P., 1977, Journal of the Optical Society of America (1917-1983), 67, 390

Gruendl R. A., Chu Y., 2009, ApJS, 184, 172

Hardy J. W., 1998, Adaptive Optics for Astronomical Telescopes

Hills J. G., 1980, ApJ, 235, 986

Høg E., Fabricius C., Makarov V. V., Urban S. et al., 2000, A&A, 355, L27

Hunter D. A., Shaya E. J., Holtzman J. A., Light R. M. et al., 1995, ApJ, 448, 179

Hunter D. A., Vacca W. D., Massey P., Lynds R. et al., 1997, ApJ, 113, 1691

Hyland A. R., Straw S., Jones T. J., Gatley I., 1992, MNRAS, 257

Indebetouw R., Mathis J. S., Babler B. L., Meade M. R. et al., 2005, ApJ, 619, 931

Johansson L. E. B., Greve A., Booth R. S., Boulanger F. et al., 1998, A&A, 331, 857

Kellerer A., 2008, CANARY: final design review

Kim H., Kim S., Bak J., Garcia M. et al., 2007, ApJ, 669, 1003

King I., 1962, AJ, 67, 471

Kissler-Patig M. et al., 2008, A&A, 491, 941

Kolmogorov A., 1941, Akademiia Nauk SSSR Doklady, 30, 301

Kornilov V. G., Tokovinin A. A., 2001, Astronomy Reports, 45, 395

Kraus S., Hofmann K., Menten K. M., Schertl D. et al., 2010, Nature, 466, 339

Lada C. J., 1987, in IAU Symposium, Vol. 115, Star Forming Regions, M. Peimbert & J. Jugaku, ed., pp. 1–17

Lada C. J., Alves J. F., Lombardi M., 2007, Protostars and Planets V, 3

Lada C. J., Lada E. A., 2003, ARA&A, 41, 57

Lada C. J., Margulis M., Dearborn D., 1984, ApJ, 285, 141

Larsen S. S., 2004, A&A, 416, 537

Lejeune T., Schaerer D., 2001, VizieR Online Data Catalog, 6102, 0

Mac Low M., Klessen R. S., 2004, Reviews of Modern Physics, 76, 125

Mackey A. D., Gilmore G. F., 2003, MNRAS, 338, 85

Maercker M., Burton M. G., 2005, VizieR Online Data Catalog, 343, 80663

Marchetti E., Brast R., Delabre B., Donaldson R. et al., 2007, The Messenger, 129, 8

Mason B. D., Hartkopf W. I., Gies D. R., Henry T. J. et al., 2009, AJ, 137, 3358

Massey P., Hunter D. A., 1998, ApJ, 493, 180

McGlynn T. A., 1984, ApJ, 281, 13

McLaughlin D. E., van der Marel R. P., 2005, ApJS, 161, 304

Meixner M., Gordon K. D., Indebetouw R., Hora J. L. et al., 2006, AJ, 132, 2268

Meylan G., 1993, in The globular clusters-galaxy connection, Smith G. H., Brodie J. P., eds., Astronomical Society of the Pacific (ASP) Conference Series, Vol. 48, p. 588

Morris T., Hubert Z., Myers R., Gendron E. et al., 2010, in Adaptative Optics for Extremely Large Telescopes

Noll R. J., 1976, Journal of the Optical Society of America (1917-1983), 66, 207

Noyola E., Gebhardt K., 2007, AJ, 134, 912

Parker J. W., 1993, AJ, 106, 560

Pasquini L., Avila G., Blecha A., Cacciari C. et al., 2002, The Messenger, 110, 1

Perina S., Barmby P., Beasley M. A., Bellazzini M. et al., 2009, A&A, 494, 933

Portegies Zwart S., McMillan S., Gieles M., 2010, ArXiv e-prints

Price D. J., Bate M. R., 2009, MNRAS, 398, 33

Probst R. G., Montane A., Warner M., Boccas M. et al., 2003, in Society of Photo-Optical Instrumentation Engineers (SPIE) Conference Series, Vol. 4841, Society of Photo-Optical Instrumentation Engineers (SPIE) Conference Series, M. Iye & A. F. M. Moorwood, ed., pp. 411–419

Rieke G. H., Lebofsky M. J., 1985, ApJ, 288, 618

Rigaut F., 2002, in European Southern Observatory Conference and Workshop Proceedings, Vol. 58, European Southern Observatory Conference and Workshop Proceedings, E. Vernet, R. Ragazzoni, S. Esposito, & N. Hubin, ed., pp. 11–+

Robitaille T. P., Whitney B. A., Indebetouw R., Wood K. et al., 2006, ApJS, 167, 256

Rousset G., Beuzit J., Hubin N., Gendron E. et al., 1994, in Presented at the Society of Photo-Optical Instrumentation Engineers (SPIE) Conference, Vol. 2201, Society of Photo-Optical Instrumentation Engineers (SPIE) Conference Series, M. A. Ealey & F. Merkle, ed., pp. 1088–1098

Rubio M., Barbá R. H., Walborn N. R., Probst R. G. et al., 1998, AJ, 116, 1708

Rubio M., Roth M., Garcia J., 1992, A&A, 261, L29

Rutten R. G., Clark P., Myers R. M., Wilson R. W. et al., 2003, in Society of Photo-Optical Instrumentation Engineers (SPIE) Conference Series, Vol. 4839, Society of Photo-Optical Instrumentation Engineers (SPIE) Conference Series, P. L. Wizinowich & D. Bonaccini, ed., pp. 360–369

Salpeter E. E., 1955, ApJ, 121, 161

Sarazin M., Roddier F., 1990, A&A, 227, 294

Schaerer D., Meynet G., Maeder A., Schaller G., 1993, A&AS, 98, 523

Schnurr O., Chené A., Casoli J., Moffat A. F. J. et al., 2009, MNRAS, 397, 2049

Seale J. P., Looney L. W., Chu Y., Gruendl R. A. et al., 2009, ApJ, 699, 150

Selman F., Melnick J., Bosch G., Terlevich R., 1998, VizieR Online Data Catalog, 334, 10098

Sirianni M., Nota A., Leitherer C., De Marchi G. et al., 2000, ApJ, 533, 203

Skrutskie M. F., Cutri R. M., Stiening R., Weinberg M. D. et al., 2006, AJ, 131, 1163

Takahashi K., Portegies Zwart S. F., 2000, ApJ, 535, 759

Tatarskii V. I., 1971, The effects of the turbulent atmosphere on wave propagation, Tatarskii, V. I., ed.

Terletsky P. Y., 1952, Zh. Eksper. Teor. Fiz, 22, 506

Tokovinin A., Kornilov V., 2002, in Astronomical Society of the Pacific Conference Series, Vol. 266, Astronomical Site Evaluation in the Visible and Radio Range, J. Vernin, Z. Benkhaldoun, & C. Muñoz-Tuñón , ed., pp. 104–+

Townsley L. K., Broos P. S., Feigelson E. D., Garmire G. P. et al., 2006, AJ, 131, 2164

Trundle C., Dufton P. L., Hunter I., Evans C. J. et al., 2007, A&A, 471, 625

Tyler G. A., 1994, Journal of the Optical Society of America A, 11, 325

Tyson R. K., 1998, Principles of adaptive optics, Tyson, R. K., ed.

Vaidya K., Chu Y., Gruendl R. A., Chen C. et al., 2009, ApJ, 707, 1417

Walborn N. R., 1986, in IAU Symposium, Vol. 116, Luminous Stars and Associations in Galaxies, C. W. H. De Loore, A. J. Willis, & P. Laskarides, ed., pp. 185–196

—, 1991, in IAU Symposium, Vol. 148, The Magellanic Clouds, R. Haynes & D. Milne, ed., pp. 145–+

Walborn N. R., Barbá R. H., Brandner W., Rubio M. et al., 1999, AJ, 117, 225

Walborn N. R., Blades J. C., 1997, ApJS, 112, 457

Walborn N. R., Maíz-Apellániz J., Barbá R. H., 2002, AJ, 124, 1601

Werner M. W., Roellig T. L., Low F. J., Rieke G. H. et al., 2004, ApJS, 154, 1

Whitney B. A., Sewilo M., Indebetouw R., Robitaille T. P. et al., 2008, AJ, 136, 18

Wyant J. C., Creath K., 1992, in Applied Optics and Optical Engineering, Volume XI, R. R. Shannon & J. C. Wyant, ed., Vol. 11, pp. 1–53

Zinnecker H., Yorke H. W., 2007, ARA&A, 45, 481